

EXAMINING SEDIMENT
ACCUMULATION RATES AND
DELTAIC PROCESSES IN A LARGE
RESERVOIR

Julie Bahr

A thesis
submitted to the faculty of
the Department of Earth and Environmental Sciences
in partial fulfillment
of the requirements for the degree of
Master of Science

Boston College
Morrissey College of Arts and Sciences
Graduate School

December 2024

EXAMINING SEDIMENT ACCUMULATION RATES AND DELTAIC PROCESSES IN A LARGE RESERVOIR

Julie Bahr

Advisor: Noah P. Snyder, Ph.D.

Reservoir sedimentation is a significant issue not only because it limits a reservoir's water storage capacity and threatens its ability to meet environmental and societal needs, but also because it reduces the amount of sediment reaching downstream coastal ecosystems where sediment loading sustains critical habitat for wildlife and fisheries. Reservoir deltas in particular can decrease channel capacity and lead to an increased flood risk for populations living in the alluvial plain upstream of dams; however, studies of these landforms are underrepresented in the literature. To address that knowledge gap, this project examines reservoir sedimentation in Lake Seminole, a 123 km² surface-water impoundment created in 1954 and located at the junction of the Chattahoochee and Flint Rivers in Florida and Georgia. Where it enters Lake Seminole, the Chattahoochee River has a large subaerial delta that is actively prograding. High-resolution topographic and bathymetric datasets and historical cross section data were analyzed to measure the evolution of this delta and characterize subaerial and subaqueous sedimentation in the reservoir more broadly. In addition, a comparative land-cover change analysis was conducted for the three watersheds that drain to Lake Seminole to explore potential links between the suspended sediment generated by these surface disturbances and sedimentation patterns in each arm of the reservoir. Across the entire reservoir body, subaqueous sediment accumulated at a rate of 0.81 cm/yr between 1957–1976 and 0.12 cm/yr between 1976–2009, with the highest sedimentation rates occurring shortly after dam construction. Within the Chattahoochee arm, subaqueous sediment accumulated at a rate of 2.79 cm/yr between 1957–1976 and 0.68 cm/yr between 1976–2009, whereas, in the Flint arm, subaqueous sediment eroded at a rate of -0.21 cm/yr between 1957–1976 and accumulated at a rate of 0.08 cm/yr between 1976–2009. Qualitative observations indicate that the erosional signal in the Flint is focused in the upstream-most portion of the arm

and a depositional signal emerges farther downstream. On the Chattahoochee River delta, subaerial sediment accumulated at a rate of 1.46 ± 0.48 cm/yr between 2007–2018, with the most rapid areas of aggradation (> 4.5 cm/yr) located around the exterior edges of the delta islands. No strong link was found between the percentage of each watershed that underwent land cover change and the sedimentation rates in each reservoir arm. This analysis will provide new insights into the physical processes of reservoir sedimentation that can be used to inform river management practices and decrease the negative impacts of sediment trapping not only within reservoirs, but also upstream and downstream of dams.

Table of Contents

List of Figures	vii
List of Tables	viii
Acknowledgements	ix
Chapter 1: Introduction and Background	1
1.1 In-Reservoir Sedimentation Dynamics.....	2
1.1.1 Delta Depositional Patterns	4
1.1.2 Reservoir Deltas and Sediment Accumulation	7
1.2 Upstream Impacts of Reservoirs	10
Chapter 2: Lake Seminole and the ACF River Basin	13
2.1 Lake Seminole	13
2.2 Apalachicola-Chattahoochee-Flint (ACF) Basin.....	19
2.3 Research Questions and Objectives.....	21
Chapter 3: Tracking Subaerial Delta Sedimentation Using Lidar Topographic Differencing	23
3.1 Introduction and Background	23
3.1.1 DEM Differencing	23
3.1.2 Multiscale Model-to-Model Cloud Comparison	25
3.1.3 Lidar Ground Filtering	27
3.2 Methods	29
3.2.1 Datasets	29
3.2.2 DEM Differencing	33
3.2.3 Point Cloud Differencing.....	34
3.3 Results	46
3.3.1 DEM Differencing	46
3.3.2 Point Cloud Differencing.....	47
3.3.3 Methodological Comparison	50
3.4 Discussion and Conclusions	51
Chapter 4: Evaluating Subaqueous Sedimentation Using Bathymetric Surveys and Cross Sections	55
4.1 Introduction	55
4.2 Methods	56
4.2.1 Bathymetric Surveys	56
4.2.2 Historical Cross Sections.....	61
4.3 Results	66
4.3.1 Bathymetric Survey Rasters and Cross-Sectional Sedimentation Rates	66

4.3.2 Historical Cross Section Sedimentation Rates	69
4.4 Discussion and Conclusions	71
Chapter 5: Comparing Three Decades of Land-Cover Change in the Chattahoochee, Flint, and Spring Creek Watersheds.....	76
5.1 Introduction	76
5.2 Methods	77
5.2.1 Training Data Selection	77
5.2.2 Multi-date Image Classification	78
5.2.3 Post-Classification Correction.....	79
5.2.4 Accuracy Assessment	79
5.3 Results	80
5.4 Discussion and Conclusions	86
Chapter 6: Summary and Conclusions	89
References	91
Appendix A: All Bathymetric Survey Cross Section Plots.....	97
Appendix B: Combined USACE and Bathymetric Survey Cross Section Plots	109

List of Figures

Figure 1. Active progradation of a reservoir delta in the Chattahoochee River	2
Figure 2. Schematic diagram of homopycnal and hyperpycnal inflow	5
Figure 3. The two main dimensions of delta deposition: aggradation and progradation	7
Figure 4. Diagram of the four morphologic zones of reservoir deltas	11
Figure 5. Aerial image of Lake Seminole and the Jim Woodruff Dam (2023)	14
Figure 6. Illustration of the Jim Woodruff Lock and Dam	15
Figure 7. Geologic map of the Lake Seminole watershed.....	17
Figure 8. Location of Lake Seminole and the boundaries of the ACF river basin	20
Figure 9. DEM differencing methodology	25
Figure 10. Visualization of the two key steps in the M3C2 algorithm	27
Figure 11. Footprints of the Lake Seminole topographic datasets listed in Table 1	31
Figure 12. DEMs of the Chattahoochee River delta in 2007 and 2018	32
Figure 13. Sample islands from the downstream portion of the 2018 lidar ground point cloud	37
Figure 14. Downstream portion of the 2007 lidar ground point cloud	39
Figure 15. DEM created using the unedited M3C2 output point clouds from CloudCompare	40
Figure 16. Process of evaluating erosional signal at the center of the delta islands	42
Figure 17. Plots of the 2007-2018 lidar survey elevation changes and deposition	43
Figure 18. Histogram of the 2007-2018 depositional point cloud	46
Figure 19. DoD showing the Chattahoochee River delta elevation change between 2007–2018 ..	47
Figure 20. The final digital elevation models of delta deposition from 2007-2018	48
Figure 21. Plot of deposition against downstream distance along the Chattahoochee River delta	50
Figure 22. Map showing locations of USACE Lake Seminole sedimentation rangelines	62
Figure 23. Cross section plot of range 07A	63
Figure 24. Process of splitting Lake Seminole into 14 sections in ArcGIS Pro	64
Figure 25. Map of the 2009 bathymetric survey of Lake Seminole	68
Figure 26. 2009–2023 sedimentation rates for select USACE rangelines.....	68
Figure 27. Map of the reservoir sections used to calculate the sedimentation rates in Table 5	71
Figure 28. Land-cover change in the watersheds that drain to Lake Seminole from 1993–2023 .	82

List of Tables

Table 1. Summary of the metadata for the 2007 and 2018 lidar surveys.	31
Table 2. Comparison of the descriptive statistics and uncertainty values for the depositional DEMs (Figure 20) produced using DEM differencing and the M3C2 algorithm.	51
Table 3. Summary of the metadata for the 2009 and 2023 bathymetric surveys.	57
Table 4. Historical sedimentation rates at the USACE rangelines that sample Lake Seminole. ...	70
Table 5. Spatially integrated sedimentation rates calculated for the entirety of Lake Seminole and the Chattahoochee and Flint arms.	70
Table 6. Confusion matrix comparing reference data assessments with map categories for the Chattahoochee River watershed.	83
Table 7. Confusion matrix comparing reference data assessments with map categories for the Flint River watershed.	83
Table 8. Confusion matrix comparing reference data assessments with map categories for the Spring Creek watershed.	83
Table 9. Probability matrix for the Chattahoochee River watershed.	84
Table 10. Probability matrix for the Flint River watershed.	84
Table 11. Probability matrix for the Spring Creek watershed.	84
Table 12. Area estimates, adjusted area estimates of the final map classes, and 95% confidence intervals for the adjusted area estimates for the Chattahoochee River watershed.	85
Table 13. Area estimates, adjusted area estimates of the final map classes, and 95% confidence intervals for the adjusted area estimates for the Flint River watershed.	85
Table 14. Area estimates, adjusted area estimates of the final map classes, and 95% confidence intervals for the adjusted area estimates for the Spring Creek watershed.	85

Acknowledgements

I would like to begin by thanking my advisor, Noah Snyder, not only for his outstanding mentorship and support of my research ambitions, but also for accepting me as a student in the first place and believing I had what it took to succeed in grad school even when I didn't believe in myself. Thank you also to Kat Wilson for providing incredibly thoughtful feedback during the process of revising this document and throughout the duration of my master's degree. To Mark Behn: thank you for serving on my committee and supporting a lot of numerical modeling work that didn't make it into this thesis.

Thank you to the U.S. Army Engineer Research and Development Center (ERDC) for funding this project and providing several data sources used herein. In particular, I would like to thank Travis Dahl for his guidance and helpful feedback.

To the Surface Process lab group at BC: thank you for listening to me talk about the nitty-gritty details of lidar data multiple times and for providing invaluable advice and insightful comments throughout the course of my graduate career. Special thanks to Anna Regnier and Tony Edgington: Anna—it was an honor to be able to mentor you and Tony—it was amazing to have someone else who cared as much about the muck in this swampy reservoir as I did.

To my parents: thank you for moving me out to Boston (and then back home again two years later) and for picking up the phone every time something went wrong in my hundred-year-old apartment. I couldn't have made it through grad school without your love and support. To my sister, Sarah, whom I promised a shout-out in the acknowledgements of my thesis in exchange for editing the personal statement I submitted with my BC application three years ago: thank you for teaching me pretty much everything I know about writing. I have no doubt this thesis would be highly unintelligible without your never-ending guidance and patience for my over-use of a thesaurus growing up. To my friends and fellow graduate students in EESC: thank you for all of the laughs and donuts and ice cream and welcome distractions and amazing memories that I'll no doubt cherish for the rest of my life.

Chapter 1: Introduction and Background

When a river's fast-flowing water meets the slower-moving or still water of a lake, sea, or ocean, it deposits sediment, creating a natural landform known as a delta. Deltas can also form in anthropogenic ecosystems when a river flows into the upstream end of a reservoir and the abrupt decrease in energy prompts the river to drop its sediment load (Csiki and Rhoads, 2010; Stratton and Grant, 2019). Additionally, reservoir deltas can develop where tributaries enter reservoirs laterally (Volke et al., 2019). Because dam construction strongly reduces the sediment carrying capacity of a river while the incoming sediment load from the drainage basin remains the same, the channel must undergo self-adjustments upstream of the reservoir to accommodate the incoming sediment. A river does this by either (1) increasing its gradient through a reduction in channel length achieved through more frequent meander cutoffs, or (2) reforming its longitudinal profile via progressive sediment deposition, which often takes the form of a reservoir delta (Xu, 1990).

Reservoir deltas can contribute to an increased flood risk due to decreased channel capacity and, thus, flood conveyance; however, they can also serve as crucial wetland habitats (Bricker et al., 2008; Juracek, 2015). Additionally, reservoir deltas can impede on-reservoir recreation and serve as an ideal site for invasive plant species to colonize (Volke et al., 2015). Therefore, understanding how reservoir deltas form and evolve with time, and then connecting these changes in reservoir sedimentation with the land-use characteristics of a watershed, can help to inform future delta and river management practices and minimize human and ecological harm. In order to evaluate the impacts of reservoir deltas, this project examines the rates and processes of sedimentation in Lake Seminole, a U.S. Army Corps of Engineers (USACE) reservoir located at the junction of the Chattahoochee and Flint Rivers in Florida and Georgia. Lake Seminole is an ideal study site because the mouth of the Chattahoochee River has a large subaerial delta that is

presently exhibiting active progradation whereas the Flint arm of the reservoir does not have any subaerial delta deposits (Figure 1).

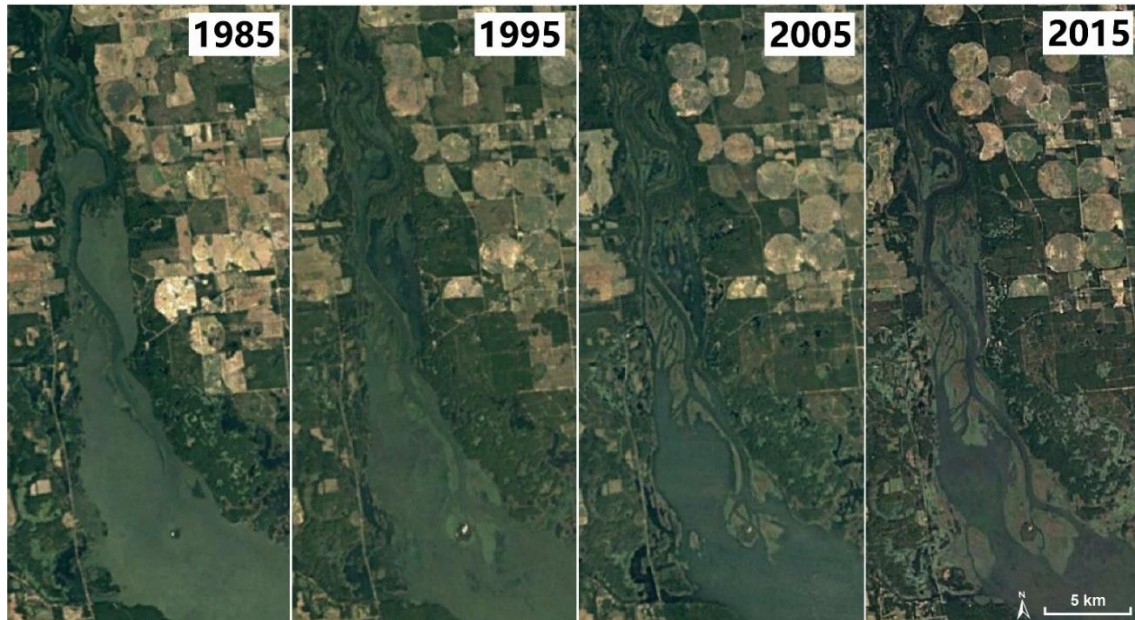


Figure 1. Active progradation of a reservoir delta in the Chattahoochee River at the upstream end of Lake Seminole. (Data source: NASA/USGS Landsat)

1.1 In-Reservoir Sedimentation Dynamics

Studies of reservoir sedimentation are crucial in understanding watershed management issues stemming from reservoir operation, sediment budgets, and depositional processes. At a foundational level, dams disturb the sediment balance within a riverine ecosystem by trapping sediment and reducing sediment loads downstream of the impoundment, engendering channel incision and bed sediment changes (Mossa and Chen, 2022). Storage of water in reservoirs in the United States peaked at 45,000 m³ per capita in 1975 but has since declined to 27,000 m³ per capita as of 2019, largely due to population growth and sediment infilling behind dams (Morris, 2020). A 2016 survey of USACE reservoir projects indicated that 26% of reservoirs in the U.S. have experienced some level of sedimentation impacts (Morris et al., 2023). In addition, dams are one of the most significant ways humans impact global sediment exchange between land and

oceans, with as much as 25% of annual global sediment discharge impounded (Stratton and Grant, 2019).

Despite these negative impacts, dams are a life-sustaining and essential component of global water infrastructure, with functions ranging from controlling floods to supplying water for municipal, agricultural, and industrial uses and supporting recreation activities like fishing and boating. The rate at which a reservoir fills with sediment is an important consideration for its long-term utility because a dam's water storage capacity can be significantly reduced as a delta progrades into a reservoir (Morris et al., 2023). This is especially true during extreme flood events: in 2013, more than half of the sediment eroded from a watershed during extreme flooding in the Colorado Front Range was deposited in a reservoir delta, reducing water storage capacity by 2% (Rathburn et al., 2017). The researchers estimated that a minimum of 420 mm of reservoir sedimentation occurred during the flood, which was nearly eighty times greater than the 5.4 mm/year background sedimentation rate for the reservoir (Rathburn et al., 2017).

In spite of their utility, studies of reservoir sedimentation are underrepresented in the literature and sedimentary deltas in particular form a significant gap in our current knowledge of dammed river basins (Stratton and Grant, 2019; Volke et al., 2015). Because of this, the science surrounding the processes that control sedimentation in individual reservoirs is limited, which is part of what this project aims to address. Given that both dam construction and rapid land-use changes have significantly altered sediment transport systems in the world's rivers, and that more dam projects and altered land-use practices can be expected in the future, it is crucial to strengthen our current understanding of dynamics of sediment deposition in reservoirs (Dethier et al., 2022). Moreover, most USACE reservoirs have surpassed their original 50-year planning lives, so addressing the challenges of long-term sediment storage and management is a key concern considering both the age of these projects and the threat of increased sediment inflows under climate change (Morris et al., 2023).

1.1.1 Delta Depositional Patterns

Before delving into more recent literature on in-reservoir sedimentation, it is important to provide a brief overview of the pioneering work on deltaic sedimentation that laid the foundation for our current understanding of delta formation and depositional patterns. Sedimentary processes and delta depositional patterns were first described in the scientific literature by Gilbert (1885) and their stratigraphy is defined by distinctive topset, foreset, and bottomset beds where the topset beds are dominated by coarse gravel and sand and the bottomset beds are comprised of silt, clay, and fine sand (Gilbert, 1885). Though Gilbert's three-part delta has become synonymous with a "typical" delta, the term "Gilbert-type delta" was first introduced by Bates (1953), who characterized it as a product of homopycnal flow into lakes (Jones, 1965). Thus, it is useful to consider both Gilbert's (1885) and Bates' (1953) conceptual understandings of deltas.

Gilbert (1885) began by defining the key principle of delta formation: the capacity and competence of a stream are functions of its velocity, so a swift current can transport both more sediment and coarser sediment than a slow current. It follows that if there is a change in a stream's velocity, then there must be either deposition or erosion in the channel until a new equilibrium is reached. At the point where a river flows into a lake or reservoir, the large body of still water dissipates its velocity, so the stream's capacity and competence are consequently decreased, prompting the river to drop the coarser particles in its sediment load. These larger grains are propelled by their own weight as they slide down the face of a newly-forming delta, so the slope of the delta foreset will be equal to the angle of repose of the coarse material, which is typically between 20–35°. The finer part of the river's load is carried out beyond the foreset and, as the river's velocity continues to decrease, these particles gradually sink to the bottom, with coarser material settling out near the toe of the foreset and finer material being more widely diffused, eventually merging with the slope of the river bottom beyond the delta. This means a vertical section from any Gilbert delta will have, from top to bottom, three zones of deposition: a

flat-lying zone of sand-gravel sized sediments, a steeply inclined zone of sand-gravel sized sediments, and a gently inclined zone of silt-clay sized sediments (Figure 2). As these deltaic sediment deposits build up, they effectively act as a barrier that further reduces the river's velocity immediately upstream, which causes another deposit, and this cycle of decreased velocity followed by sediment deposition propagates upstream until the profile of the stream achieves a continuous grade from the toe of the delta backward to some steeper part of its channel upstream.

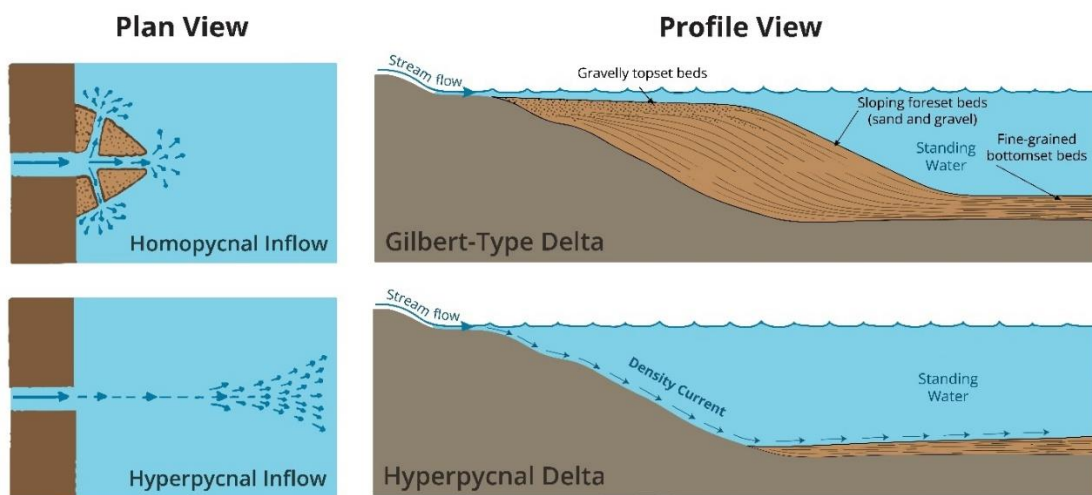


Figure 2. Schematic diagram of homopycnal and hyperpycnal inflow into a basin and the subsequent deltaic deposits. Adapted from Bates (1953).

While Gilbert (1885) focused on descriptions of the distinct layering and gradation in deltas, Bates (1953) centralized density contrasts in order to characterize three different types of inflow into permanent bodies of water: hyperpycnal, homopycnal, and hypopycnal. For hyperpycnal conditions, the inflow is more dense, so the sediment-laden river water plunges and flows along the bottom of the water body as a turbidity (density) current (Figure 2). In homopycnal conditions, the inflow is comparably dense to the water body, so mixing readily takes place in three dimensions, creating a Gilbert-type delta with topset, foreset, and bottomset beds. Lastly, hypopycnal conditions occur when the inflow is less dense, so the river water flows out over the surface of the denser fluid in the water body. Nearly all major rivers emptying

directly into a marine environment have hypopycnal discharges because of the interactions between the freshwater and saline basin water.

Hyperpycnal inflow into lakes or reservoirs can be driven by both differences in temperature and suspended sediment. For example, even if a river's suspended sediment concentration is comparable to a lake's, colder river temperatures can cause the plume to plunge to the base of the lake and produce turbidity currents. Additionally, hyperpycnal inflow can retain considerable speeds farther downstream, transporting finer-grained sediment many kilometers away the river's mouth. For example, between 1935–1948, 13 m of sediment were deposited where the Colorado River enters Lake Mead, but 34 m of sediment were deposited 48 km downstream against the face of the Hoover Dam due to contributions from hyperpycnal flows (Bates, 1953). In reservoirs, the transport and deposition of sediment is often influenced by turbidity currents that follow the thalweg of the former river channel within the reservoir to the deepest portion, often near the dam. Homopycnal inflow occurs when a river flows into a well-mixed lake or reservoir that has a similar water temperature, and it is the most common type of inflow into freshwater bodies. Bates's (1953) theoretical depositional pattern for homopycnal inflow closely matches Gilbert's (1885) descriptions of deltaic deposits in nature: homopycnal inflow develops partly subaerial flat, topset beds flanking the stream channel that quickly transition to foreset beds resting at the angle of repose (Bates, 1953). Observational and process-based frameworks such as Gilbert (1885) and Bates (1953) provide the basis on which to form and test hypotheses of delta processes using modern experimental and observation methods.

Additionally, it is important to note that the rate of lateral motion associated with deltaic sedimentation occurs much faster than the rate of net sediment accumulation (Sadler and Jerolmack, 2014). That is to say, progradation—the movement of a delta outward into a body of water—is substantially faster than aggradation—the delta building up above the water level, at most timescales (Figure 3). Part of the reason for this is that, after delta islands are subaerial, aggradation is only possible during floods when the inundation of the islands facilitates the

deposition of sediment. This is relevant because, while progradation can be on the scale of meters or kilometers and is visible in 30 m Landsat pixels (Figure 1), aggradation is often on the scale of centimeters and can be much more challenging to track over time.

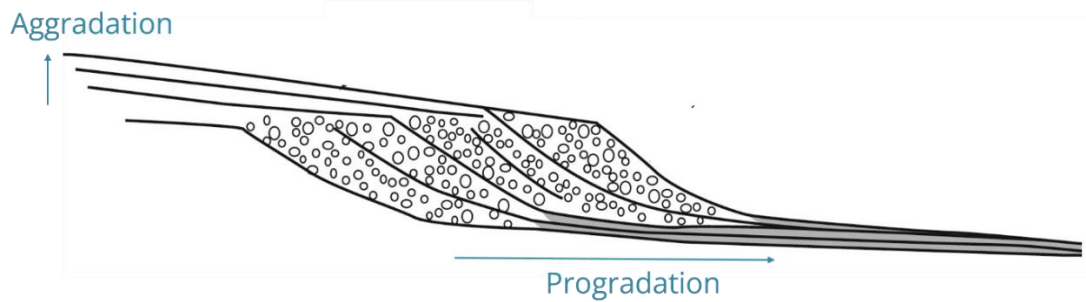


Figure 3. The two main dimensions of delta deposition: aggradation and progradation. Adapted from Rubi et al. (2018).

1.1.2 Reservoir Deltas and Sediment Accumulation

Previous studies of the dynamics of in-reservoir sedimentation have shown varied rates of sediment accumulation and disparate types of sediment deposition. Baena-Escudero et al. (2021) found that, in 56 years of dam operation, the Cantillana Dam in Spain lost 70% of its original storage capacity. Moreover, reservoir construction increased aggradation and decreased channel capacity upstream, leading to more frequent floodplain inundation (Baena-Escudero et al., 2021). In Englebright Lake, a sediment and flood-control reservoir on the Yuba River in California, Snyder et al. (2004) found that, over 60 years of dam operation, the accumulated sediment occupied 25% of the reservoir's original storage capacity and the accumulated material was deposited in a long, narrow delta with a prograding foreset wedge, following the Gilbert-style model.

Building upon this earlier analysis, Snyder et al. (2006) found that the Englebright Lake reservoir delta prograded during short-duration flood deposition and was reshaped during low-flow periods of prolonged reservoir drawdown that scoured sand from the topset beds and redeposited sediment within the active foreset. Additional research has also suggested that seasonal drawdowns in flood-control reservoirs exert a strong influence on sedimentation

patterns, especially with regard to increased low-elevation floodplain sediment deposition downstream of dams in the immediate post-drawdown period (Keith et al., 2016). Moreover, Snyder et al. (2006) noted a distinct transition in the reservoir sedimentation rate upon the closure of a major upstream dam in the 1970s, which is an important influence to consider in Lake Seminole given that the Chattahoochee River system includes several additional dams upstream.

Following the 2013 Colorado Front Range flood that accelerated the advancement of the reservoir delta in Ralph Price Reservoir detailed in Rathburn et al. (2017), high discharges and reservoir drawdowns prograded the delta 200 m and deposited three times the volume of sediment that was deposited during the flood (Eidmann et al., 2022). Initially, the delta topset aggraded and the foreset prograded during high discharges that mobilized flood sediments stored in the channel; however, comparable rates of delta progradation also occurred during reservoir drawdowns because the incision of the delta topset served as a source of sediment for foreset progradation (Eidmann et al., 2022). This link between post-disturbance channel and delta sediment sources and the influence of fluctuating reservoir levels on sediment redistribution are important to consider as high magnitude disturbances occur more frequently with climate changes and fluvial systems are forced to adapt to higher levels of hydroclimatic variability. However, one of the benefits of studying Lake Seminole is that it is a highly-managed reservoir system with minimal fluctuations in water level, so it is not necessary to consider the influence of these types of disturbances and drawdowns. Instead, Lake Seminole provides an opportunity to focus on first-order questions about delta sedimentation under stable base level conditions.

Coring of reservoir sediment following the removal of the Glines Canyon Dam on the Elwha River in Washington revealed that Lake Mills, like Ralph Price Reservoir and Englebright Lake, was defined by a Gilbert-style delta that prograded more than a kilometer into the reservoir during the dam's operation (Randle et al., 2015). Downstream of Lake Mills, Lake Aldwell was also characterized by a Gilbert-style delta, and reservoir drawdowns of as little as 3 m were capable of triggering delta progradation and channel degradation across the width of the reservoir,

redistributing the delta sediment and eventually reducing reservoir storage capacity by more than 70% prior to the removal of the Glines Canyon Dam (Randle et al., 2015).

In opposition to the Gilbert-style delta model is Lake Powell, the second largest reservoir in the United States, where underflow density currents and subaqueous gravity flows transport sediment along the lakebed after deposition, moving coarse-grained ($\sim 300 \mu\text{m}$) sediments horizontally into areas at the front of the delta where fine ($\sim 20 \mu\text{m}$) sediments are settling from above (Wildman et al., 2011). Similarly, in Lake Mead, the Colorado River deposits sand in the delta's topset and foreset beds, but muddy turbidity currents plunge over the sandy foreset bed before depositing bottomset sediment (Kostic et al., 2002). This means the overriding turbidity currents can lower the foreset angle, or rather, the angle of deposition of the sand-grained flow. Flume experiments conducted by Kostic et al. (2002) indicated this mechanism of deposition could lower the angle of deposition to as low as 1° , as is the case in Lake Mead where the maximum slope of the foreset bed is slightly below 1° . Following Bates (1953), the reservoir deltas in Lake Powell and Lake Mead are consistent with hyperpycnal inflow patterns.

Moreover, research has found that reservoir deltas can transition between homopycnal and hyperpycnal depositional patterns after experiencing a disturbance that shifts the density gradient at the upstream end of the reservoir. For example, highly turbid floodwaters can create a hyperpycnal delta in the Ronghua Reservoir in Taiwan, but because the small reservoir rapidly becomes turbid during flood events, the density contrast between the incoming and receiving flows decreases, and the delta morphs into a Gilbert-style delta as the characteristic steep slope progrades directly over the upper foreset of the hyperpycnal delta (Lai and Capart, 2009). These studies of reservoir sedimentation underscore that recognizing and understanding both exogenic—outside the reservoir—and endogenic—within reservoir—influences on reservoir sedimentation is key to interpreting and predicting changes in sedimentation within individual systems, especially related to the foci of sediment routing and deposition, delta morphology, and the distribution of sediment grain sizes within a delta.

1.2 Upstream Impacts of Reservoirs

Though the downstream impacts of dams have been widely studied, comparatively little is known about the upstream impacts of dams and even less is known about the dynamic zone where a stream entering a reservoir can incite delta formation. In hydrology, when a river is near an ocean, lake, or other feature that sets its base level, the section of the river influenced by the conditions at its mouth is often called a backwater (Langbein and Iseri, 1960). Fluvial geomorphologists studying the upstream impacts of reservoirs have adopted the same terminology to describe the “backwater zone” where the hydrology and morphology of an upstream reach of a river is influenced by the presence of a reservoir downstream and the new local base level established by the dam (Evans et al., 2007; Liro, 2017; Volke et al., 2019).

As a delta progrades into a reservoir, the backwater zone aggrades upstream into the river’s former floodplain and represents a fluvial transition zone between the lotic river system and lentic reservoir pool (Volke et al., 2019). The four functional zones of reservoir deltas described in Volke et al. (2015) are a useful framework for understanding the riverine and lacustrine processes that occur in backwaters (Figure 4). The fluvial-delta transition zone is located farthest upstream and is characterized by increased flooding and sediment deposition; the subaerial delta zone exists between the reservoir’s maximum and mean water levels and is characterized by the presence of geomorphic features like channel levees and point bars; the subaerial-subaquatic transition zone is located between the reservoir’s mean and minimum water levels and is characterized by sediment deposition during high water levels and fluvial processes during low reservoir water levels; and the subaquatic reservoir zone is located below the minimum reservoir pool boundary, so it contains the portion of the delta that is permanently inundated by the reservoir (Volke et al., 2015).

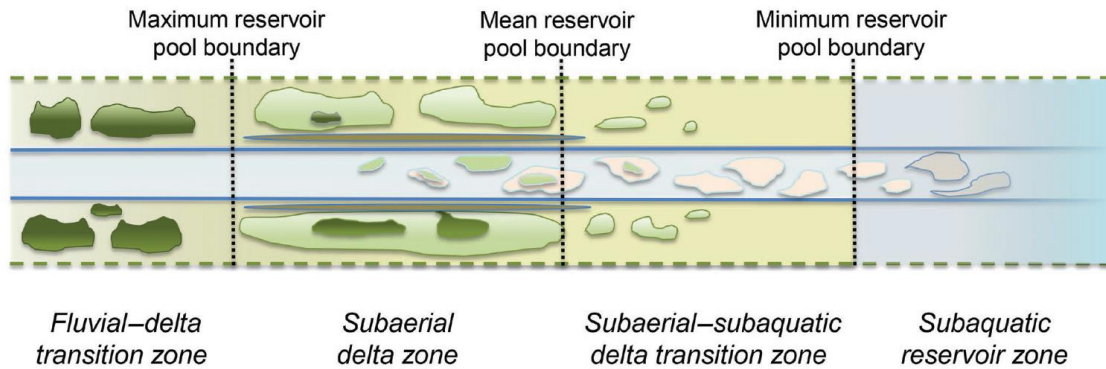


Figure 4. Diagram of the four morphologic zones of reservoir deltas. The green patches represent vegetation and the linear features in the subaerial delta zone represent levees and depositional bars (from Volke et al., 2015).

In the backwater zone, water level fluctuations stemming from the reservoir can induce sediment deposition in the river channel and floodplain, increase groundwater levels, lead to more frequent and extreme floodplain inundation, facilitate the deposition of pollutants and modify channel morphology and riparian vegetation (Csiki and Rhoads, 2010; Liro, 2019; Xu, 1990). These decreases in channel area can increase the flood risk for populations living in the alluvial plain upstream of a reservoir. For example, upstream aggradation following the construction the Cantillana Dam in Spain meant that higher water levels were reached for the same river discharge values: both flood height and duration increased for discharges 20-23% lower than pre-dam values (Baena-Escudero et al., 2021). Furthermore, the loss of recreational access to reservoirs by boaters is another well-documented impact of sedimentation because boat ramps are often located in or near the backwater zone at the upstream end of reservoirs (Morris et al., 2023).

Xu (1990) was one of the first studies to detail the upstream impacts of dams and, using observations on the Weihe River upstream of the Sanmenxia Reservoir in China, Xu created a three-stage model to describe channel adjustment upstream of a reservoir following base level rise. In the first stage of the model, base level rise at the dam triggers aggradation concentrated within the river channel, which decreases the height of the floodplain relative to the channel and leads to more frequent overbank flooding and sediment deposition in the floodplain. In the second

stage of the model, the increased height of the floodplain relative to the channel bed decreases the frequency of overbank flooding, which decreases the coarser sediment deposits in the floodplain and the occurrence of the meander cutoffs, thus increasing channel sinuosity. In the final stage, the channel system enters a new equilibrium as sinuosity tends toward a constant. Because the content of fine sediment increases significantly during the adjustment, the final channel is narrower, deeper, and more sinuous than the initial channel (Xu, 1990).

Similar channel narrowing was identified in the backwater zone of a flood-control reservoir in Poland where sediment accumulation increased channel sinuosity and narrowed the formerly braided channel into single, stable channel planform. However, a single channel tributary also within the reservoir's backwater zone only experienced planform stabilization, leading researchers to hypothesize that the magnitude of channel morphology change in the backwater zone is controlled by the space available, in terms of channel width and area, to accommodate fine sediment deposition (Liro, 2017; Liro, 2019). Moreover, an analysis of river channel evolution upstream of a low head dam on the Huron River in Ohio also found that sinuosity increased and channel capacity decreased due to sediment deposition following dam construction (Evans et al., 2007).

Biotic components of backwater zones have also been found to have significant impacts on sedimentation and channel adjustment. In an analysis of the succession of the floodplain ecosystem on the Laohahe River following the construction of the Hongshan Reservoir, Xu and Shi (1997) found that the establishment of dense aquatic weeds pushed sediment deposits farther upstream into the backwater zone. In the first few years following dam construction, a delta formed at the upstream end of the reservoir and progressively advanced towards the dam with ongoing sedimentation; however, once aquatic weeds colonized the backwater zone, they intercepted a large portion of the incoming sediment and dramatically slowed delta progradation. This dynamic could be an important consideration when analyzing sedimentation in Lake Seminole since the reservoir is dominated by dense populations of invasive weeds.

Chapter 2: Lake Seminole and the ACF River Basin

2.1 Lake Seminole

Lake Seminole is a shallow, 123 km² surface-water impoundment located at the confluence of the Chattahoochee and Flint Rivers in Florida and Georgia. It was formed in 1954 by the USACE's construction of the Jim Woodruff Lock and Dam, which stands 28 m high (Figure 5). The lock and dam were authorized under the River and Harbors Acts of 1945 and 1946 were constructed to improve navigation of the Chattahoochee and Flint Rivers, as well as the Apalachicola River downstream of their confluence, and to generate hydroelectric power (Tetra Tech, 2016; Torak et al., 2005). Later legislation has expanded these purposes to include recreation, water quality, and fish and wildlife conservation, including the conservation of federally listed threatened and endangered species and their critical habitat (Tetra Tech, 2011). From west to east bank, the key features of the Jim Woodruff Lock and Dam are a fixed-crest spillway, a navigation lock, a concrete gated spillway, a powerhouse, and an earthen overflow dike (Figure 6).

Construction of the dam and navigation lock began in 1947, the lock was opened to navigation in May 1954, and the powerhouse began operating in February 1957 (Tetra Tech, 2016). Water was first impounded in the reservoir in May 1954 at an elevation of 19.8 m. The elevation was then lowered to 15.8 m in July 1954, raised to 20 m in April 1955, and finally filled to 23.4 m in January 1957 (Tetra Tech, 2016). Since then, the reservoir has been operated with a normal upper pool elevation of 23.4 m with maximum fluctuations between 23.1 and 23.7 m. Channel dredging in the Chattahoochee and Apalachicola Rivers from Columbus, Georgia to the Gulf of Mexico was another significant component of the USACE's navigation project, so, beginning in the 1950s, the quantity of material dredged in the basin increased exponentially compared to the previous century (Mossa and Chen, 2022).

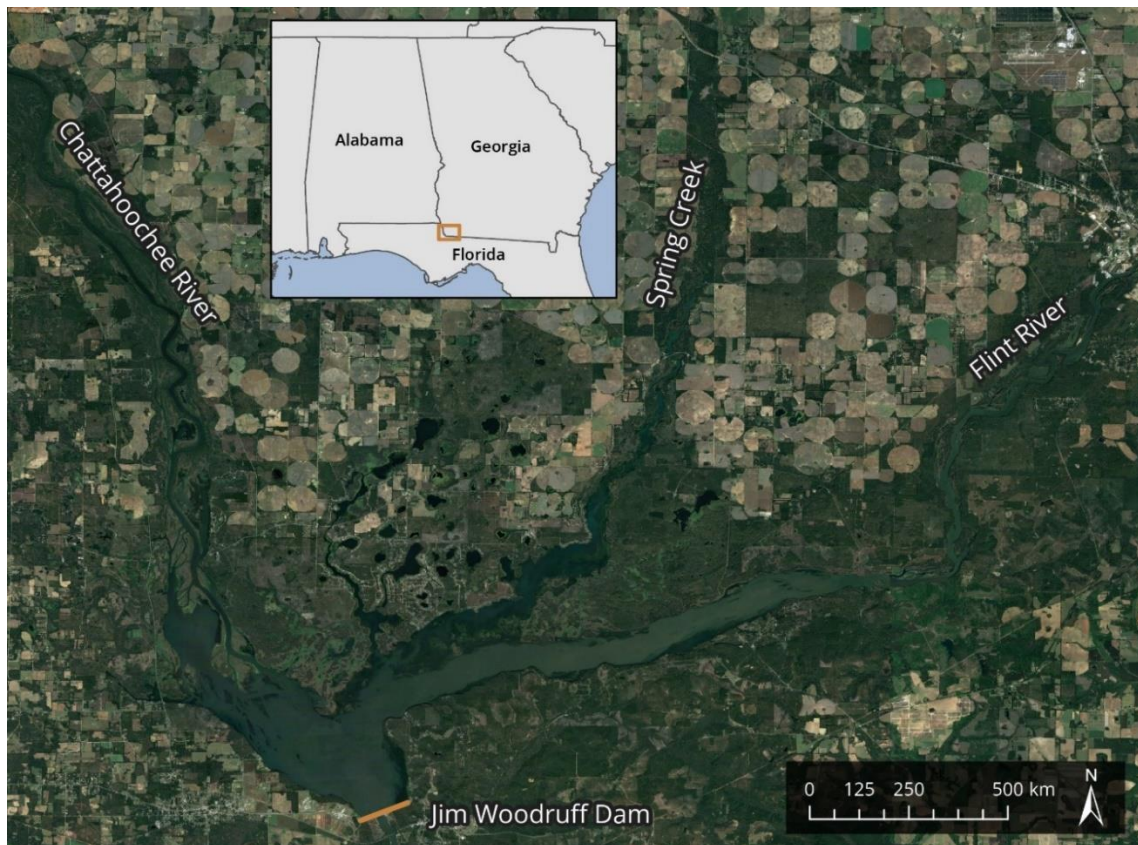


Figure 5. Aerial image of Lake Seminole and the Jim Woodruff Dam (2023). (Data source: Airbus)

Lake Seminole is located in a subtropical climate region. The coldest months of the year, December and January, averaged 12.2 degrees Celsius ($^{\circ}\text{C}$) over an 18-year period (2005–2023) at a NOAA data station in Bainbridge, GA. The warmest months, July and August, averaged 27.6 $^{\circ}\text{C}$ over the same period. Occasional freezing temperatures occur during otherwise mild winter months and temperatures around 38 $^{\circ}\text{C}$ are not uncommon during the summer. The mean annual air temperature for a 66-year period (1957–2023) using data from stations located at Colquitt, GA and Bainbridge, GA, is 19.6 $^{\circ}\text{C}$.

The average annual precipitation in the Tallahassee area for the 62-year period from 1960–2022 was 1578 mm/yr. In 2022, the highest monthly rainfall at Bainbridge, GA occurred during March, with a total of 220 mm, and the lowest monthly rainfall occurred during September, with a total of 27 mm. This is consistent with trends in the climatic data record from

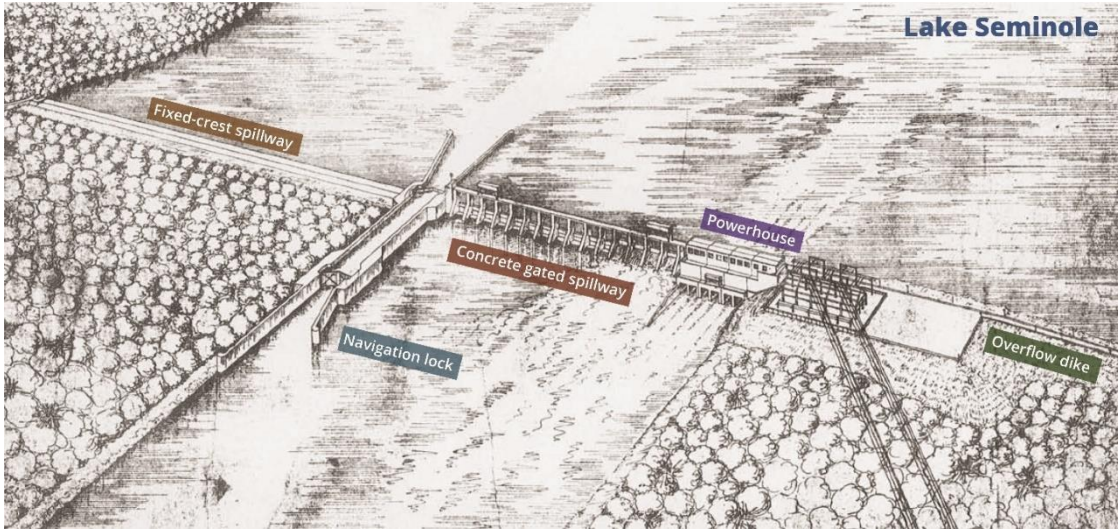


Figure 6. Illustration of the Jim Woodruff Lock and Dam. Adapted from USACE (1952)

1957–2023 that show March being the wettest month of the year, and September and October being the driest months of the year. Annual precipitation in the Lake Seminole region during 2022 was about 1483 mm, which is close to the 62-year average for the region (NOAA; Torak et al., 2005).

During the warmer months, thunderstorms are a major producer of rainfall, and the region is also affected by tropical storms and hurricanes. In July 1994, Tropical Storm Alberto made landfall near Ft. Walton, Florida before moving up to the Atlanta area and then meandering southward. During the storm, up to 660 mm of rainfall occurred in areas between the Chattahoochee and Flint Rivers (Tetra Tech, 2016). It is important to note that the Jim Woodruff Dam does not provide flood risk management operations; during large flood events, regulated releases from the dam are used to reduce peak flows (Tetra Tech, 2016). In October 2018, Lake Seminole was again hit by a powerful storm: Hurricane Michael made landfall near Panama City, Florida as a Category 5 hurricane before weakening into a tropical storm as it crossed over Georgia. The storm winds uprooted trees along the banks of the reservoir and wiped out entire swaths of aquatic vegetation; shallower areas of the channel also showed signs of having been scoured by wind and waves carrying sediment and debris (White, 2019).

In terms of geology, Lake Seminole is located in the Coastal Plain physiographic province, and the surrounding area is comprised of three regions: a flat karstic region at the northern end of the reservoir, a Piedmont region of dissected rolling hills with remnant plains, and a low-lying coastal sediment region. Though the reservoir itself is located in the Coastal Plain, much of its drainage area is located in the Piedmont region, which consists of moderate- to high-grade metamorphic rocks like schists and migmatites as well as igneous rocks like granite (Figure 7). The Coastal Plain consists of sedimentary rocks and sediment eroded from the Piedmont over the last 100 million years as well as limestones generated by marine organisms (Tetra Tech, 2016).

Furthermore, Lake Seminole is underlain by the Upper Floridian aquifer, the largest aquifer in the southeastern United States and the primary source of water for domestic and agricultural uses in most of north and central Florida. Soils in the Coastal Plain are often porous, which permits flow through the ground, and there is evidence that Lake Seminole contributes inflow into the Upper Floridian aquifer via sinkholes and reverse springs in the lake bottom (Torak et al., 2005). In addition, limestone caves were discovered during dam construction, and the solutioning and chemical weathering of the limestone comprising the reservoir bottom promotes this leakage and groundwater inflow (Tetra Tech, 2016; Torak et al., 2005). Despite the limestone dissolution, Torak et al. (2005) found a low potential for sudden sinkhole collapse and lake drainage, except near the dam where the 9 m difference in water level between the Apalachicola River and Lake Seminole establishes the potential to form relatively high hydraulic gradients.

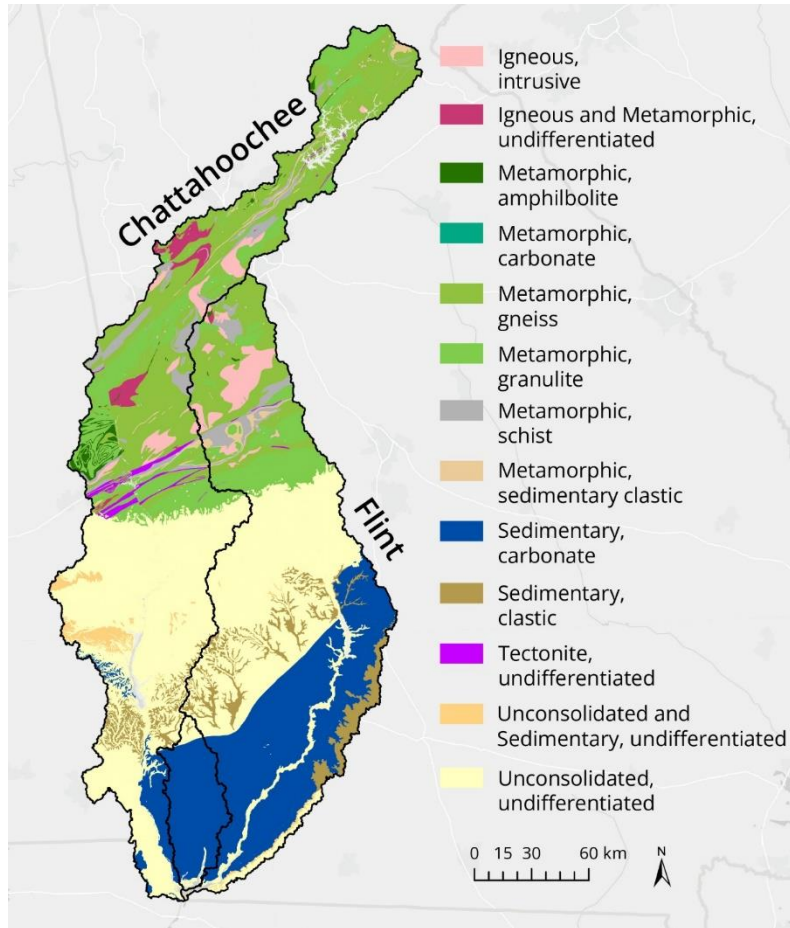


Figure 7. Geologic map of the Lake Seminole watershed. From east to west, the three sub-watersheds outlined in black are the Chattahoochee, Spring Creek, and Flint basins.

In terms of prior work completed in Lake Seminole, in 2011, the USACE contracted Tetra Tech to complete a sedimentation and erosion analysis for the reservoir using bathymetric cross sections that were surveyed at a network of rangelines established during dam construction. Cross section surveys were collected in 1957, 1976, 1988-89, and 2009 at 40 different stations throughout the reservoir and up the Chattahoochee and Flint Rivers. Tetra Tech (2011) found that bank erosion was not a major problem within Lake Seminole, but it did increase farther upstream as the lentic reservoir ecosystem transitioned to the lotic ecosystem of the Chattahoochee and Flint Rivers. In terms of sedimentation, the dominant location of sediment deposition was the actively prograding delta in the Chattahoochee arm of the reservoir. The Flint arm of the reservoir was relatively unimpacted by sedimentation aside from one cross section near the upstream end

of the reservoir that showed extreme sediment deposition (~5 m) between 1988 and 2009. Tetra Tech (2011) was able to use aerial photos to confirm that the source of this sedimentation was dredged material deposited sometime between 1993 and 1999.

Regarding the difference in sedimentation between the Chattahoochee and Flint arms of the reservoir, Tetra Tech (2011) hypothesized that the geologic differences between each drainage basin could be responsible: the Chattahoochee watershed has a greater clastic sediment load relative to the Flint, which has more carbonates that dissolve instead of eroding (Figure 7). Another possible explanation is that the Flint River has undergone more extensive dredging than the Chattahoochee River.

Previous research on Lake Seminole has focused not only on physical processes within the reservoir, but also on chemical and biological monitoring. In terms of biological monitoring, the reservoir is dominated by dense populations of macrophytes, and invasive species like hydrilla (*Hydrilla verticillate*), Eurasian milfoil (*Myriophyllum spicatum*), and water hyacinth (*Eichornia crassipes*) have all become well established (Waters et al., 2015). Non-native plant growth in the reservoir has degraded water quality by decreasing dissolved oxygen and increasing nutrient levels and adversely affected reservoir operations by interfering with recreation area usage, decreasing navigability, and blocking hydropower intake structures (Tetra Tech, 2016).

Though the USACE has documented over 900 species of aquatic plants at Lake Seminole, hydrilla has exhibited the most prolific growth (Tetra Tech, 2016). A number of chemical, biological, and mechanical aquatic plant management techniques have been implemented in the reservoir since 1957; however, none have been successful in controlling hydrilla growth (Tetra Tech, 2016). From 1994 to 1998, USACE developed a Hydrilla Action Plan that included the application of herbicides and the use of sterile grass carp (*Ctenopharyngodon Idella*) and hydrilla flies (*Hydrillae pakistani*) for biological control in an attempt to control the spread of the vegetation (Eubanks and Morgan, 2001).

2.2 Apalachicola-Chattahoochee-Flint (ACF) Basin

The Apalachicola–Chattahoochee–Flint (ACF) river basin has a drainage area of 50,504 km², making it the largest river that drains into the eastern Gulf of Mexico and the fifth largest outflow of water in the continental United States (Mossa and Chen, 2022; Waters et al., 2015). At the USGS gauging station closest to the Jim Woodruff Dam, Lake Seminole has a drainage area of 44,288 km². Where they enter Lake Seminole, the Chattahoochee River has a drainage area of 21,600 km² and the Flint River has a drainage area of 19,386 km² (Figure 8). Also of note in the ACF basin is Spring Creek: a Flint River tributary with a drainage area of 1,269 km² that enters Lake Seminole approximately 10 km upstream of the Flint River’s confluence with the Chattahoochee River.

Moreover, the ACF basin extends across three states—Georgia, Florida, and Alabama—and water-allocation negotiations between these neighbors have been tense since the early 1990s when all three states found their populations booming (Torak et al., 2005). The Chattahoochee and Flint Rivers are critical water sources for Georgia and Alabama and increased upstream water consumption from these rivers directly impacts the Apalachicola River and its diverse aquatic biota downstream in Florida (Darst and Light, 2008; LoCascio, 2015). This conflict is a point of interest in an analysis of reservoir sedimentation since, at a fundamental level, reservoirs are created to impound and divert water, not sediment, and increased sediment accumulation rates could impact the delivery of vital nutrients and detritus to Apalachicola Bay’s shellfish and oyster populations, which are a cornerstone of the regional economy (Bricker et al., 2008; LoCascio, 2015).

In fact, previous research has identified the Jim Woodruff Dam as a primary cause of incision in reaches of the Apalachicola River downstream of the dam due to the diminished sediment supply (Darst and Light, 2008; Light et al., 2006). Light et al. (2006) examined the water level in a reach of the Apalachicola River downstream of Lake Seminole and found that it

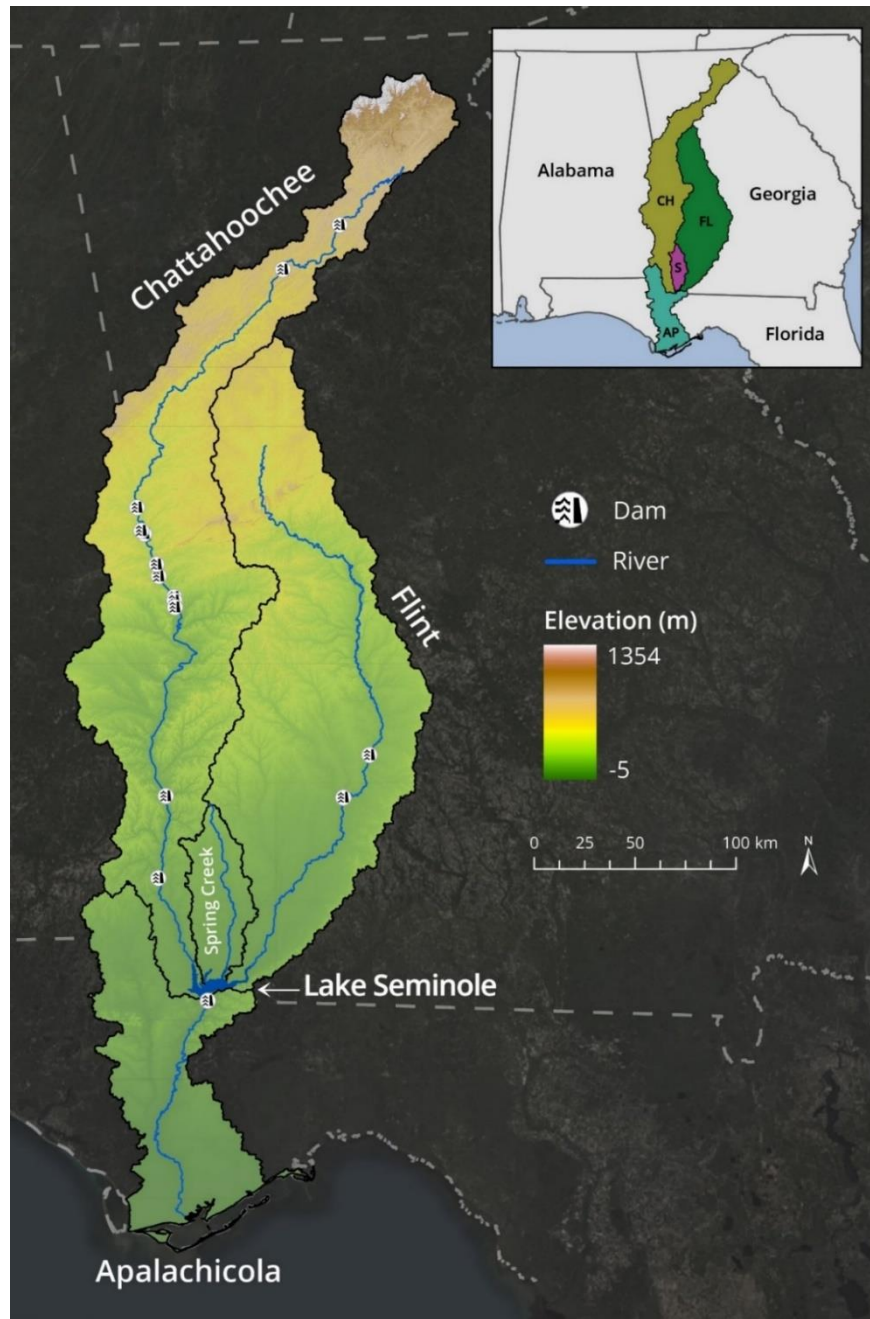


Figure 8. Location of Lake Seminole and the boundaries of the ACF river basin. In the inset map, CH=Chattahoochee, FL=Flint, S=Spring Creek, and AP=Apalachicola.

decreased 1.5 meters between 1954–2004 because of changes in the channel bed and geometry following dam construction. In a recent update, Mossa and Chen (2022) found that water level at that location has continued to decline through the present day and has negatively impacted river-floodplain connectivity. The Apalachicola River provides critical habitat for four endangered

species (Gulf sturgeon and three mussel species), and the U.S. Fish and Wildlife Service has recognized that decreased sediment load and channel straightening have been key factors in these species' habitat disturbance (Jackson and Pringle, 2010). However, new research has also documented aggradation in the tidal reach downstream of the dam as well as the accretion of the Apalachicola River delta, attributing this sediment gain to the removal of bed and bank sediment in the upstream zones of degradation close to the dam (Mossa and Chen, 2022).

Upstream of Lake Seminole, though the Flint and Chattahoochee watersheds are similar in size, they differ on a number of key characteristics, including the dominant geology (Figure 7) and land use type. The Chattahoochee River has 12 dams on its mainstem—making it the most intensely regulated water system in the state of Georgia—and encompasses both Atlanta and Columbus, meaning that the river experiences large sediment inputs from urban and agricultural erosion, but also that much of that sediment is trapped by dams upstream of Lake Seminole (Figure 8). On the other hand, the Flint River only has two dams and is dominated by rural and agricultural land use. Additionally, the Flint River is spring-fed and relatively clear, especially in comparison to the Chattahoochee River (Tetra Tech, 2016). In fact, a USACE study conducted in 1980 found that the Chattahoochee River was generally two to three times as turbid as the Flint River but had lower total dissolved solids (Torak et al., 2005). Though no definitive conclusions can be drawn about the relative influence of each of these factors on sedimentation—or lack thereof—in the Chattahoochee and Flint arms of Lake Seminole, these differences are important to keep in mind while conducting a comprehensive analysis of subaerial and subaqueous sedimentation patterns in the reservoir.

2.3 Research Questions and Objectives

In examining Lake Seminole, this project aimed to investigate the processes of sediment deposition in reservoirs and characterize the geomorphology of the resulting reservoir delta. In particular, this project sought to answer the following questions:

- 1) Where and at what rates is sediment accumulating in Lake Seminole?
- 2) How do current sedimentation rates compare to past sedimentation rates?
- 3) What environmental factors have influenced sedimentation rates and depositional patterns?

In order to address these questions, three main research objectives were identified, and each objective is presented in its own chapter as a separate analysis. Chapter 3 presents subaerial aggradation rates for the Chattahoochee River delta calculated by differencing repeat lidar surveys collected in 2007 and 2018. Chapter 4 details historical and recent subaqueous sedimentation rates in Lake Seminole measured by calculating changes in bed elevation using bathymetric cross section data collected from 1957–2009 and reservoir-scale bathymetric surveys collected in 2009 and 2023. Chapter 5 includes an assessment of 30 years of land-cover change (1993–2023) in the Chattahoochee, Flint, and Spring Creek watersheds performed by creating a multi-date Landsat image and conducting a supervised land cover classification. Conclusions for the study overall are presented in Chapter 6.

Chapter 3: Tracking Subaerial Delta Sedimentation Using Lidar Topographic Differencing

3.1 Introduction and Background

High-resolution topography (HRT) is any topographic dataset that, in its raw form, consists of location and elevation measurements stored in a point cloud with an average spatial resolution of at least 1 point/m² (Passalacqua et al., 2015). HRT data can be obtained using a variety of different techniques including Light Detection and Ranging (lidar), Synthetic Aperture Radar (SAR), Structure from Motion (SfM), and Sound Navigation and Ranging (sonar) (Passalacqua et al., 2015). Rapid advances in HRT in recent decades have facilitated improved characterizations of various ecologic, geomorphic, and hydrologic processes, and one of the most common techniques that uses HRT to evaluate these earth-surface processes is topographic differencing. Topographic differencing is the process of measuring landscape change by comparing HRT datasets acquired at different dates.

For this project, lidar topographic differencing was used to track changes in subaerial sedimentation on the Chattahoochee River delta between 2007–2018. There are two main types of topographic differencing: vertical differencing, which operates in two dimensions and most often entails the raster subtraction of digital elevation models (DEMs), and three-dimensional (3D) differencing, which operates in three dimensions using point clouds without the need to grid the data to a raster format. In this study, two different types of vertical differencing—DEM and point cloud—were used to analyze changes in sedimentation on the Chattahoochee River delta.

3.1.1 DEM Differencing

The first type of topographic differencing is vertical differencing, which is used to measure topographic change in two dimensions. Vertical differencing is useful for capturing processes like floods and landslides and is most appropriate in scenarios where the surface change is predominantly vertical, like river erosion, rather than translational, like earthquakes. In the

topographic differencing literature, vertical differencing is often used synonymously with DEM differencing (Scott et al., 2021); however, some newer 3D differencing methods can also be used in 2D to perform vertical differencing on point clouds, which is detailed further in the next section (Lague et al., 2013). This section is focused on DEM differencing, which involves rasterizing both HRT point clouds to identical horizontal grids and then subtracting the values stored in each cell, as shown in Figure 9.

The most common way to produce a DEM from a point cloud is by using a triangular irregular network (TIN) approach to link the sample points into a set of triangles. The TIN surface is then interpolated into a raster of a specified cell size, or spatial resolution. The resulting accuracies usually vary between the source lidar and the final DEM because the process of averaging several lidar points within each cell can result in slightly different elevation values when compared to the survey checkpoints. Producing a DEM at too fine a spatial resolution can also enhance these errors, so the optimal spatial resolution of a DEM is dictated by the size of the point cloud and is obtained using the point density of the lower-resolution HRT dataset (Scott et al., 2021):

$$SR = \frac{1}{\sqrt{\text{point density}}} . \quad (1)$$

Moreover, DEM differencing must be performed using DEMs in the same horizontal and vertical coordinate systems. In order to produce a DEM of Difference (DoD), the earlier, or compare, dataset is subtracted from the later, or reference, dataset. Resulting values below a minimum level of detection (E_{MLOD}) are masked out of the DoD. For a DEM vertical uncertainty ∂Z , the minimum level of detection is found using the following equation (Brasington et al., 2003):

$$E_{MLOD} = \sqrt{\partial z_{reference}^2 + \partial z_{compare}^2} . \quad (2)$$

This is one of the simpler methods of estimating DoD error because it requires that the DEM errors are random and independent of landscape type. Wheaton et al. (2010) details more complex error calculation methods that can be used when the signal from the HRT is not significantly larger than the error in the datasets. In the absence of vertical uncertainty information for the DEMs, the recommended E_{MLOD} is 0.5 m, which corresponds to a standard ∂z of 0.35 m for both DEMs (Scott et al., 2021).

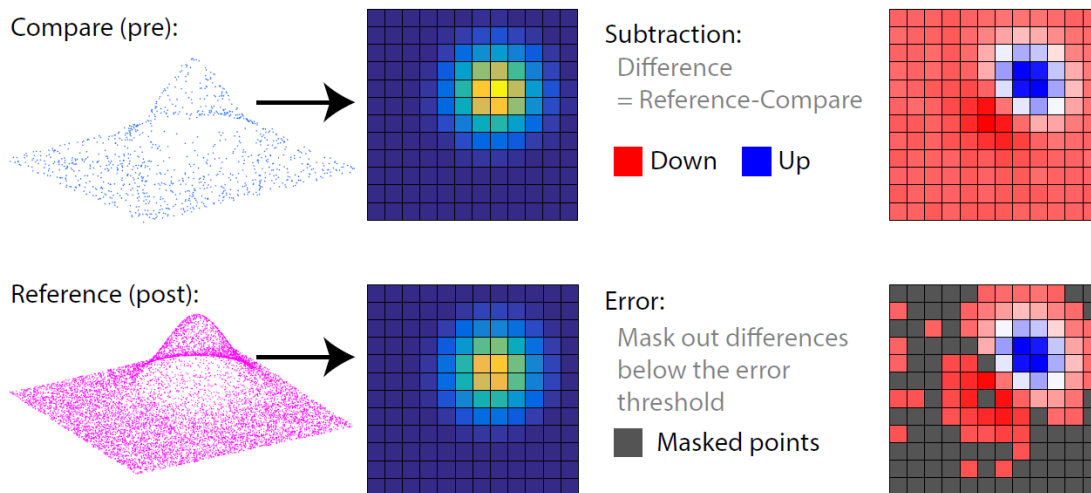


Figure 9. DEM differencing methodology. In order to produce a DoD, the compare dataset is subtracted from the reference dataset and resulting values below a minimum level of detection are masked out (from Scott et al., 2021).

3.1.2 Multiscale Model-to-Model Cloud Comparison

The second type of topographic differencing is 3D differencing, which analyzes topographic change using point clouds instead of DEMs. There are a variety of different algorithms available for 3D differencing, but the Multiscale Model to Model Cloud Comparison (M3C2), which calculates cloud-to-cloud separation in the surface-normal direction, is the most useful for this project because the algorithm is available in the open source software package CloudCompare (cloudcompare.org) and has previously been applied to measure geomorphic change in a prograding delta (Lague et al., 2013; Wagner et al., 2017). Moreover, the M3C2

method includes a spatially variable error calculation in the differencing scheme (Lague et al., 2013).

Though the M3C2 algorithm was designed for use in complex 3D differencing cases, it has also been applied in simpler 2D cases as a more robust alternative to DEM differencing. Transforming a point cloud into a continuous elevation surface like a DEM increases both horizontal and vertical uncertainty, which results in a loss of accuracy in change detection (Passalacqua et al., 2015). Working directly on point clouds mitigates these surface representation errors, preserves the 3D point uncertainty, and allows for the extraction of more detailed information from the dataset, like vegetation classification (Passalacqua et al., 2015). However, working with point clouds is generally considered to be more challenging and less intuitive than working with gridded data like DEMs, which is part of what Lague et al. (2013) aimed to address with the creation of the M3C2 method.

There are two steps in the M3C2 algorithm: (1) surface normal estimation and orientation in 3D and (2) measurement of the mean surface change along the normal direction and the calculation of a local confidence interval. Figure 10 depicts the M3C2 algorithm and the two user-defined parameters D (normal scale) and d (projection scale). Calculations are performed over a series of “core” points representing the region of interest, which will generally be a sub-sampled version of the point cloud, but can also be the entire cloud. In step one, for any given core point i , a normal vector is defined by fitting a plane to the neighbors that fall within a $D/2$ radius of i . The standard deviation of the distance of the neighbors to the best fit plane is used as a measure of the cloud roughness ($\sigma_i(D)$) surrounding i . In step two, two sub-clouds are defined by the intersection of the reference and compare clouds with a cylinder of diameter d and axis (i, \vec{N}) . Each sub-cloud is then projected on the cylinder axis to produce a distribution of distances, and the mean of the distribution gives the average position (i_1 and i_2) of each cloud. The standard deviation of each cloud ($\sigma_1(d)$ and $\sigma_2(d)$) serves as a local estimate of the point cloud roughness. If outliers like vegetation are expected in the point cloud data, i_1 and i_2 can instead be defined as

the median of the distance distribution and the point cloud roughness can be measured using the inter-quartile range of each cloud. Lastly, the local distance between the two clouds $L_{M3C2}(i)$ is given by the distance between i_1 and i_2 (Lague et al., 2013).

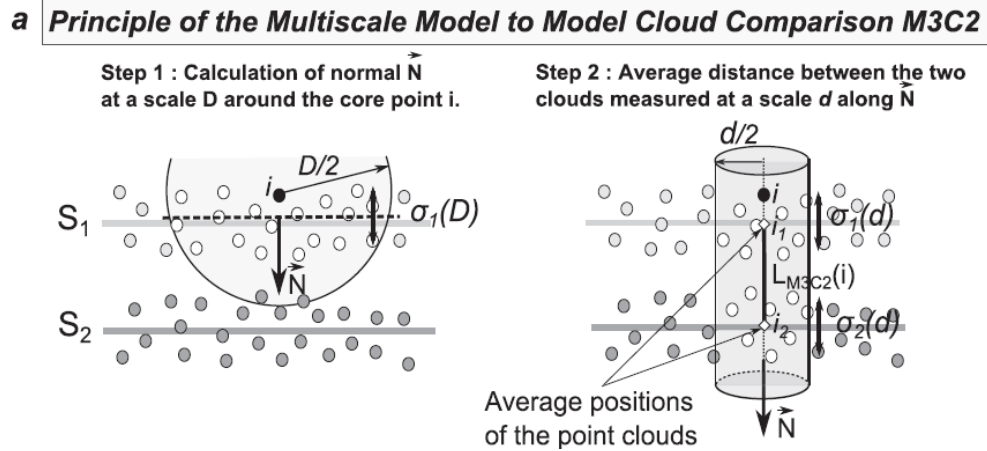


Figure 10. Visualization of the two key steps in the M3C2 algorithm using cloud 1 (S_1) and cloud 2 (S_2). In the first step, the normal is estimated from the first point cloud and, in the second step, the average surface change is measured along the normal direction and a local confidence interval is estimated (from Lague et al., 2013).

In addition to its applications in 3D differencing, the M3C2 method can also be used as a direct substitute for DEM differencing by using a grid of core points, imposing a vertical normal, and setting the projection scale (d) to be slightly larger than the grid spacing. This produces a grid of points with scalars (vertical difference, the limit of detection, significance of change, and roughness) attached to them, which can be turned into raster grids (Lague et al., 2013). This vertical normal method was the M3C2 application used in this project.

3.1.3 Lidar Ground Filtering

Vegetation is difficult to accurately capture and filter in lidar data and, in locations with moderate to high vegetation density, can be the largest source of uncertainty in the dataset (Passalacqua et al., 2015). This is a principal concern when working with lidar data collected in a wetland environment like a reservoir delta. Lidar systems work by measuring the amount of time it takes for pulses of light emitted from a rapidly firing laser to travel to the ground and back to

the sensor. The sensor records when the light leaves and returns and the amount of time between these two values is used to calculate the distance the light traveled, which is then converted to elevation (Meng et al., 2010). Importantly, almost all lidar applications require a process called ground filtering to determine which lidar returns—reflections of light back to the sensor—are from the ground surface and which are from non-ground surface features like vegetation. Making this distinction can be a significant challenge in areas with a high level of surface variability, and features like shrubs, bridges, and jagged, hilly edges often pose a problem for ground filtering algorithms (Lague et al., 2013). Not only shrubs, but any dense vegetation < 5 m in height is a common source of error that often gets mislabeled as ground points because the difference in slope and elevation between the vegetation and neighboring ground points is similar to the difference between ground points and neighboring ground points (Meng et al., 2010). Because these low-lying features are difficult for automated algorithms to detect as non-ground, they often have to be manually removed from the ground classification (Dewberry, 2019).

Not only is vegetation challenging to filter, but it can also interfere with a lidar sensor's ability to capture the true ground surface. It can be difficult for a lidar pulse to penetrate heavy vegetation, which can result in an inaccurate bare earth surface due to a lack of lidar returns from the ground beneath the vegetation (Dewberry, 2019). Even where light is able to reach true ground level, dense vegetation can also disrupt the return of the laser pulse (Zhao et al., 2023). This means that areas of vegetation with poor penetration capability can result in overestimated surface elevations in lidar data. This effect has been documented in deltaic and boreal wetland environments (Hopkinson et al., 2005; Töyrä et al., 2003); peatlands (Luscombe et al., 2015); and ecosystems dominated by grasses and shrubs (Kucharczyk et al., 2018; Sankey et al., 2017; Zhao et al., 2023). These studies have shown that lidar accuracy varies with vegetation type and the consensus is that factors like vegetation orientation, structure, height, and density can all influence the likelihood of laser pulses reaching and reflecting from the true ground surface (Kucharczyk et al., 2018). In addition, an analysis of vegetation class-dependent errors in lidar

ground elevations collected in a wetland ecosystem found that aquatic vegetation was associated with the largest errors because of the ground cover present beneath the vegetation (Hopkinson et al., 2005). Most aquatic vegetation is underlain by either open water or saturated organic soils and both surfaces reflect poorly in the near-infrared portion of the light spectrum, which lidar sensors operate in, so the likelihood of obtaining a true ground return is reduced relative to drier, more reflective surfaces (Hopkinson et al., 2005).

With all of this background in mind, the key research questions this study aimed to answer were:

- 1) At what rate did subaerial sediment accumulate on the Chattahoochee River delta between 2007–2018?
- 2) What region of the delta was this deposition focused in, both in terms of downstream distance and the location within the individual wetland islands?
- 3) What are the advantages and disadvantages of using point cloud and DEM differencing to measure topographic change in a reservoir delta environment?

3.2 Methods

3.2.1 Datasets

3.2.1.1 2007 Lidar Survey

The 2007 lidar dataset was collected from November 12, 2007–January 20, 2008 by Merrick & Company (Merrick), who were contracted by the Northwest Florida Water Management District (NFWMD). The survey was flown over five counties in northern Florida (Calhoun, Holmes, Washington, Jackson, and Liberty) in order to generate high-resolution data for improved floodplain delineation and hydrologic modeling (Merrick, 2008). The survey covers a total of 5,594 km², has a reported vertical error of 14.8 cm, a reported horizontal error of 100 cm, and a point density of 1.16 points/m² (Table 1). Following data collection, Merrick verified

the raw data and boresighted it to align the flightlines. The purpose of boresight calibration was to correct for minute misalignments between adjacent strips of data that are noticeable in the raw point cloud. After this, the data was parsed into manageable tiles. These tiles then underwent automated filtering in Merrick Advanced Remote Sensing (MARS) lidar processing and modeling software that classified the points into error points, ground points, and canopy or building points. The dataset was then manually reclassified to remove any erroneous points that remained after the auto filter. Merrick delivered the data to NOAA as LAS files containing points classified as bare-earth and canopy (Merrick, 2008). The points available for download on NOAA Digital Coast (coast.noaa.gov/digitalcoast) are classified into two classes: unclassified and ground.

3.2.1.2 2018 Lidar Survey

The 2018 lidar dataset was collected from March 31, 2018–May 10, 2018 by Dewberry, who were contracted by the U.S. Geological Survey (USGS) to produce high-resolution data capable of supporting water resource planning, flood control plans, and the Federal Emergency Management Agency (FEMA) Risk Mapping, Assessment and Planning (Risk MAP) program (Dewberry, 2019). The survey was flown over 28 counties in the Florida panhandle region. The survey covers a total of 7,076 km², has a reported vertical error of 6.7 cm, a reported horizontal error of 18.2 cm, and a point density of 16.25 points/m² (Table 1).

It is important to highlight the difference in resolution between the 2007 and 2018 lidar surveys here: the point cloud collected in the 2018 lidar survey is 14 times as dense as the 2007 survey point cloud. It is also important to note that the 1.16 points/m² number for the 2007 survey reflects the entire 5,594 km² area of survey coverage, and, if only the Chattahoochee River delta islands are considered, then the point density drops even further to 0.92 points/m² because there are some gaps in coverage on the islands (Figure 12). One implication of this is that there is an increased likelihood that the 2018 survey successfully captured the ground surface in vegetated

Table 1. Summary of the metadata for the 2007 and 2018 lidar surveys. WSE=Water surface elevation. LS=Lake Seminole CH=Chattahoochee River. FL=Flint River. AP=Apalachicola River. Q=Stream discharge. The average and maximum values are for the period of survey collection shown in column 2 and were calculated using the streamgage closest to Lake Seminole on each river.

Dataset	Survey Dates	Survey Area (km ²)	Vertical Error (cm)	Horizontal Error (cm)	Point Density (pts/m ²)	Horizontal Datum	Vertical Datum	Point Cloud File Size (GB)	DEM File Size (GB)	LS Avg. & Max WSE (m)	CH Avg. & Max Q (m ³ /s)	FL Avg. & Max Q (m ³ /s)	AP Avg. & Max Q (m ³ /s)
2007 Florida Lidar	11/12/2007–1/20/2008	295	14.8	100	1.16	NAD 83	NAVD88 height (m)	0.56	0.20	23.40	90	105	224
										23.65	300	297	532
2018 Florida Lidar	3/31/2018–5/10/2018	334	6.7	18.2	16.25	NAD 83	NAVD88 height (m)	5.32	0.97	23.44	274	187	522
										23.63	405	265	716

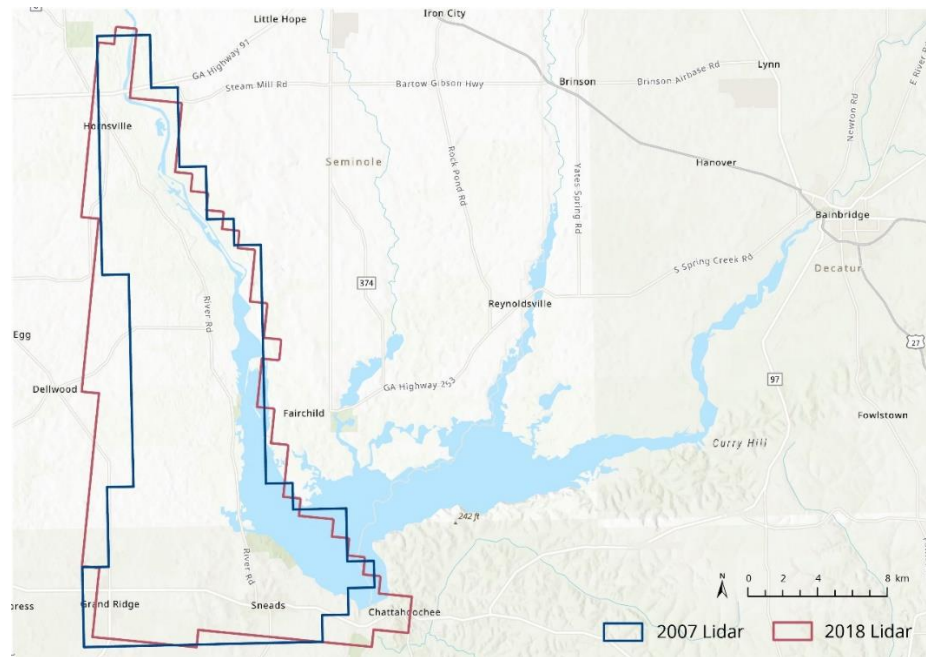


Figure 11. Footprints of the Lake Seminole topographic datasets listed in Table 1.



Figure 12. DEMs of the Chattahoochee River delta generated using the 2007 (left) and 2018 (right) lidar surveys. Both DEMs are underlain by high-resolution National Agriculture Imagery Program (NAIP) aerial photographs taken close to the period of survey collection.

areas where detection can be limited by occlusion because, say, for example, in a 1 m² area of vegetation, the 2018 survey had 14 more chances to capture a return representing the true ground surface. As discussed above, the saturation of the ground surface in wetlands can also influence the likelihood of obtaining a true ground return, so, if there were differences in water level when the 2007 and 2018 surveys were collected, this could result in higher ground elevation errors in the survey collected with the higher water level/ground saturation. However, this is not a concern because the water level in Lake Seminole never fluctuates by more than 0.6 m and the average

and maximum water surface elevations during both periods of survey collection were nearly identical (Table 1).

In addition to having a higher point density, the metadata available regarding survey collection, processing, and point classification for the 2018 survey is much more extensive than the metadata for the 2007 survey. After the calibration, vertical accuracy, and relative accuracy of the laser point data was confirmed, Dewberry used a variety of software suites for data processing. The laser points were imported into GeoCue and classified using a proprietary routine in TerraScan. After extracting the ground layer, a surface model was created to examine the classification of ground points, and analysts manually corrected classification errors stemming from vegetation and buildings. After completing the ground classification corrections, the dataset was processed using a water classification routine that automatically classified hydro features. The data were delivered to USGS as LAS tiles. The points available for download on NOAA Digital Coast are classified into seven classes: unclassified, ground, low point (noise), water, bridge deck, high noise, and ignored ground (near breakline).

3.2.2 DEM Differencing

Both the 2007 and 2018 DEMs were downloaded from the NOAA Digital Coast Data Access Viewer. After defining the region of interest in the data access viewer, a custom data file consisting of the DEM coverage of the specified study area was created by the program for download. Both DEMs were imported into ArcGIS Pro for analysis. The DEMs were created using identical projected and geographic coordinate systems (NAD83/ UTM zone 16N) and vertical datums (NAVD88 height (m) meters). The two DEMs were differenced using the Raster Calculator tool in ArcGIS Pro. That output raster was then clipped to an outline of the 2018 Chattahoochee River delta islands, created using the methods detailed in the following section, using the Clip Raster tool.

Once this process was complete, the minimum level of detection for the DoD was calculated using (2. The reported DEM vertical uncertainty for the 2018 dataset was 0.14 m (Dewberry, 2019). Though there was no vertical uncertainty reported for the 2007 DEM, the vertical error reported for the lidar survey was 0.15 m, and it is not uncommon for the DEM generation process to double the vertical uncertainty of a lidar survey; for example, the vertical uncertainty was 0.06 m for the 2018 lidar survey. Taking all of this into account, a vertical uncertainty of 0.35 m was used for the 2007 DEM, which is also the standard value used in the literature when DEM vertical uncertainty is unknown (Scott et al., 2021). This resulted in a minimum level of detection of 0.38 m for the DoD, so all values between -0.38 and 0.38 m were masked out of the DoD using the Extract by Attributes tool.

3.2.3 Point Cloud Differencing

Point cloud processing and analysis was completed on a Precision 7820 Tower Workstation equipped with 128 GB installed RAM and two Intel Xeon Gold 6242 processing units with clock speeds of 3.10 GHz and 3.09 GHz.

3.2.3.1 Pre-Processing with ArcGIS Pro and LAStools

Prior to downloading the lidar point clouds from NOAA Digital Coast, the tile grids for both surveys were downloaded from the bulk download page and imported into ArcGIS Pro. The Select by Location tool was used to identify the tiles for each survey that intersected the area of interest on the Chattahoochee River delta and these selected records were exported as a CSV file using the Export Table tool. In Excel, all fields but the Name field were deleted, and the Find and Replace function was used to remove the leading text from each LAZ file name so they exactly matched the file names on the NOAA bulk download page. This list of the LAZ file names covering the study region in each survey was then converted to a .txt file. Following this, all the LAZ files for the 2018 and 2007 surveys were downloaded by importing the URL List file from the NOAA bulk download page into UGet. After all the LAZ files finished downloading, a file

copy command in the Command Prompt was used to copy the study area files listed in each survey's .txt file to a new folder. The reason all the LAZ files for each survey were downloaded and then filtered to the study area is because the only way to filter the files queued for download in UGet was by manually unchecking files to remove them, which was not feasible for lidar surveys comprised of over 16,000 files.

After downloading the LAZ files, the LAStools Software Suite was downloaded and the ArcGIS toolbox was imported into ArcGIS Pro. The laszip tool was run in batch mode to convert all the LAZ files for both surveys to LAS files since ArcGIS Pro cannot directly open LAZ files. The Create LAS dataset was then used to create two LAS datasets: one using the 2007 tiles and one using the 2018 tiles. This step is required because LAS files must be compiled in a point cloud dataset (LAS Dataset, point cloud .slpk file, or I3S point cloud scene layer) in order to use ArcGIS Pro's datum and coordinate system functions in the Extract LAS tool. This tool was used to convert the geographic coordinate system of the 2007 tiles from NAD83 (NSRS2007) to NAD83 (2011) and to project both the 2007 and 2018 datasets into NAD 1983 (2011) UTM Zone 16N. Point clouds are required to have a linear unit to load properly in CloudCompare, so adding a projected coordinate system is an essential step to avoid XY coordinates in geographic units like degrees being incorrectly loaded as being in meters or feet.

In order to change the horizontal or vertical datum or projection in the Extract LAS tool, the new spatial reference information needs to be specified in the Environments tab under Output Coordinates. Performing datum shifts like NAD83 (NSRS2007) to NAD83 (2011) requires supplemental coordinate system information to be installed from My Esri. Additionally, though the input for the Extract LAS tool is required to be an LAS Dataset, the Extract LAS tool still creates one output file for each LAS file referenced by the LAS dataset. Thus, the final processing step before importing the points into CloudCompare was merging all the LAS files for the 2007 survey and for the 2018 survey using the lasmerge tool. This was done by calling the 64-bit lasmerge Windows executable in the command prompt.

3.2.3.2 Working in CloudCompare

In order to prevent CloudCompare from crashing due to the size of the 2018 point cloud, the two lidar surveys were split into upstream and downstream delta point clouds prior to being imported into CloudCompare, and all of the following steps were repeated for each section of the delta. When importing the LAS files, the default field settings were applied, and the suggested global shift/scale transformation was used for the 2007 LAS file. To ensure the point clouds were properly aligned, when the 2018 LAS file was imported, the global shift/scale setting was changed from the suggested parameters to the same as the previous input. After importing the clouds, the elevation coordinates for each survey were exported to scalar fields using the Projection function under the tools menu. Next the active scalar field for the 2018 survey was changed to Classification and the Filter by Value tool was used to export only the points with a value of 2, representing ground points per the survey metadata.

These 2018 ground points were then used to generate polygon outlines of the delta islands. The first step in this process was to isolate a single island by drawing a rough outline in the Segmentation tool and using the Segment Out function. After this, the isolated single island point cloud was selected and the Extract Envelope function in the Cross Section Tool was used to create a polyline outline of the island. This process—segmentation and envelope extraction—was repeated for all 31 islands on the Chattahoochee River delta. All polyline features were then selected and exported as a single shapefile. In areas where the delta shape was particularly skinny or complex, the island was split into two features that were later merged using the Merge Editing function in ArcGIS Pro. It is important to note that this process did introduce some error into any final elevation products clipped to this outline because the islands are wetlands and do have some small interior spaces filled with water rather than solid earth. On islands where there were large gaps, the island was also split into two features on either side of the hole that were later re-merged in ArcGIS Pro. The determination as to whether an island would be split to accommodate

a hole was made based on the size and shape of the hole. For example, on Figure 13, island A was split around the highlighted hole, but islands B and C were not. The hole in island B was deemed too small and the shape of the hole in island C was too complex to successfully obtain an envelope.

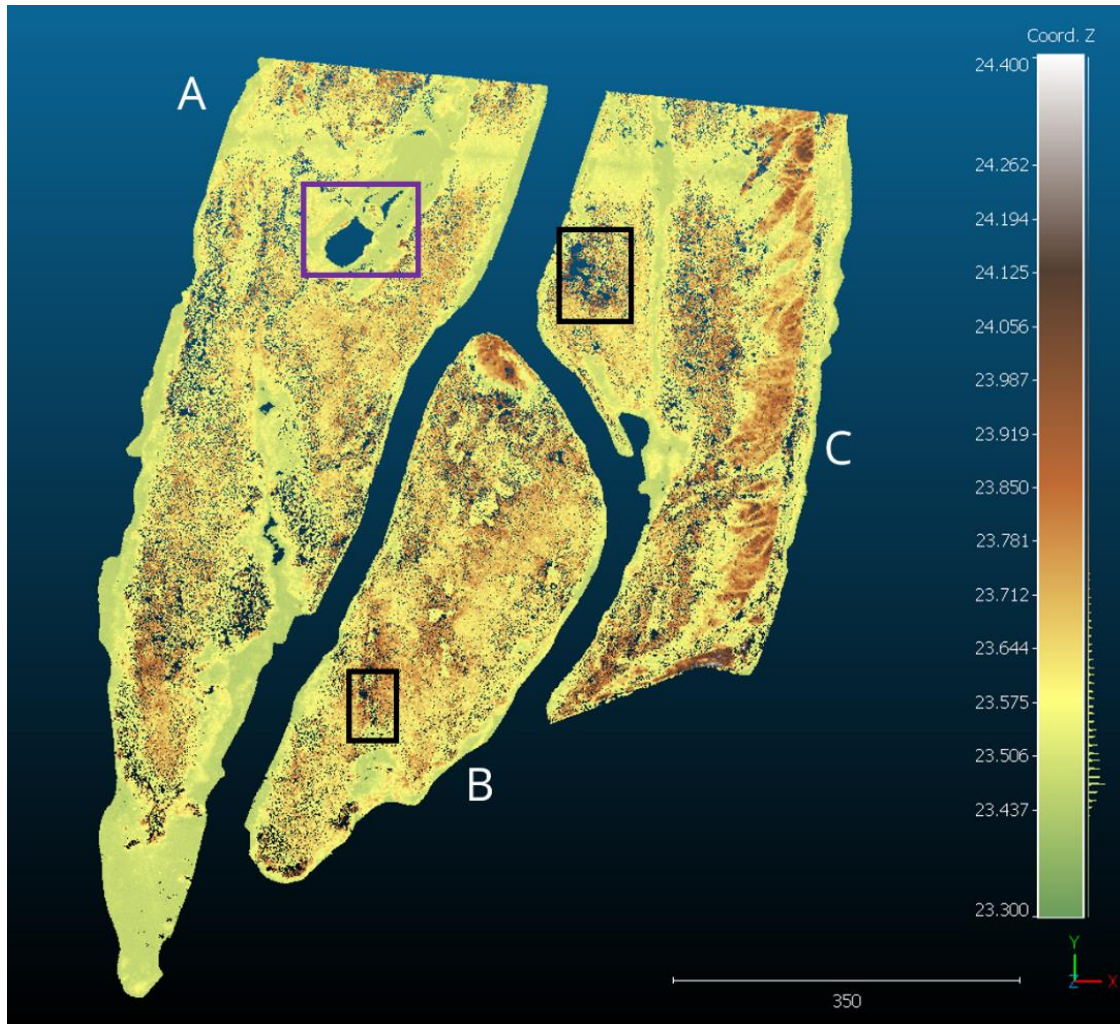


Figure 13. Sample islands from the downstream portion of the 2018 lidar ground point cloud. Holes with a black box around them were not split and the hole with a purple box around it was split. The units for the scale bar are meters and the color bar represents elevation values in meters.

Once the final outline of the delta islands was exported from CloudCompare, it was imported into ArcGIS Pro so the split islands could be re-merged, and then that final outline of the islands was re-imported into CloudCompare. Again, when re-importing the shapefile of the island outlines, it was important that the shapefile had a projection assigned to it and that the

global shift/scale was the same as the previous input. After the island outline was re-imported, the active scalar field for the 2007 survey was changed to Classification and the Filter by Value tool was used to export only the points with a value of 2, representing ground points per the survey metadata. Then the 2007 ground point cloud was clipped to the outline of the 2018 islands using the Existing Polyline function in the Segmentation tool. The 2018 ground point cloud was manually clipped to just the islands by drawing a polygon around them in the Segmentation tool.

Furthermore, the 2007 ground points included thousands of water surface returns and these points were included in the clipped point cloud used for differencing (Figure 14). The reason for this is that the M3C2 algorithm can only perform a difference in areas where there are points present in both clouds; in other words, elevation changes in areas of new growth on the delta islands could only be tracked if there was a point present in that area in the 2007 survey. Thus, a decision was made to use water surface returns from the 2007 survey, where they were present, to facilitate this analysis. Though lidar returns from water surfaces are not fully reliable due to absorption in the near-infrared wavelength, the water surface elevations at the edges of the delta islands varied from 22.8–23.4 m, which was deemed close enough to the average water surface elevation during the period of survey collection (Table 1).

The final step in CloudCompare was implementing the M3C2 point cloud comparison algorithm. After selecting the clipped 2007 and 2018 ground point clouds and opening the plugin, the following parameters were specified: the entire 2007 cloud was used as core points, the normal calculation mode was set to vertical, and the “Guess params” function was used to set the normal and projection scale values, as suggested in Lague et al. (2013). After running the tool, the output point cloud was exported as a .txt file with a comma separator. CloudCompare does allow the option to export point clouds as a shapefile; however, this does not preserve scalar fields like M3C2 distance.

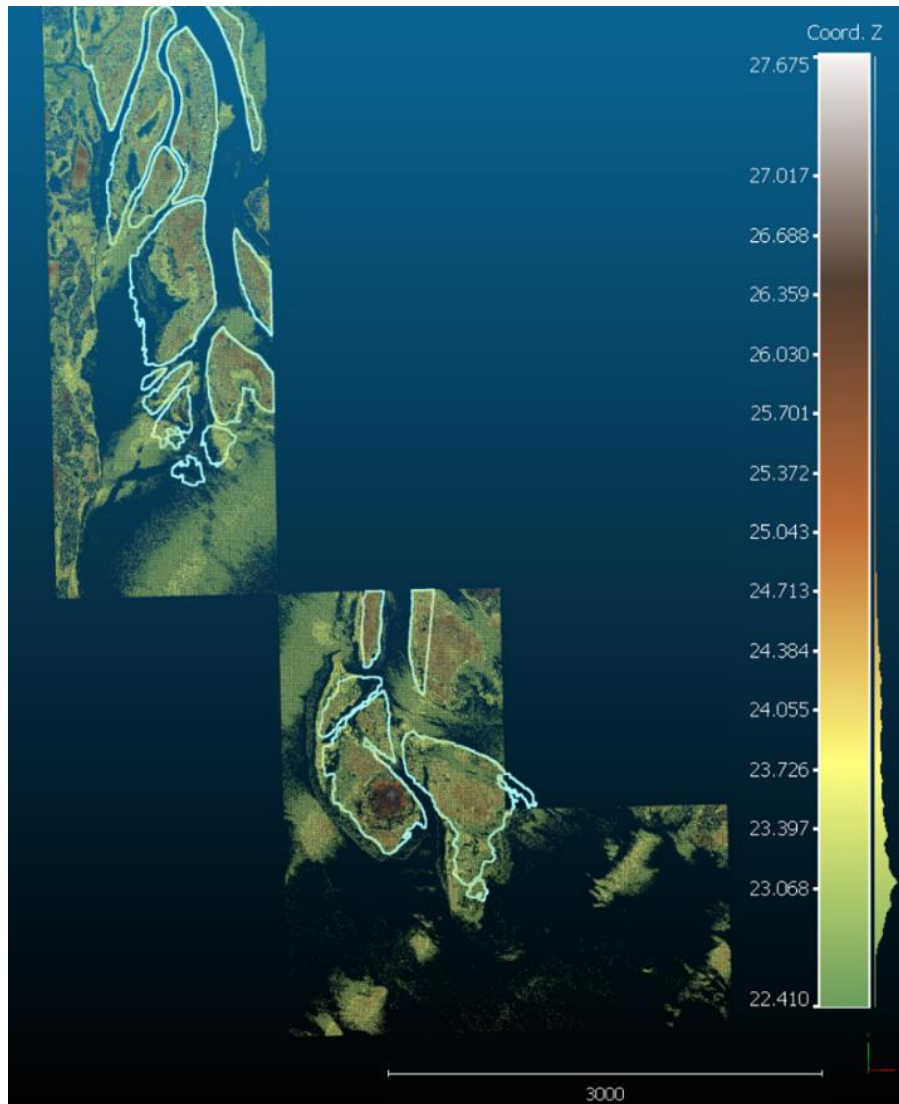


Figure 14. Downstream portion of the 2007 lidar ground point cloud with the delta island outlines overlain in light blue. The units for the scale bar are meters and the color bar represents elevation values in meters.

3.2.3.3 Filtering Vegetation and Generating Elevation Products

The final .txt files exported from CloudCompare for the upstream and downstream M3C2 differences were both imported into ArcGIS Pro using the XY Table to Point tool and then combined into a single shapefile using the Merge tool. When importing the .txt files into ArcGIS Pro, it was important to specify the same projected coordinate system that was used for the LAS files. After importing the points, the Select by Attributes tool was used to filter the point cloud so only significant change values, as determined by the M3C2 algorithm, remained. This was done

using the “significance of change” scalar field, which assigns a value of 1 to points where the distance measured by M3C2 was significantly larger at the 95 % confidence interval than a measure of the point cloud roughness and density (Lague et al., 2013). After filtering the point cloud, the Create TIN and TIN to Raster tools were used to create a 1-meter DEM of the elevation change on the delta islands, with the outline of the delta islands being used as a hard clip boundary. The optimal spatial resolution of the DEM was determined using Equation 1 and the point density of the 2007 lidar survey, which was ~ 1 point/m² (Table 1).

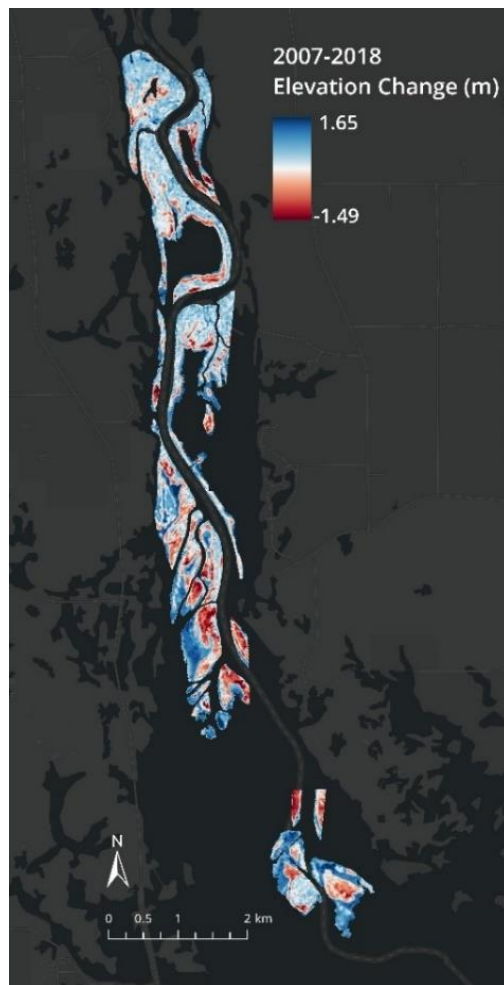


Figure 15. DEM created using the unedited M3C2 output point clouds from CloudCompare. Areas of erosion are shown in red and areas of deposition are shown in blue.

The point cloud differencing analysis could have concluded here; however, in evaluating the DEM of elevation change, it became evident that there was an abnormal erosional signal at

the center of many of the southern delta islands (Figure 15). This erosion signal is abnormal in the sense that the delta is visibly prograding in aerial imagery (Figure 1), so it would be expected that the elevation of the delta is increasing over time as sediment deposits build up rather than seeing large areas of erosion. The signal is especially abnormal in its location and magnitude: it would be unusual, for example, to have 1.2 m of erosion at the center of an island where there is 0.6 m of deposition around the outer edges. Though this erosion signal could be a result of the Chattahoochee River reworking delta sediment, it was hypothesized that these areas of erosion in the DEM were an artifact of short, dense wetland vegetation at the center of the islands being captured instead of the true ground surface in the 2007 lidar survey.

In order to test this hypothesis, the 2007–2018 elevation change point cloud was compared to maps of the 2007 vegetation height, 2009 normalized difference vegetation index (NDVI) values, and 2017 NDVI values (Figure 16). The 2007 vegetation height map was produced by differencing the entire 2007 lidar point cloud with just the 2007 ground points in CloudCompare using the M3C2 algorithm. The 2009 and 2017 NDVI maps were created using 1-meter National Agriculture Imagery Program (NAIP) imagery collected on 7/21/2009 and from 9/18/2017-11/05/2017. These were the closest high-resolution, 4-band imagery to the periods of survey collection for the 2007 and 2018 lidar surveys (Table 1). NDVI values range from -1 to 1 and quantify vegetation greenness and density by making use of the fact that healthy plants absorb most of the red light they receive as a part of photosynthesis and reflect strongly in the near-infrared portion of the spectrum (Rouse et al., 1973). In general, values between -1 and -0.1 correspond to water, -0.1 and 0.1 to barren areas, 0.1 and 0.5 to sparse vegetation, and 0.5 and 1 to dense, green vegetation. The NAIP images from each year were mosaiced using the Mosaic to New Raster tool in ArcGIS Pro and then the NDVI function was implemented to calculate the NDVI values for each year using Equation 3:

$$NDVI = \frac{NIR-Red}{NIR+Red} . \quad (3)$$

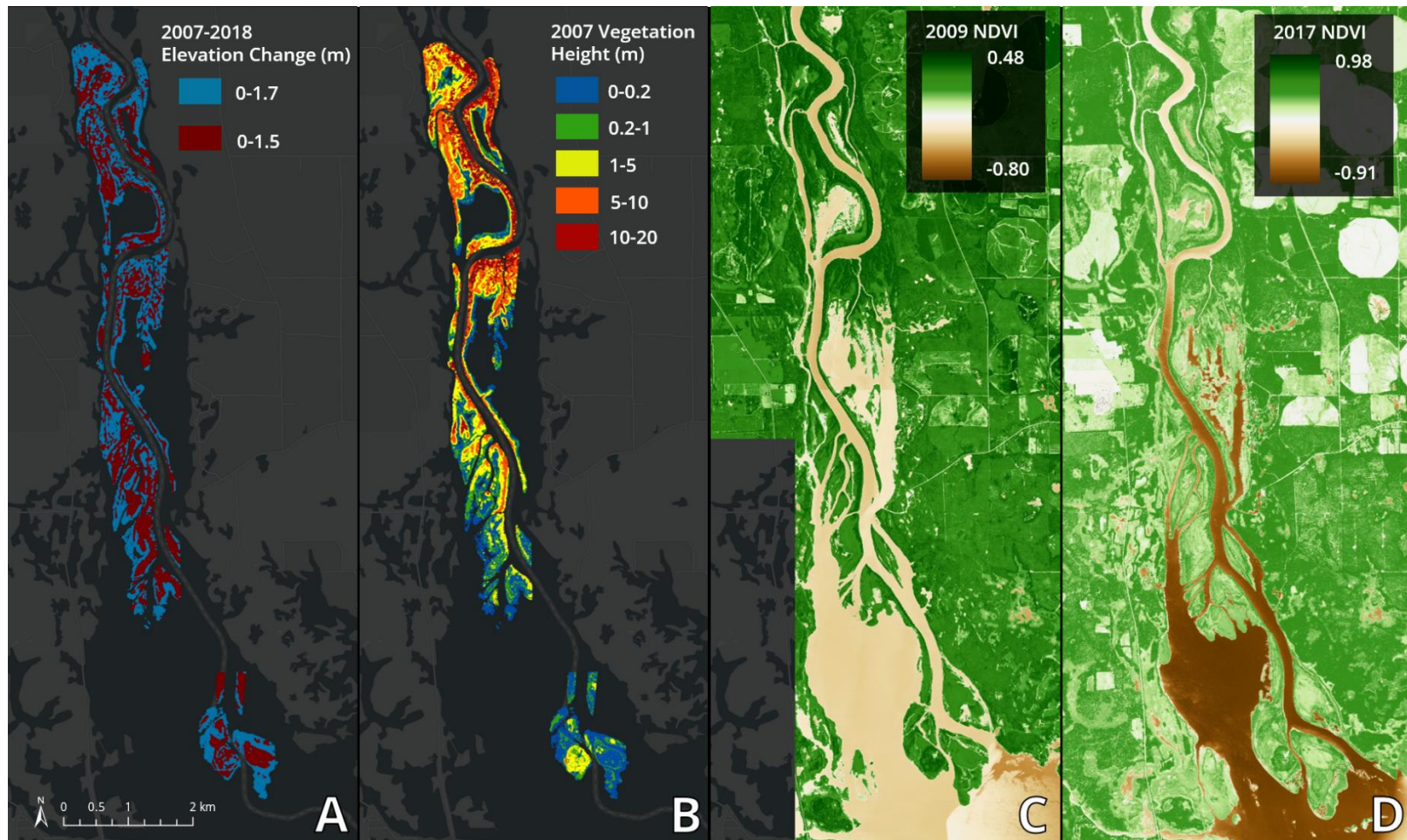


Figure 16. Process of evaluating erosional signal at the center of the delta islands. A: 2007-2018 elevation change difference point cloud filtered to remove insignificant changes. B: Vegetation height point cloud produced using the 2007 lidar data. C: Normalized difference vegetation index (NDVI) map created using a 4-band National Agriculture Imagery Program (NAIP) imagery collected on 7/21/2009. This was the closest 4-band high resolution (1-meter) imagery to the period of the 2007 lidar survey collection. D: NDVI map created using a 4-band NAIP imagery collected from 9/18/2017-11/05/2017. This was the closest 4-band high resolution imagery to the period of the 2018 lidar survey collection.

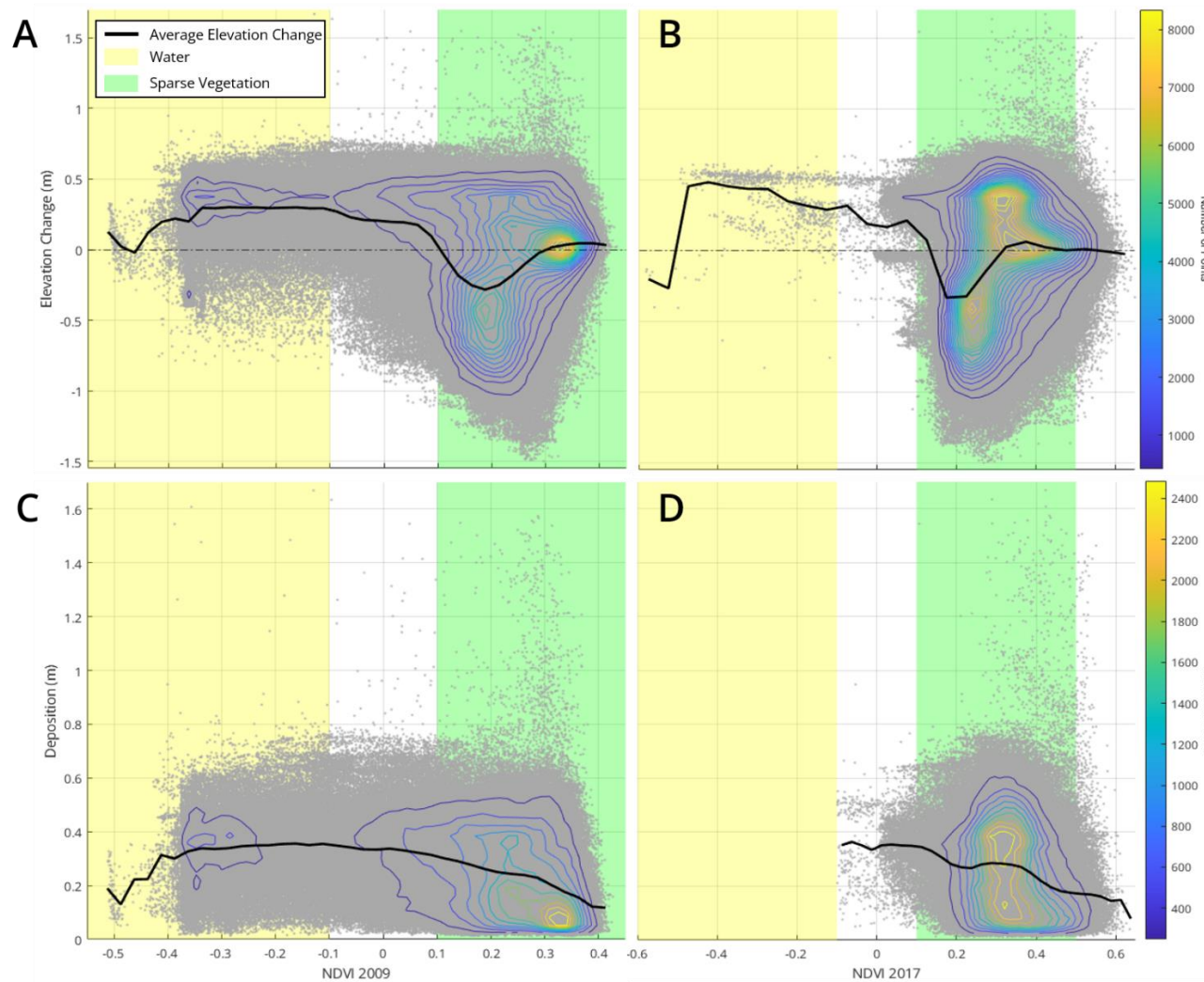


Figure 17. Plots of the 2007-2018 lidar survey elevation changes (A and B) and deposition (C and D) points against the 2009 (A and C) and 2017 (B and D) NDVI values. The approximate NDVI value range for water is shaded in yellow and the approximate value range for sparse vegetation is shaded in green. The black line on all four plots represents the average elevation change of binned values in 30 bin intervals. The contour lines reflect the density of the underlying plotted points and the color ramp represents the number of points in each contour. A: 2007-2018 elevation change plotted against 2009 NDVI values. B: 2007-2018 elevation change plotted against 2017 NDVI values. C: 2007-2018 deposition (elevation change values above 0) plotted against 2009 NDVI values. D: 2007-2018 deposition plotted against 2017 NDVI values.

Looking at Figure 16, the larger areas of erosion in panel A generally align with areas of vegetation less than 5 m in height in panel B, whereas areas of vegetation taller than 5 m in height align with areas of deposition. This could imply that taller vegetation like trees was successfully captured and filtered out of the ground surface in the 2007 lidar survey, leading to a depositional signal, whereas shorter vegetation was not captured and filtered out of the survey, leading to an erosional signal. The same trend is visible with the NDVI values in panels C and D: the darkest green areas correspond to areas of deposition, whereas the light green areas match up with areas of erosion on the islands in panel A. A decision was made to map NDVI values close the period of collection for both the 2007 and 2018 lidar surveys, rather than just the 2007 survey, to confirm that areas of shorter, reedy vegetation were present in the same spots during both years of survey collection, and it appears that this was the case.

In order to further evaluate this vegetation hypothesis, the M3C2 elevation change points were plotted against the 2009 and 2017 NDVI values in MATLAB (Figure 17). It is important to note that the 2007 vegetation height map was produced using the ground points from the 2007 survey, so, if the ground points in the 2007 survey are inaccurate because they reflect vegetation rather than bare earth, then the vegetation map is also inaccurate. Thus, the NDVI values were prioritized moving forward with the analysis. The Extract Multi Values to Points tool in ArcGIS Pro was used to assign a 2009 and 2017 NDVI value to each point in the M3C2 elevation difference point cloud. This table was then exported from ArcGIS Pro and imported into MATLAB to produce the plots shown in Figure 17. Looking at the contour lines in panels A and B of Figure 17, most of the erosional points are concentrated in areas of sparse vegetation; however, most of the deposition is concentrated in areas of vegetation as well, so resolving this issue was not as simple as ignoring the points located in areas of sparse vegetation. The exception to this is that deposition is also concentrated over areas of water in the 2009 NDVI map, as shown in panel A. This is because water surface returns were included in the 2007 ground point cloud that was used for differencing. Based on the evidence shown in panels A and B, a decision was

made to remove all erosional points from the dataset and only focus on areas of deposition. Although this did remove all the genuine erosional points from the dataset, there was no clear way to distinguish between these points and those resulting from errors capturing vegetation in the 2007 survey, so a more simplistic change detection approach was adopted.

Panels C and D in Figure 17 show only the depositional points that were used for the analysis. Additionally, the depositional points that occurred in areas of water in the 2017 NDVI map (panel B) were also removed from the final dataset. These were a result of the very small interior spaces in the delta islands that were filled with water instead of solid earth and these points were removed because they do not represent true ground points. Looking at the plots of these final depositional points against the 2009 and 2017 NDVI values shown in panels C and D, areas of deposition are more clearly concentrated in areas of water and sparse vegetation in 2009 and in areas of sparse vegetation in 2017.

The final processing steps were filtering the M3C2 elevation difference point cloud in ArcGIS Pro to remove erosional points and depositional points located over water surfaces in the 2017 NDVI map, and then producing a final DEM using this point cloud. The Create TIN and TIN to Raster tools were again used to create a 1-meter DEM of the elevation change on the delta islands, with the outline of the delta islands being used as a hard clip boundary. The average aggradation rate and volumetric change in sediment storage for the delta were calculated using this interpolated DEM surface rather than the point cloud because the histogram of the point cloud was strongly skewed to the right (Figure 18). This skew, of course, was a result of removing all the erosional points from the dataset, which chopped off the left part of the distribution.

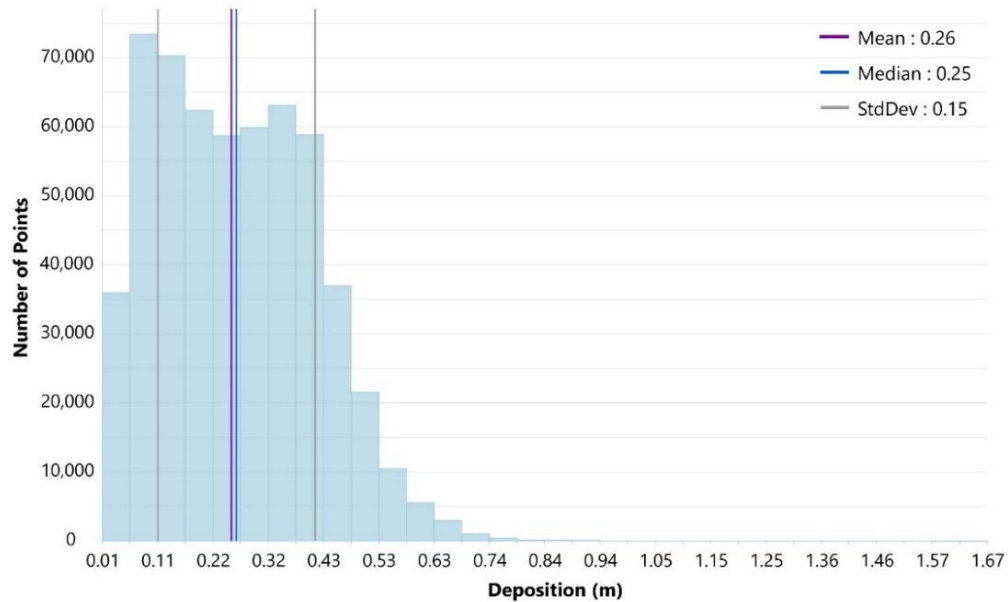


Figure 18. Histogram of the 2007-2018 depositional point cloud. The distribution is strongly skewed to the right because of the removal of all erosional points.

3.3 Results

3.3.1 DEM Differencing

Between the 2007 and 2018 lidar surveys, 9% of the subaerial land surface of the Chattahoochee River delta underwent net aggradation and 14% underwent net erosion, based on the DoD (Figure 20). The remaining 77% of the delta land surface was masked out of the DoD because the elevation change was below the minimum level of detection. The mean, median, and standard deviation for the elevation differences in the DoD were -0.20 m, -0.56 m, and 0.68 m, respectively, indicating that erosion was the dominant change on the delta land surface. However, these results need to be considered in the context of the vegetation-related errors in ground point elevations that were encountered when working with the 2007 lidar survey point cloud as well as the smaller overall magnitude of the depositional signal. Looking at the unedited DoD, 83% of all depositional pixels had values between 0 and 0.38 m whereas only 68% of the erosional pixels had values between 0 and -0.38 m, so a larger area of depositional pixels were lost when the minimum level of detection was masked out. This also underscores the earlier conclusions about

the abnormality of the erosional signal visible in both the DoD and point cloud difference: in many areas, the erosional signal at the center of a delta island is between 1-2 m whereas the depositional signal around the outer edges of the island is less than 0.5 m (Figure 20). Because of this, and for the sake of comparison with the point cloud difference, a decision was made to mask out all erosional values from the DoD, as was done prior to producing the final point cloud difference DEM (Figure 20).

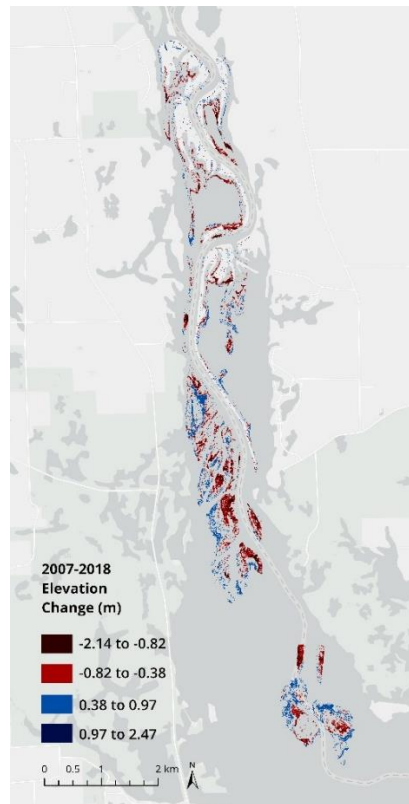


Figure 19. DoD showing the Chattahoochee River delta elevation change between 2007 and 2018. Areas of erosion are shown in red and areas of deposition are shown in blue. A minimum level of detection of 0.38 m was applied.

3.3.2 Point Cloud Differencing

The mean, median, and standard deviation of the rates of change ($\Delta z/\Delta t$) calculated using the final point cloud difference DEM were 1.46 cm/yr, 0.89 cm/yr, and 1.29 cm/yr, respectively, with correspondent mean, median, and standard deviation values for the combined error in the calculated rates of change being 0.48 cm/yr, 0.44 cm/yr, and 0.26 cm/yr, respectively. This

corresponds to an average of 0.16 ± 0.05 m of aggradation between 2007 and 2018 across the entire delta surface (Figure 20). In total, the subaerially exposed portion of the Chattahoochee River delta accumulated 1.07×10^6 m³ of sediment during the study period. Only 3.5% of the delta land surface aggraded more than 0.5 m, and the most rapid areas of aggradation (> 4.5 cm/yr) were located around the exterior edges of the delta islands whereas the interior wetlands were comparatively stable. Due to limited data availability in the 2007 lidar survey (Figure 12), 9% of the overall subaerial delta was not included in the study. Though this section of the delta is not accounted for in the above statistics, it is estimated that comparable magnitudes of deposition occurred in this area during the study period.

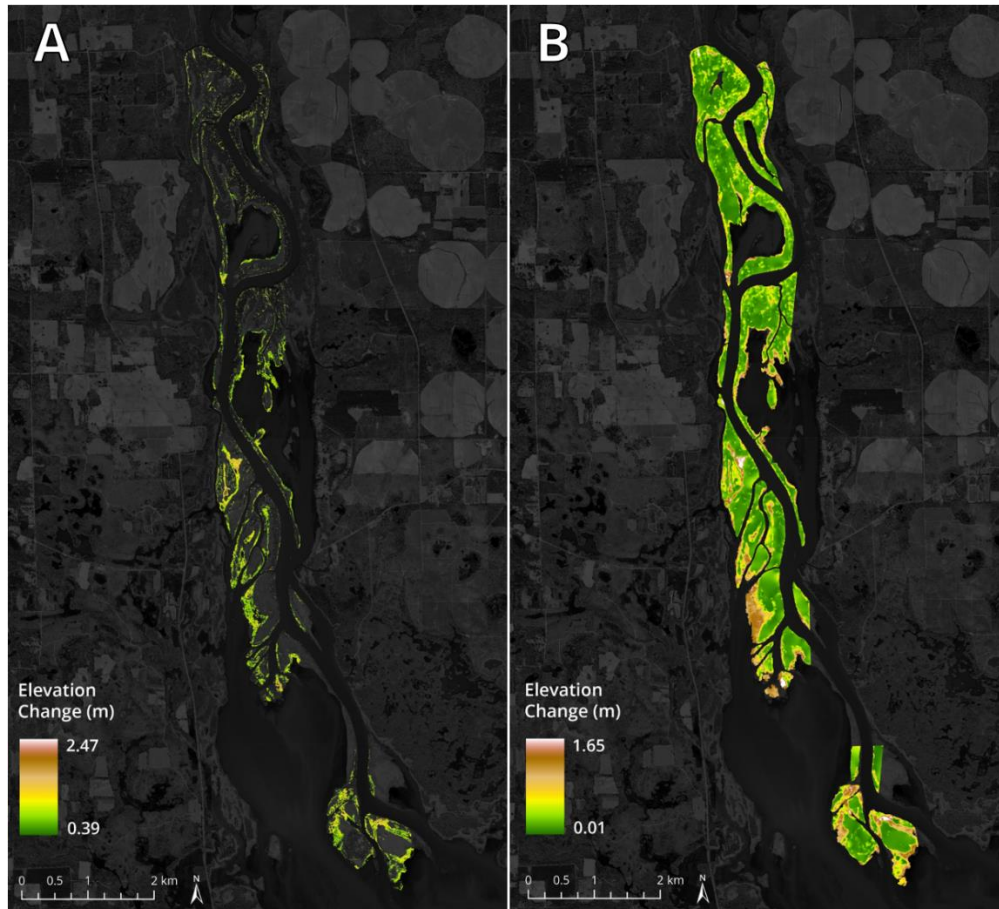


Figure 20. The final digital elevation models of delta deposition from 2007-2018 produced using (A) DEM Differencing and (B) point cloud differencing methods. A: DoD resulting from differencing the 2007 and 2018 lidar DEMs, applying a minimum level of detection of 0.38, and filtering out all erosional points. B: DEM resulting from differencing the 2007 and 2018 lidar point clouds using the M3C2 algorithm and removing all erosional points.

To further investigate the spatial variability in elevation changes, deposition was plotted against downstream distance and a linear regression model was fit to the points (Figure 21). The scatterplot and bin average line both showed a very weak positive linear relationship between deposition and downstream distance. This was confirmed with a Pearson's correlation coefficient of 0.291 for the data. Additionally, the R^2 value was 0.085, so 8.5% of the variation in sediment deposition could be explained by the downstream distance. Simple linear regression revealed a significant relationship between deposition and downstream distance ($p = 0.000$); however, this finding should be interpreted in the context of the large sample size ($n = 562,113$). It has been well-documented that a large sample size ($n > 10,000$) can result in a significant p-value even if the difference between groups is negligible, so the correlation coefficient and R^2 value are more useful indices in this scenario (Sullivan and Feinn, 2012). Looking at the bin average line, the two largest areas of deposition were located at 5.25 and 11.75 km downstream and the two smallest areas of deposition were located at 0.75 and 10.75 km downstream. It is also important to contextualize these results with the 1 km data gap between 9.75 and 10.75 km downstream. This data gap is due to the limited coverage available in the 2007 lidar survey (Figure 12) and also extends to the low point density between 10.75 and 11.25 km downstream, which could be responsible for the downward spike in the depositional signal observed in this region.

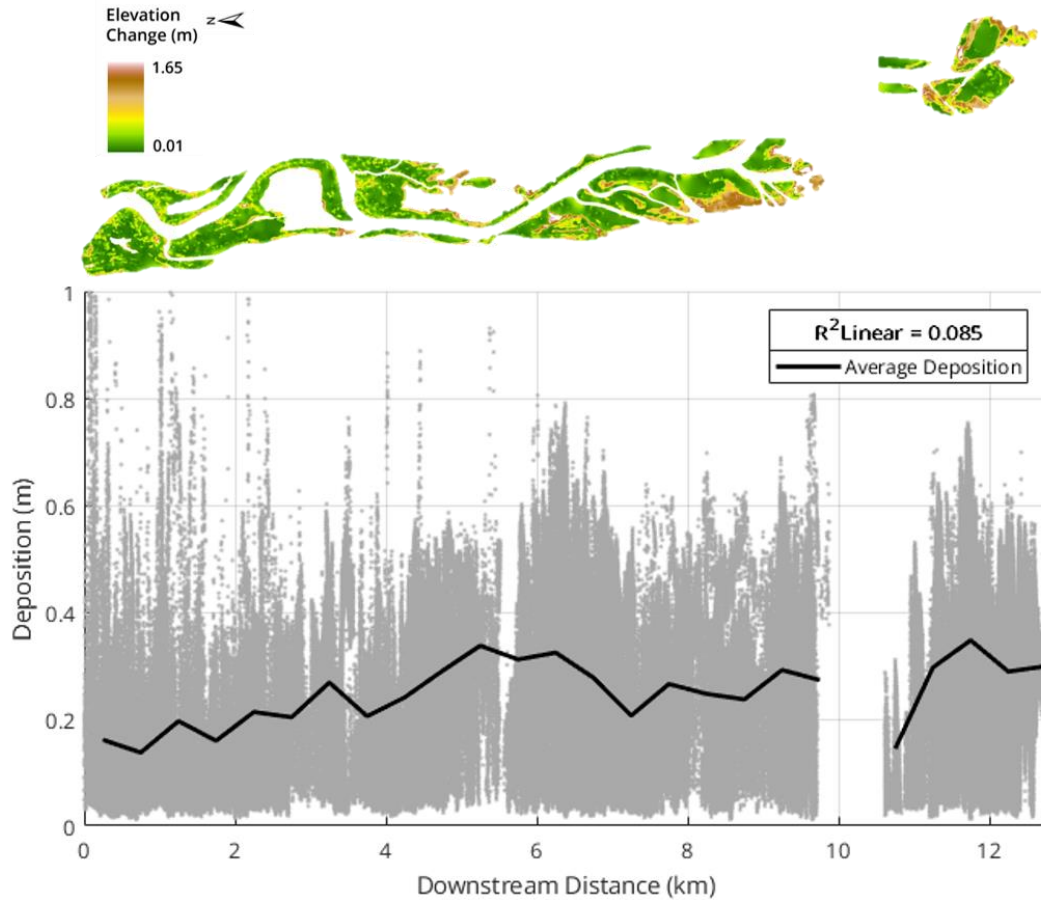


Figure 21. Plot of deposition from the M3C2 difference against downstream distance along the Chattahoochee River delta. The black line represents the average deposition of binned values in 25 bin intervals. A DEM of deposition is shown above the plot and aligned with the x-axis so 0 corresponds to the upstream-most point on the delta.

3.3.3 Methodological Comparison

Overall, the point cloud differencing method yielded both a lower uncertainty value for the geomorphic change and a lower average magnitude of sediment deposition on the delta, with a mean depositional value over three times less than that yielded by the DEM differencing method (Table 2). This also means that the minimum and maximum depositional values for the point cloud difference DEM were much lower than those produced by DEM differencing. The lower uncertainty for the point cloud differencing method was key due to the lower overall magnitude of aggradation on the delta: the average of 0.16 m of deposition produced by the point cloud differencing method falls within the bounds of the minimum level of detection mask that

was applied to the DEM difference, which is why the average depositional magnitude is much higher for the DEM difference. However, the mean and median values for the point cloud difference DEM were notably further apart than those produced by the DEM differencing: the point cloud differencing median was only 63% of the mean value whereas the DEM differencing median was 96% of the mean value. This indicates that removing all erosional points resulted in a data distribution that was more strongly skewed to the right for the point cloud difference DEM compared to the DEM differencing DEM. Both methods yielded similar standard deviations.

Table 2. Comparison of the descriptive statistics and uncertainty values for the depositional DEMs (Figure 20) produced using DEM differencing and the M3C2 algorithm (point cloud differencing).

	DoD Deposition (m)	M3C2 Deposition (m)
Minimum	0.38	0.01
Maximum	2.47	1.65
Mean	0.53	0.16
Median	0.51	0.10
Standard Deviation	0.13	0.14
Uncertainty	0.38	0.05

3.4 Discussion and Conclusions

On the Chattahoochee River delta, subaerial sedimentation occurred at a rate of 1.46 ± 0.48 cm/yr between 2007 and 2018, supporting the inference from historical aerial photos that the reservoir delta is an active depositional system (Figure 20). A similar analysis conducted on the Wax Lake Delta (WLD), a coastal delta in Louisiana, found an average net elevation change of 2.02 cm between 2009 and 2013, which indicates that the average elevation difference of 16 cm observed on the Chattahoochee River delta is quite high (Wagner et al., 2017). It is important to note that study period for this analysis was nearly three times as long as that used for the WLD and that the removal of all erosional points did significantly increase the average elevation change on the Chattahoochee River delta compared to the WLD, which included several large areas of erosion. The areas of most rapid aggradation (> 4.5 cm/yr) on the Chattahoochee delta were located around the exterior edges of the islands whereas the interior wetlands were relatively

stable (Figure 20). Furthermore, there was a very weak positive linear relationship between sediment deposition and downstream distance, with the largest zone of deposition being located 11.75 km downstream, or about 90% of the downstream extent of the subaerial delta (Figure 21).

These results also need to be considered in the context of several key limitations. The 2007 lidar survey had a low point cloud density that may have resulted in the ground surface being improperly captured as well as a data gap on the lower portion of the delta that prevented that area from being analyzed (Figure 12). Furthermore, water returns were not removed from the 2007 survey before conducting the difference to be able to account for the growth of new delta islands between surveys (Figure 14). The decision to use these water returns did introduce some additional error into the process since the 2007 water surface elevations were, on average, lower than the actual water surface, which resulted in an overestimation of the elevation change in these areas. However, water returns were not present everywhere, so much of the aggradation associated with new subaerial island development was not able to be measured, which resulted in an underestimation of aggradation in these areas. Lastly, removing all erosional points from the point cloud difference introduced an additional source of error into the dataset and likely resulted in an overestimation of the delta aggradation rate.

In terms of the best method for measuring topographic change in a reservoir delta environment, point cloud differencing yielded a much lower uncertainty value, compared with DEM differencing, and was more sensitive to the lower rates of change associated with aggradation on the Chattahoochee delta (Table 2). However, DEM differencing would be advantageous in a reservoir delta environment with a stronger magnitude of sediment deposition: in spite of the higher error associated with DEM differencing, it is simpler, faster, and more cost-effective than point cloud differencing, which can be time consuming and computationally intensive depending on the size of the point clouds (Table 1). Aside from the lower uncertainty, another benefit of working directly with the lidar point clouds was the ability to produce an outline of the delta islands using the ground points, which was an important component of this

study. Though it was not necessary in this analysis, working directly with point clouds also allows for the manual correction of any errors in the ground point classification process, which are common in wetland environments. DEM differencing and working with point clouds are not mutually exclusive: after creating an outline of the delta islands and correcting any errors in the ground filtering, DEMs could still be generated from the lidar surveys and differenced for the sake of time and simplicity. Overall, point cloud differencing is a valuable method for analyzing geomorphic change in a subaerial delta environment due to its ability to capture slower rates of aggradation and the opportunity it provides to correct ground classification errors, but DEM differencing can be a more practical choice for deltas and other depositional environments with faster rates of aggradation.

For future research directions, one possible application would be using the 2007 and 2018 lidar surveys to assess changes in elevation in the Chattahoochee floodplain. Sediment infilling in river channels upstream of dams due to the rise in base level makes the floodplain more accessible to the river during high discharge events, which leads to more frequent and extreme floodplain inundation and overbank sediment. Differencing repeat lidar surveys covering the floodplain could be useful for tracking this overbank sedimentation; however, it is uncertain whether the signal of deposition would be large enough to appear in the lidar surveys and occur rapidly enough to be traceable over 11 years. Additionally, the 2007 and 2018 lidar surveys could be used to create canopy height models (CHMs) that could then be differenced to evaluate vegetation establishment on the Chattahoochee River delta and floodplain upstream as sediment deposits build up over time and establish new wetland habitat. In fact, a CHM was already created using the 2007 lidar survey as a part of this study. In terms of working with other lidar surveys, the 2018 lidar survey could be differenced with an existing 2020 lidar survey, which was collected shortly after Hurricane Michael, to analyze the impact of short-term extreme events on sedimentation patterns on the Chattahoochee delta. Eventually, it would also be useful to investigate sedimentation on the Flint River floodplain upstream of the reservoir using lidar

surveys; however, the oldest lidar survey available for the Flint arm of the reservoir was collected in 2020, so several more years need to pass before that becomes possible.

Chapter 4: Evaluating Subaqueous Sedimentation Using Bathymetric Surveys and Cross Sections

4.1 Introduction

Though a subaerial delta is often the first visible sign of reservoir sedimentation, in most reservoirs, these coarse topset sediments represent only a small fraction of the total impounded sediment volume, with fine sediments being deposited underwater, deeper in the reservoir pool (Morris et al., 2023). While subaerial sedimentation can be tracked using lidar surveys, and even viewed from space in satellite imagery, measuring subaqueous reservoir sedimentation requires a more targeted data collection approach like conducting bathymetric surveys or coring accumulated sediments. In fact, bathymetric surveys are uniquely valuable for quantifying reservoir sedimentation trends at a spatial scale that is challenging to achieve with sediment cores alone. For Lake Seminole, two bathymetric surveys are available from 2009 and 2023 that provide continuous spatial coverage of the Flint and Chattahoochee paleochannels. In addition, the USACE set up a network of rangelines where bathymetric cross sections were surveyed at four intervals between 1957–2009. In this project, these bathymetric datasets were used to calculate both recent and historical subaqueous sedimentation rates in Lake Seminole over the past six decades and assess spatial patterns in sedimentation. Unlike the Chattahoochee arm of the reservoir, the Flint arm does not have a subaerial delta deposit; however, this does not preclude it from having a subaqueous deposit like a hyperpycnal delta, so bathymetric surveys are a particularly important tool for assessing sedimentation there. The key research questions this study aimed to answer were:

- 1) At what rates did subaqueous sediment accumulate in Lake Seminole between 1957–2023? How did these rates evolve with time?
- 2) Which rangelines or sections of the reservoir were loci of deposition? What were the spatial trends in subaqueous sedimentation?

3) Is there evidence of sedimentation or deltaic deposits in the Flint arm of the reservoir?

4.2 Methods

4.2.1 Bathymetric Surveys

4.2.1.1 Datasets

Prior to beginning this project, the most recent multibeam echosounders (MBES) survey of Lake Seminole was completed in 2009. The survey is available for download on a USACE web application (https://gis.sam.usace.army.mil/Work/_R004/) as a series of XYZ files. PDF match sheets for each section of the survey are also available to download in the web application. These sheets specify that survey points are referenced to the horizontal coordinate system NAD 83 (NSRS 2007) State Plane Georgia West and the vertical datum NGVD 29 (US ft). Additionally, the survey was referenced to elevation above mean sea level, so the Z values in the XYZ files represent elevations of the reservoir floor, not depths.

In order to assess subaqueous sedimentation following 2009, an updated 2023 MBES survey of Lake Seminole was conducted in support of this project. This survey was collected in June 2023 with a reported horizontal coordinate system of NAD 83 (2011) State Plane Georgia West and a vertical datum of NAVD 88 (US ft). Though the 2023 bathymetric survey has a much higher point density than the 2009 bathymetric survey, the overall survey area is notably lower, with coverage mostly limited to the submerged Chattahoochee and Flint paleochannels (Table 3). The survey team reported that coverage was limited due to difficulties with shallow water in parts of the reservoir.

Table 3. Summary of the metadata for the 2009 and 2023 bathymetric surveys. WSE=Water surface elevation. LS=Lake Seminole. CH=Chattahoochee River. Q=Stream discharge. FL=Flint River. AP=Apalachicola River. The average and maximum discharge values are for the period of survey collection shown in column 2 and were calculated using the streamgage closest to Lake Seminole on each river.

Dataset	Survey Dates	Survey Area (km ²)	Point Density (pts/m ²)	Horizontal Datum	Vertical Datum	LS Avg. & Max WSE (m)	CH Avg. & Max Q (m ³ /s)	FL Avg. & Max Q (m ³ /s)	AP Avg. & Max Q (m ³ /s)
2009 Bathy	2009	80	0.01	NAD 83 (NSRS 2007); State Plane GA West	NGVD29 (US ft)	23.46	426	286	810
						23.73	2525	1803	3624
2023 Bathy	6/2023	8	4	NAD83 (2011); State Plane GA West	NAVD 88 (US ft)	23.41	298	256	616
						23.53	858	518	1147

4.2.1.2 Creating the Rasters

The 2009 bathymetric survey was downloaded from the USACE web application as a series of XYZ files. These XYZ files were then converted to CSV files in Windows Notepad by using the Find and Replace function to replace all the spaces in the files with commas. All CSV files were imported into ArcGIS Pro by running the XY Table to Point tool in batch mode, making sure to specify NAD 83 (NSRS 2007) State Plane Georgia West and NGVD 29 (US ft) as the horizontal and vertical coordinate systems. The Merge tool was then used to combine all the resulting point shapefiles. This merged dataset was reprojected to NAD 1983 (2011) UTM Zone 16N using the Project tool, specifying a geographic transformation from NAD83 (NSRS2007) to NAD83 (2011). As noted in the point cloud differencing methods, performing datum shifts like these requires supplemental coordinate system information to be installed from My Esri. The Project tool was also used to transform the vertical datum from NGVD29 (US ft) to NAVD 88 (US ft) and then from NAVD 88 (US ft) to NAVD 88 (m). This final transformation from NAVD 88 (US ft) to NAVD 88 (m) does not have to be completed using the Project tool; alternatively, a

new double field can be added to the point shapefile and the Field Calculator can be used to multiply the elevation values by 0.304 to convert them to meters.

In order to account for gaps in the bathymetric survey coverage within the upstream portions of the Chattahoochee and Flint arms, 23.46 m was enforced as an elevation boundary for the shoreline of the reservoir. The reported mean water surface elevation during the collection of the 2009 survey was 77 ft or 23.46 m (Table 3). This boundary was enforced by converting the reservoir boundary polygon to a line using the Polygon to Line tool in ArcGIS Pro. For this project, the boundary polygon was provided by collaborators at USACE as a part of the dataset package for a 2020 lidar survey of the reservoir; however, in the absence of direct collaboration with USACE, reservoir outline polygons can be found in the National Hydrography Dataset (NHD) waterbodies feature layer. After converting the reservoir polygon to a line, the Generate Points Along Lines tool was used to create points along the outline of the reservoir at 1 m intervals. A new double field was then added to the resulting points shapefile and the Field Calculator was used to set the value of this field to 23.46 for all points. It is important that the name of this new field matches the name of the elevation field in the 2009 bathymetric survey points shapefile. Lastly, this reservoir outline points shapefile was merged with the 2009 bathymetric survey points shapefile so that the shoreline elevation value would be enforced as a hard boundary during the raster interpolation process.

A 10-meter raster was created using this merged point cloud and the Topo to Raster tool. Per Equation 1, this spatial resolution assumes a minimum point density of 0.01 points/m^2 , which is a conservative estimate given the variable point density in different areas of the survey. Within the Topo to Raster tool, the polygon of the reservoir outline was specified as a boundary input layer. It was also important to turn drainage enforcement off and change the primary type of input data to spot. The final step in creating the 2009 bathymetric survey raster was erasing the delta islands from the Chattahoochee arm of the reservoir. The same USACE 2020 lidar dataset that included the reservoir outline also included a polygon layer of the delta islands; however, in the

absence of this dataset, outlines of the delta islands could be created using a the most recent high resolution lidar point cloud available and the Extract Envelope function in CloudCompare (Figure 13). The polygon of the islands was converted to a raster using the Polygon to Raster tool and then the Raster Calculator was used to set any overlapping areas in the bathymetric survey raster as null values.

A similar methodology was used to create the 2023 bathymetric survey raster. The survey was delivered as a series of XYZ files by USACE, which were then converted to CSV files, imported into ArcGIS Pro, and merged into a single point shapefile. This point shapefile was reprojected to NAD 1983 (2011) UTM Zone 16N and the vertical datum was transformed from NAVD 88 (US ft) to NAVD 88 (m). Because the spatial coverage of this bathymetric survey was too small to justify interpolation across the entire reservoir surface, an outline of just the 2023 survey coverage needed to be generated. This was done by using the shp2las tool in the LAStools ArcGIS toolbox to export the survey points as an LAS file. This LAS file was then imported into CloudCompare and the Extract Envelope function was used to create an outline (see Section 3.2.3.2 Working in CloudCompare for additional details). Due to the complexity of the outline shape, the survey was split into six different features that were later merged using the Merge Editing function in ArcGIS Pro. Once this outline was created and imported into ArcGIS Pro, the Topo to Raster tool was used to create a 1-meter raster of the survey. Per Equation 1, the maximum resolution of the survey raster could be 0.5-meter; however, the resolution was increased to 1-meter to make the processing time more manageable.

4.2.1.3 Generating and Analyzing Cross Sections

The first step in pulling cross sections from the two bathymetric surveys was digitizing the locations of the USACE rangelines in ArcGIS Pro. This was done by importing and georeferencing Figure 25 from Tetra Tech (2011), creating a new line feature class for each rangeline, and then tracing the rangeline locations based on the image from the report using the

Create Features tool. A model was set up in ArcGIS Pro ModelBuilder using batch versions of the Generate Points Along Lines, Extract Multi Values to Points, and Table to Excel tools to create points at every 0.5 m on the rangelines, extract values from both the 2009 and 2023 bathymetric survey rasters, and then export those point values to a Microsoft Excel file. In the Generate Points Along Lines tools, it is important to select the “include end points” and “add accumulated distance and sequence fields” options and, in the Extract Multi Values to Points tool, it is important to select the “bilinear interpolation” option.

After opening this data in Excel, the first steps were to sort the sequence field from smallest to largest and then select the two columns for the bathymetric survey fields and use the Find and Replace function to replace all empty cells with “NaN”. This was important for ensuring that the sorting functions in Excel worked properly and that the data could be seamlessly imported into MATLAB. The next step was ensuring that the data was plotted in the correct direction. Cross section data is traditionally plotted from left to right when looking downstream; however, in ArcGIS Pro, most of the points were interpolated from left to right when facing upstream, so the direction needed to be switched. The first point in the interpolation sequence for each cross section was selected in ArcGIS Pro to visually confirm whether points were interpolated in the upstream or downstream direction. If the direction needed to be switched, the length field—an accumulated distance field generated by the Extract Multi Values to Points tool—was sorted from smallest to largest, making sure to specify that Excel continue with the current selection rather than expand it when prompted. The final steps were to duplicate the length field and reorder the fields as follows: length, 2009 bathymetric survey, length, 2023 bathymetric survey, making sure to delete all additional fields. This Excel workbook was then imported into MATLAB and a script was run to calculate a sedimentation rate between 2009 and 2023 in cm/yr and create a plot of the data that included this sedimentation rate.

4.2.2 Historical Cross Sections

4.2.2.1 Dataset

In order to monitor sedimentation in Lake Seminole, the USACE established a network of rangelines in 1954 and bathymetric cross sections were surveyed along these rangelines in 1957, 1976, 1988-89, and 2009 (Figure 22). Furthermore, Tetra Tech was contracted by USACE to analyze these data and determine the extent and degree of sedimentation in Lake Seminole (Tetra Tech, 2011). Both the final sedimentation report and Excel sheets containing the plots of the cross-section surveys at each rangeline were provided by the USACE for use in this project.

In spite of efforts by Tetra Tech to resolve errors in the data, several of the cross sections appear to have registration errors where morphological features like channels are misaligned in one year compared to all the others. For example, in Figure 23, the 1989 survey line appears misaligned on the left bank over the main Chattahoochee channel but matches well with the other years of data closer to the right bank. This is likely because that year of data was collected slightly upstream of the target line and the others were collected slightly downstream of the target line, but it is impossible to confirm the source of the offset. These misalignments do introduce error into the data, which is exacerbated by the relatively few rangelines available that sample the main reservoir body; however, a decision was made to proceed with the analysis and interpret the results in the context of the poor data quality for certain rangelines. As a whole, 1988-89 was the most frequent year for these alignment errors and they were more common on the Flint arm of the reservoir than the Chattahoochee.

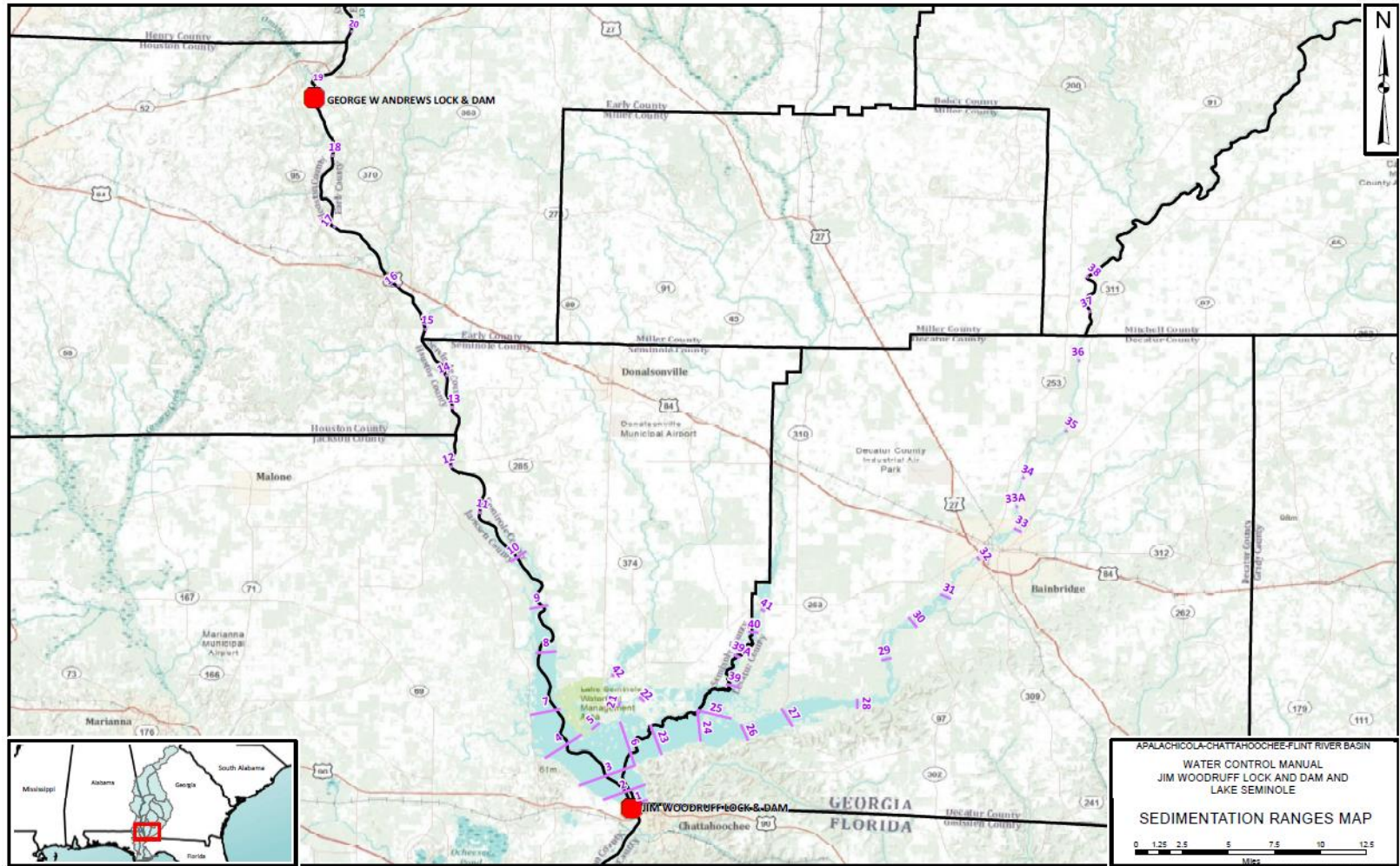


Figure 22. Map showing locations of USACE Lake Seminole sedimentation rangelines. (Tetra Tech, 2016)

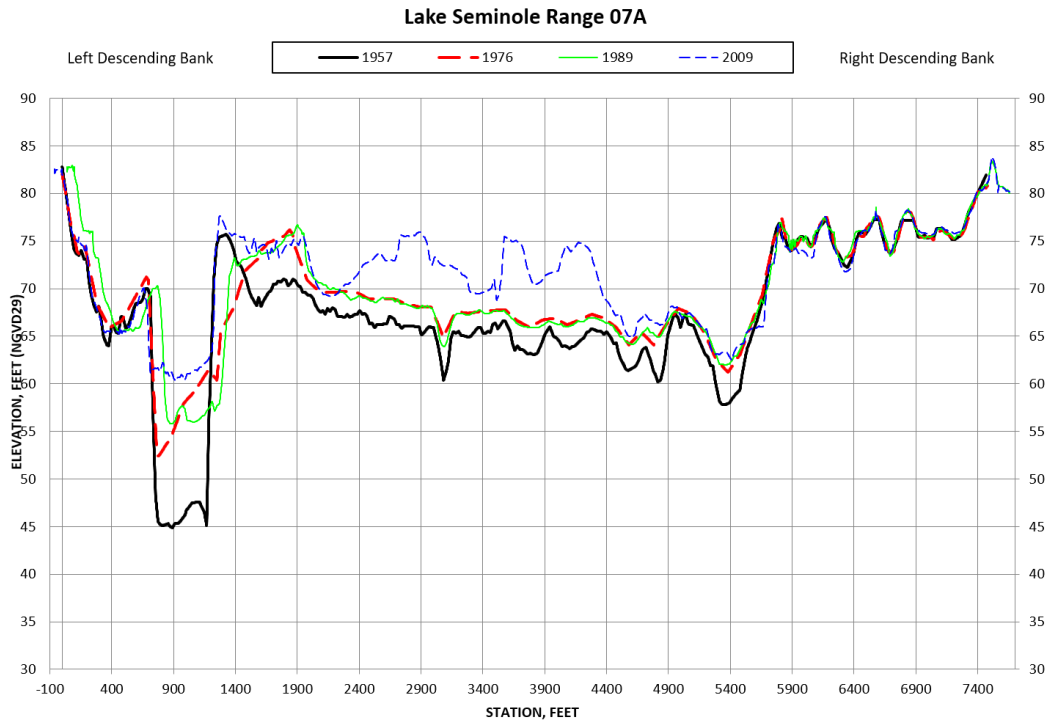


Figure 23. Cross section plot of range 07A, located in the Chattahoochee arm of Lake Seminole, produced by Tetra Tech using USACE bathymetric survey data. (Tetra Tech, 2011)

4.2.2.2 Calculating Sedimentation Rates from the Cross Sections

The cross-sectional area changes between each survey year—specifically, the area changes analyzed over the full range of lake elevations (79–44 ft NGVD)—reported in Appendix D of Tetra Tech (2011) were used as the basis for this sedimentation analysis. The cross-sectional area change values for each interval and rangeline were converted from ft² to m² and then they were divided by the top width to convert them to sedimentation in meters. The top width value for each rangeline was determined by taking the average of the top width values reported at 79 ft NGVD for the four survey years in Appendix C of Tetra Tech (2011) and converting this value from ft to m. These sedimentation values were then converted to a sedimentation rate in cm/yr for each period by dividing by the number of years in the interval and then converting from m to cm.

In order to calculate spatially integrated sedimentation rates for Lake Seminole, the reservoir was split into 14 sections based on the locations of the 21 rangelines that sampled it. The boundary polygon provided by collaborators at USACE was used to determine what

constituted the extent of the reservoir and, thus, which areas would be included in this analysis. Beginning at the Jim Woodruff Dam, a polygon for the first section was drawn in ArcGIS Pro, where rangeline 02A was traced as the uppermost boundary. The Clip tool was then used to clip the reservoir boundary polygon to this section and the Erase tool was used to remove this section from the reservoir extent. For the second section polygon, rangeline 03A was traced as the uppermost boundary. The output of the Erase tool from the previous step was clipped using the second section polygon and the second section polygon was also erased from this output. These steps continued until Lake Seminole had been split up into 14 sections. This process is illustrated in Figure 24 and ensured that the reservoir sections were exactly aligned with one another at the edges defined by rangelines.

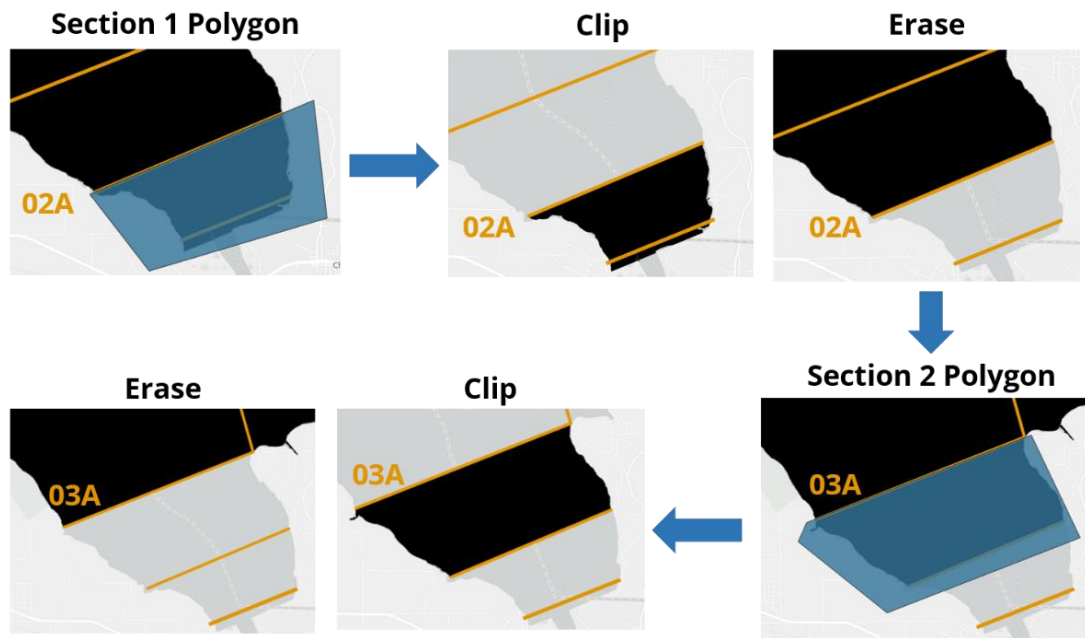


Figure 24. Process of splitting Lake Seminole into 14 sections in ArcGIS Pro based on the location of the USACE rangelines.

After all 14 sections had been delineated, the Add Field tool was run in batch mode to add a short integer field called “Section” to each of the 14 reservoir section layers, and then each section’s number was manually typed into that field. The 14 section layers were then combined using the Merge tool. The Calculate Geometry Attributes tool was used to calculate the area of

each section in m² and these numbers were copied over to the Excel sheet where the sedimentation calculation based on Tetra Tech (2011) had been performed. In that spreadsheet, it was also noted which rangelines each section sampled. A section was considered to sample a rangeline if that rangeline was included in the area of the section or if the rangeline defined one of its edges. For example, section 1 sampled rangelines 01A and 02A and section 2 sampled rangelines 02A and 03A (Figure 24). The sedimentation in meters for each reservoir section was determined for each interval by taking the average of the sedimentation values for the rangelines that section sampled. This sedimentation was multiplied by the area of each section to calculate volumetric sedimentation in m³. The sedimentation in meters was also converted to a sedimentation rate in cm/yr before exporting these values and the volumetric sedimentation as a CSV file and importing it into ArcGIS Pro. The Add Join function was used to join this table to the merged reservoir sections layer using the Section field so patterns in sedimentation could be visualized.

In order to calculate the reservoir-wide sedimentation volume for each period, the volumes for all 14 sections were added together. These reservoir-wide sedimentation volumes were converted to a sedimentation rate in cm/yr for each time period by dividing by the area of the entire reservoir, then dividing by the number of years in the period, and then converting from m to cm. In addition to reservoir-wide sedimentation rates, sedimentation rates were also calculated for the Chattahoochee arm and the Flint arm using the four reservoir sections that sampled the Chattahoochee arm and the five reservoir sections that sampled the Flint arm.

4.2.2.3 Comparison with the Bathymetric Surveys

For rangelines 02A and 03A, it was determined that the coverage of the 2023 bathymetric survey was substantial enough to warrant comparison with the historical cross section data: for all other rangelines, the 2023 bathymetric survey only covered the Chattahoochee and Flint paleochannels and, even so, channel coverage was spotty in the Chattahoochee arm. In order to

qualitatively assess the accuracy of the bathymetric survey creation and cross section generation process, the 2009 bathymetric survey cross sections were also included in this analysis to see if they aligned with those plotted by Tetra Tech. In order to facilitate this comparison, new bathymetric survey rasters needed to be created with a vertical datum of NGVD29 instead of NAVD88.

Once the new 2009 and 2023 bathymetric survey rasters were created, new cross sections were pulled from them using the same process that was used for the NAVD88 rasters. The length—or station—and elevation fields were then copied over to the Tetra Tech Excel sheets for each rangeline. The Tetra Tech station and elevation values were also converted from feet to meters to match the bathymetric survey cross sections. Because the rangelines used to pull cross sections off the bathymetric surveys were digitized based on the maps provided in Tetra Tech (2011) and not based on precise GPS coordinates, a transformation also needed to be applied to the bathymetric survey station values to ensure they aligned properly with the USACE data. The offset was visually determined based on the location of the Flint and Chattahoochee paleochannels: an offset of 61 m was applied to the bathymetric survey cross sections along rangeline 02A and an offset of 20 m was applied to rangeline 03A. After plotting the data, these Excel workbooks were then imported into MATLAB and a script was run to calculate a sedimentation rate over the interval between 1957 and 2023 in cm/yr.

4.3 Results

4.3.1 Bathymetric Survey Rasters and Cross-Sectional Sedimentation Rates

The most notable features in the 2009 bathymetric survey are the paleo channels and floodplains for the Chattahoochee and Flint Rivers (Figure 25). The Flint arm of the reservoir is generally lower in elevation than the Chattahoochee arm, which could imply that the Chattahoochee arm has shoaled due to sedimentation (Figure 25). However, the USACE cross sections that sample both the Chattahoochee and Flint paleo channels show that the submerged

Flint River floodplain is about 1.5–3 m lower in elevation than the submerged Chattahoochee floodplain, so this difference was present prior to dam construction and reservoir impoundment. Additionally, there is a narrow area of relatively higher elevation that borders both sides of the submerged Chattahoochee channel downstream of the delta islands. These deposits are likely a remnant of the natural levees of the Chattahoochee River.

Of the 12 USACE rangelines that sample the Chattahoochee channel, Flint channel, or their confluence, six underwent sediment erosion between 2009–2013 and six underwent deposition, based on cross sections pulled from the bathymetric surveys (Figure 26). All four rangelines that sampled the Chattahoochee channel (04A, 07A, 08A, and 09A) underwent erosion, with the highest erosional rates (< -2 cm/yr) located farther upstream of the dam at cross sections 08A and 09A. On the other hand, all but one rangeline (027A) that sampled the Flint channel showed sediment deposition. Sedimentation rates on the Flint were the highest (1–2 cm/yr) closest to the dam at cross sections 06A and 023A and gradually decreased to ~ 1 cm/yr further upstream from the dam at cross sections 024A and 026A until an erosional signal emerged at the upstream-most rangeline (027A). This pattern is similar to the one observed on the Chattahoochee: sediment erosion decreases downstream. As for the three rangelines that sampled the confluence of the two rivers (01A, 02A, and 03A), the rangeline closest to the dam (01A) experienced erosion—albeit at the lowest rate of all the cross sections (-0.47 cm/yr)—and the other two (02A and 03A) experienced about 1 cm/yr of sediment deposition.

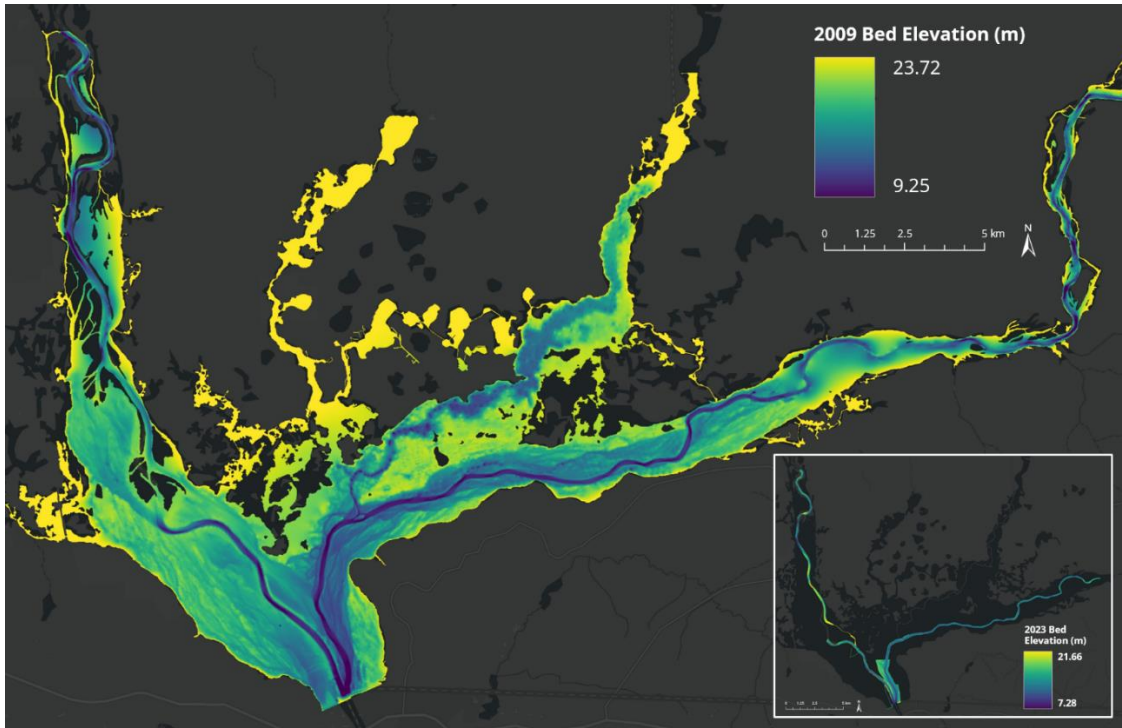


Figure 25. Map of the 2009 bathymetric survey of Lake Seminole. Inset: Map of the 2023 bathymetric survey of Lake Seminole. Coverage was limited to the Chattahoochee and Flint River channels due to difficulties with shallow water areas reported by the survey collection team.

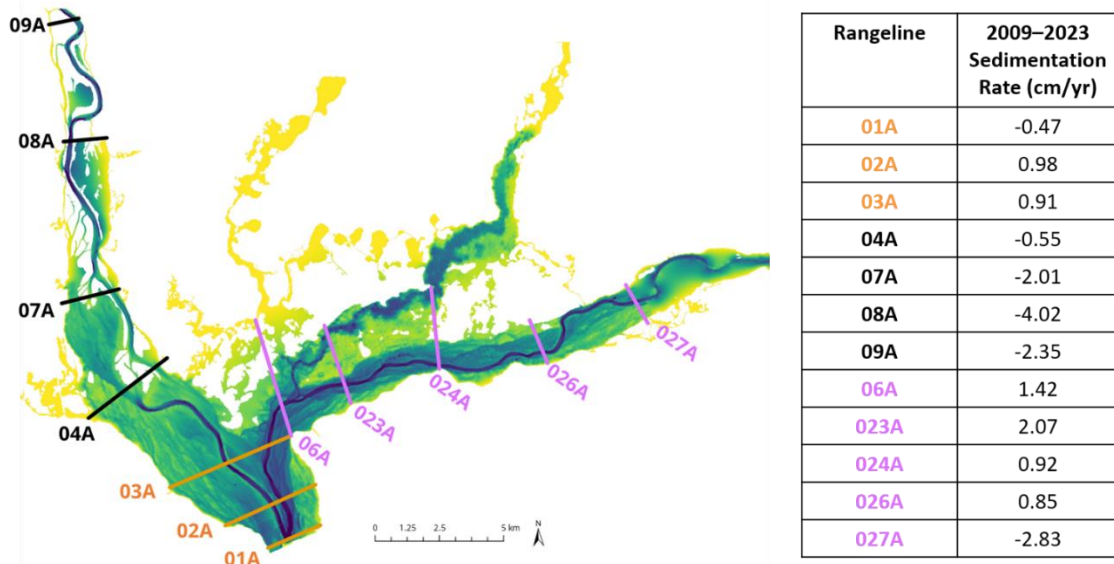


Figure 26. 2009–2023 sedimentation rates for each USACE rangeline that sampled the Chattahoochee channel, Flint channel, or their confluence. Rates were calculated using cross sections pulled from the 2009 and 2023 bathymetric surveys. Rangelines that sampled upper Spring Creek or the ponds north of the main reservoir pool were not included in this analysis due to lack of coverage in the 2023 bathymetric survey.

4.3.2 Historical Cross Section Sedimentation Rates

Based on the USACE bathymetric cross sections, sedimentation rates in Lake Seminole were highest in the two decades immediately following reservoir impoundment in 1954, with three rangelines (04A, 07A, and 09A) showing sedimentation rates greater than 2.5 cm/yr (Table 4). All three of those rangelines were located on the Chattahoochee River delta, which was a locus of deposition across all five decades of survey coverage. On the other hand, the highest erosion rates were consistently found on the Flint arm of the reservoir, particularly at rangeline 029A, which averaged -1.06 cm/yr between 1957–2009. Across all rangelines, sedimentation rates generally remained high from 1976–1989 before transitioning to a more dominant erosion signal from 1989–2009. As for the two rangelines that had significant enough bathymetric survey coverage to justify calculating a sedimentation rate from 1957–2023, sediment accumulated at a rate of 0.30 cm/yr at rangeline 02A and 0.40 cm/yr at rangeline 03A (Appendix B).

Similar conclusions can be drawn from the spatially-integrated reservoir sedimentation analysis: the highest sedimentation rate occurred from 1957–1976, followed by slightly decreased deposition from 1976–1989, and then erosion from 1989–2009 (Table 5). Between 1957–2009, Lake Seminole averaged 0.47 cm/yr of subaqueous sedimentation, which is equivalent to $3.03 \times 10^7 \text{ m}^3$ of sediment deposition. Within the Chattahoochee arm, sediment accumulated at a rate of 2.79 cm/yr between 1957–1976, 0.68 cm/yr between 1976–2009, and 1.28 cm/yr between 1957–2009, with sedimentation rates decreasing by over half between the first and second survey intervals (Table 5). In the Flint arm, the cross-sectional transect recorded erosion at a rate of -0.21 cm/yr between 1957–1976, accumulation at a rate of 0.08 cm/yr between 1976–2009, and again erosion at a rate of -0.03 cm/yr between 1957–2009. Thus, the erosional signal observed in the Flint over the entire 52-year survey period was two orders of magnitude lower than the depositional signal observed in the Chattahoochee during that same time.

Table 4. Historical sedimentation rates at the USACE rangelines that sample Lake Seminole. Rates were calculated using the cross section data provided in Tetra Tech (2011). For maps of the rangeline locations, see Figure 22 and Figure 26. Rangelines 02A and 03A are the only ones that have data from 1957–2023 because these were the only areas where the 2023 bathymetric survey was substantial enough to warrant comparison with the historical cross section data. CONFL=Confluence of Chattahoochee and Flint. CHAT=Chattahoochee River. SPRING=Spring Creek. FLINT=Flint River.

SEDIMENTATION RATE (CM/YR)						
RIVERS SAMPLED	RANGE LINE	1957–1976	1976–1989	1989–2009	1957–2009	1957–2023
CONFL	01A	1.15	3.19	-2.32	0.53	
CONFL	02A	1.90	1.52	-2.85	-0.03	0.30
CONFL	03A	1.59	1.22	-0.96	0.84	0.40
CHAT	04A	3.82	0.77	1.24	3.36	
SPRING	05A	0.19	1.41	-1.54	-0.27	
FLINT	06A	0.93	0.96	-0.53	0.61	
CHAT	07A	3.02	0.49	2.82	3.76	
CHAT	08A	1.67	1.68	-0.26	1.51	
CHAT	09A	2.76	1.87	-1.12	1.70	
SPRING	21A	-0.56	0.28	-0.25	-0.37	
SPRING	22A	0.00	-0.08	0.42	0.23	
FLINT	23A	0.18	-0.79	-0.55	-0.56	
FLINT	24A	-0.63	1.71	0.35	0.54	
SPRING	25A	-0.41	0.88	-0.24	-0.04	
FLINT	26A	-0.47	1.66	-0.40	0.15	
FLINT	27A	-0.66	-0.68	0.38	-0.43	
FLINT	28A	-1.20	1.03	-0.39	-0.54	
FLINT	29A	-0.41	-0.54	-0.95	-1.06	
SPRING	39AA	0.62	-1.15	-0.38	-0.34	
SPRING	39A	0.43	-1.36	0.27	-0.12	
SPRING	40A	0.02	0.02	-0.87	-0.52	

Table 5. Spatially integrated sedimentation rates calculated for the entirety of Lake Seminole and the Chattahoochee and Flint arms.

	Sedimentation Rate (cm/yr)				
	1957–1976	1976–1989	1989–2009	1976–2009	1957–2009
Lake Seminole	0.81	0.71	-0.13	0.12	0.47
Chattahoochee	2.79	1.04	1.17	0.68	1.28
Flint	-0.21	0.38	-0.12	0.08	-0.03

Looking at the spatial trends in the sedimentation rates from 1957–2009, the strongest depositional signal is located in the center of the Chattahoochee arm and the strongest erosional signal is located in the upstream portion of the Flint arm (Figure 27). In the Chattahoochee arm,

subaqueous deposition is concentrated beneath the subaerial delta, with sedimentation rates greater than 1.5 cm/yr, and then decreases downstream toward the confluence with the Flint River. In the Flint arm, the highest erosion rates (< -0.5 cm/yr) are located in the upstream portion of the arm, which then decrease to -0.2 cm/yr downstream before transitioning to a small depositional signal within the largest and most lake-like portion of the reservoir. Another erosional section does appear downstream on the Flint arm; however, the rate of erosion in that section is less than -0.05 cm/yr. In the three downstream sections that contain the contributions from both the Chattahoochee and Flint, sedimentation rates also decrease with distance downstream, likely as the sediment contribution from the Chattahoochee wanes.

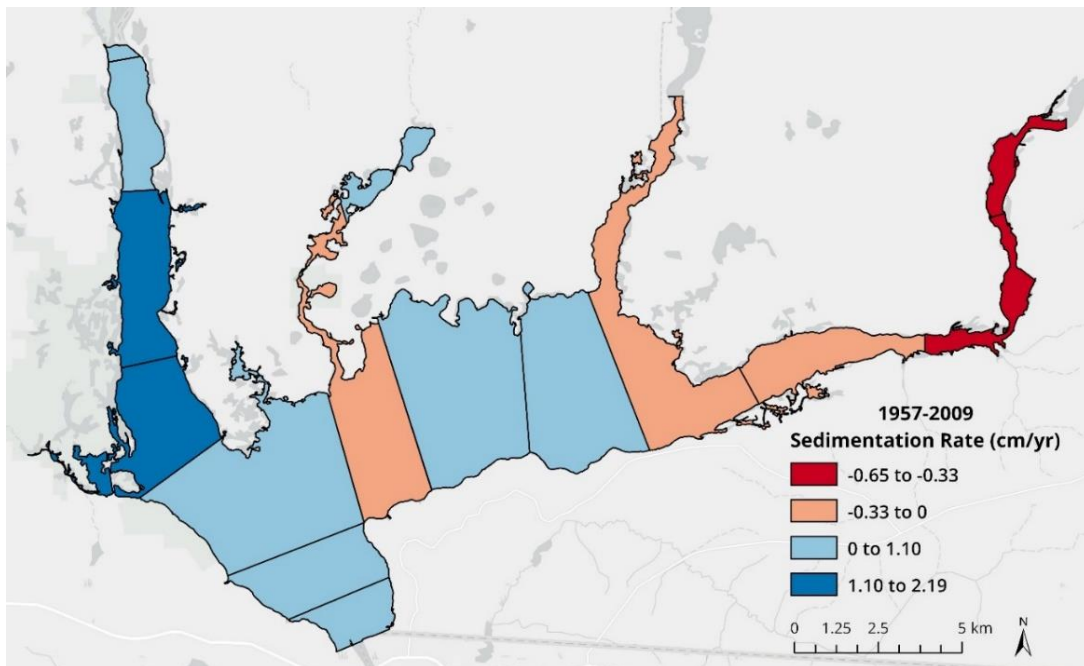


Figure 27. Map of the 14 reservoir sections used to calculate the sedimentation rates listed in Table 5. Sections are colored based on the sedimentation rate from 1957–2009.

4.4 Discussion and Conclusions

Of the cross sections that were pulled from the bathymetric surveys, all four rangelines that sampled the Chattahoochee channel underwent erosion between 2009–2023, and all but the upstream-most rangeline that sampled the Flint channel had sediment deposition (Figure 26). For

the Chattahoochee, these trends need to be considered in the context of the limited spatial coverage of the Chattahoochee channel in the 2023 bathymetric survey; the erosion signal could be a result of the Chattahoochee behaving like a sand-bedded river and eroding bars and reworking sediment since there was aggradation on the subaerial delta during this same time and visible progradation in satellite imagery (Figure 25). In fact, the subaqueous sedimentation rate calculated for the Chattahoochee between 1957–2009 (1.28 cm/yr) closely matches the subaerial aggradation rate calculated for the delta between 2007–2018 (1.46 cm/yr), so the dominant sedimentation mode in this arm is likely still deposition in spite of the erosion observed between 2009–2023 in the bathymetric surveys. The erosion signal could also be a result the main depositional center of the delta prograding beyond the coverage of the USACE rangelines

In the Flint arm, the pattern of erosion upstream and deposition downstream in the cross sections pulled from the bathymetric surveys matches the pattern observed in the map of spatially-integrated sedimentation rates in the 14 reservoir sections (Figure 26; Figure 27). The emergence of this depositional signal downstream on the Flint could be engendered by the transition to a more lacustrine environment in the reservoir pool or it could just be the Flint behaving as a river and eroding sediment upstream and depositing it downstream. Though the same trend is visible in both the spatially-integrated sedimentation analysis and the cross sections pulled from the bathymetric surveys, the magnitude of this downstream deposition varies quite a bit between the methods: based on the spatially-integrated analysis, the average sedimentation rate downstream on the Flint arm was around 0.1 cm/yr between 1957–2009, but, based on the updated bathymetric surveys, the average sedimentation rate downstream was about 1.5 cm/yr between 2009–2023 (Figure 27; Figure 26).

It is important to note that the reason for this difference in magnitude is likely that the rate for 2009–2023 only included sedimentation in the former Flint channel and the rate for 1957–2009 was sedimentation averaged across the entire width of the rangelines and then interpolated over the area of the Flint reservoir sections. Looking solely at the former river

channels, rangeline 02A shows a similar magnitude of deposition in both the Flint and Chattahoochee channels between 1957–1976 and 1976–2009, and rangeline 03A shows more deposition in the Flint channel (~1.8 m) between 1957–1976 compared to the Chattahoochee channel (~0.3 m) and then similar magnitudes of deposition in both channels between 1976–2009 (Appendix B). Rangeline 06A, which samples the Flint just upstream of its confluence with the Chattahoochee, also shows consistent deposition in the Flint channel between 1957–1976 (~0.3 m) and 1976–2009 (~0.5 m), as do the next two rangelines upstream (023A and 024A), albeit at a lower magnitude (< 0.1 m). Moving further upstream from the dam, rangeline 026A shows erosion in the Flint channel between 1957–1976 and then slight deposition between 1976–2009 whereas rangelines 027A, 028A, 029A all show consistent erosion during both survey periods. Thus, there is evidence of continued sediment deposition in the Flint arm, especially focused within the former river channel, and the magnitude of this signal decreases as distance from the dam increases. Based on the bathymetric data presented here, there is no evidence of the formation of progradational hyperpycnal delta in the Flint arm, but this does not preclude the development of such deposits in the Flint in the future, especially if sediment deposition continues to increase.

In terms of the potential for different types of deltaic deposits in the Chattahoochee arm, if there was sediment deposition on the submerged natural levees visible in the Chattahoochee arm, this could be indicative of hyperpycnal inflow due to density currents pushing sediment away from the delta face and eventually depositing it farther downstream, closer to the dam (Figure 25). Unfortunately, the bathymetric coverage in 2023 was not extensive enough to test this hypothesis as a part of this project (Figure 25). Of the two USACE rangelines that sample the levees in the Chattahoochee arm—02A and 03A—both indicate that about 0.5 m of deposition occurred on the levees between 1976 and 1988; however, there were notable alignment issues with the cross sections surveyed in 1988–89, particularly for rangeline 02A, so this increase in

elevation between survey periods may reflect data errors rather than actual deposition (Appendix B).

The main limiting factor for this project was the notable number of registration errors in the cross sections, particularly associated with the 1988–89 surveys (Figure 23). This meant that sedimentation was likely overestimated from 1976–1989 and then underestimated from 1989–2009 when the proper alignment of the 2009 surveys appeared as erosion relative to the misalignments in 1989. Moreover, the registration errors in the 1989 survey were more frequent in the Flint rangelines than the Chattahoochee ones, which could explain the emergence of the depositional signal in the Flint from 1976–1988 in the spatially integration sedimentation analysis (Table 5). Fortunately, this is not a major concern for the sedimentation rates calculated from 1957–1976, 1976–2009, and 1957–2009, just the two intermediate intervals that draw on that data from the 1980s.

Additionally, the relatively small number of cross sections that sampled Lake Seminole was a limitation in performing the spatially-integrated reservoir sedimentation analysis: for most sections, data from only two USACE rangelines was interpolated to calculate a sedimentation rate for an area that was $\sim 9 \text{ km}^2$ in size, so having a larger number of cross sections to sample would have been beneficial. Furthermore, one issue that arose when working with the USACE cross-section data was that the exact coordinates of the rangelines were not disclosed in any of the provided data, so these lines were georeferenced using maps from the report. Though this was a good way of approximating the location of the rangelines, when comparing cross sections pulled from the 2023 bathymetric survey raster to the USACE data, it became clear there was an offset in the station of the 2023 data that needed to be manually corrected for. This was not a principal limitation, however, because only two rangelines had enough coverage in the 2023 survey to warrant this comparison.

For future research paths, it would be ideal if another bathymetric survey of Lake Seminole could be conducted with spatial coverage extending beyond just the Chattahoochee and

Flint paleochannels. An updated survey with an extent that more closely matches the 2009 survey would allow the two to be differenced using the same methods employed to track subaerial sedimentation using lidar surveys in the previous section. This difference could provide insights into whether sediment deposition has continued on the submerged levees visible on the Chattahoochee arm of the reservoir and enable the analysis and interpretation of hyperpycnal inflows contributing to the growth of the Chattahoochee delta. Moreover, more complete survey coverage would facilitate the calculation of sedimentation rates from 1957–present for all USACE rangelines (Table 4). In the absence of a complete bathymetric survey, an updated survey at the 21 USACE rangelines that sample Lake Seminole would also be useful for calculating the 1957–present sedimentation rates. Aside from collecting new datasets, it would be valuable to calculate a channel-focused sedimentation rate for each rangeline using the existing USACE cross section data. Based on visual observation, much of the sediment deposition is focused in the former Chattahoochee and Flint channels, so comparing these more rapid rates to the ones averaged across the entire cross section could provide helpful insights into sedimentation patterns. Calculating historic channel-focused sedimentation rates would also allow the 2023 bathymetric survey to be used in updating these rates since it does have good coverage of the former channels.

Chapter 5: Comparing Three Decades of Land-Cover Change in the Chattahoochee, Flint, and Spring Creek Watersheds

5.1 Introduction

Changes in land use or cover can augment or reduce the amount of sediment available to be transported to a river during overland runoff. For example, increased urban construction or timber harvesting can enhance erosion whereas reforestation and urban best-management practices (BMPs) can lessen erosion or more effectively trap eroded sediment (Murphy, 2020). Research has indicated that soil erosion rates are highest in cultivated lands and lowest in forested lands because agricultural practices like tilling expose soil to wind and rain whereas forests have dense roots systems that can anchor soil and absorb water to slow surface runoff (Aneseeye et al., 2020). Studies have also shown that land-use and land cover-changes result in soil erosion and sedimentation processes that can alter the hydrologic balance of watersheds: for example, Gashaw et al. (2019) found that the conversion of forested land into agricultural land increased sediment yield by 49% and soil erosion by 55% in the Andassa watershed in Ethiopia between 1985–2015. Thus, tracking the evolution of land cover—primarily the transition from forested areas to agricultural and urban ones—in the three watersheds that drain to Lake Seminole (the Chattahoochee, Flint, and Spring Creek basins) could provide insight into why sedimentation patterns differ in each arm of the reservoir. Of course, land cover modifications are just one of many factors impacting sediment yield in these watersheds, and sediment yield is, in turn, one of many factors influencing sedimentation in Lake Seminole. However, broadly comparing trends in sedimentation to spatial patterns in surface disturbances provides a useful starting point for better understanding which exogenic factors could be exerting a stronger influence on sedimentation in Lake Seminole.

In this study, a multi-date Landsat image and Random Forest Classifier (RFC) were used to evaluate land cover change in the Chattahoochee, Flint, and Spring Creek watersheds from

1993–2023 (Breiman, 2001). The Flint River watershed is primarily comprised of croplands, forests, and scattered rural developments whereas the Chattahoochee River watershed has more forested and urban areas. The Spring Creek watershed is almost entirely comprised of croplands but has some forested area at the northern edge of the watershed. Within these three watersheds, the dominant change process in the last three decades is the clearing of forests and other natural vegetation for urbanization, agricultural development, and the logging industry, which is highlighted by the land-cover change classes used in this study (Obata et al., 2020). The key research questions this study aimed to answer were:

- 1) How has land cover in the Chattahoochee, Flint, and Spring Creek watersheds changed over the course of the past three decades (1993-2023)?
- 2) Has one watershed undergone more substantial land-cover changes than the others?
- 3) What has the most dominant land-cover change class been in each watershed?

5.2 Methods

5.2.1 Training Data Selection

The training data were selected using Landsat 5 Collection 2 Level 1 images acquired on 07/31/1993 and 07/08/1993 and Landsat 8 Collection 2 Level 1 images acquired on 03/05/2023 and 10/22/2023. The 2023 images were selected from outside the growing season because the Landsat scenes collected from June 1-October 1 all included cloud cover over some portion of the study region. A total of six classes were selected for this analysis: *Stable Water*, *Stable Crops*, *Stable Natural Vegetation*, *Stable Developed*, *Natural Vegetation → Crops*, and *Natural Vegetation → Barren*. These classes were simplified from an original scheme of four stable classes and four change classes. The *Crops → Developed* and *Natural Vegetation → Water* (representing reservoir construction) classes were removed because, even after testing variations in the amount of training data used for these classes, they always produced large amounts of salt-

and-pepper noise over forested areas. This could have been because these classes constituted such a small portion of the study region; in fact, it was challenging to find training data for these classes because examples of them were so rare. Thus, a decision was made to incorporate both of these classes into the *Nat Veg* → *Developed* class. Even though this was an oversimplification, it did not appear to impact the accuracy of the *Nat Veg* → *Developed* class and, based on visual inspection, produced a more accurate map overall. As a note, the *Nat Veg* → *Developed* class not only included urbanization, but also the clearing of trees that was not followed by replanting, so change representing *Natural Veg* → *Barren*. Though the inclusion of *Stable Barren* and *Natural Veg* → *Barren* classes would have yielded more a more precise result, a decision was made to instead focus on overall accuracy due to the large size of the study region.

Training data were extracted using the principles outlined in Zhu et al. (2016). The proportional occurrence of each class was roughly estimated to be 10% *Water*, 40% *Natural Vegetation*, 30% *Stable Crops*, 10% *Developed*, 4% *Nat Veg* → *Crops*, and 3% *Nat Veg* → *Developed*. These proportions accounted for the minimum and maximum sizes recommended for each class to prevent unbalanced training data and the proportional occurrence of each land cover class in the final training data matched these values. Training data were hand-drawn as polygons in QGIS and exported as a shapefile that was then uploaded to Google Earth Engine. Data proportions were also determined in QGIS by calculating the area of each training data polygon in square kilometers, summarizing the data by class to get the total area of each class, and calculating a new field for the class proportion by dividing each class area by the total area of training data. Because this study area was similar in size to a Landsat scene, a total of 25,000 pixels of training data were used for classification.

5.2.2 Multi-date Image Classification

A direct multi-date approach with a supervised classification was used for the change detection analysis (Singh, 1989). Prior to creating the multi-date image, the Landsat 8 Level 2,

Collection 2, Tier 1 and Landsat 5 Level 2, Collection 2, Tier 1 datasets on Google Earth Engine were filtered for clouds using the CFMask Algorithm (Foga et al., 2017). An additional Normalized Difference Vegetation Index (NDVI) band was also added to each dataset. A “before” composite image of the study region was then generated using a quality mosaicking approach with the NDVI band and the Landsat 5 data collected from June 1-October 1, 1993. An “after” composite was also generated using the same process for the Landsat 8 data collected from June 1-October 1, 2023. These two composites were then combined into a single, 14-band multi-date image using the image collection function in Google Earth Engine. This multi-date image was used as the input for the image classification, which was also performed in Google Earth Engine using an RFC with 200 decision trees (Breiman, 2001).

5.2.3 Post-Classification Correction

A single image classification was performed on the Chattahoochee, Flint, and Spring Creek watersheds because all three are adjacent to one another. Following this classification, the resulting map was imported into ArcGIS Pro and the Pixel Editor tools were used to conduct a final edit of the water bodies in the map. For most of the reservoirs in the study region, there were no cloud-free observations during either 1993 or 2023, so the waterbodies feature layer from the National Hydrography Dataset (NHD) was used as a guide to reclassify these values from *NoData* to *Water*. The edited map was then reuploaded to Google Earth Engine and clipped to the outline of each watershed so a separate accuracy assessment and area estimation could be performed for each watershed.

5.2.4 Accuracy Assessment

An accuracy assessment was performed for each watershed following the methods outlined in Olofsson et al. (2014). The number of reference samples for each watershed was determined using equation 13 in Olofsson et al. (2014), the per-class user’s accuracies from a

prior lab assignment, and a target standard error of 0.015 for the Chattahoochee and Flint watersheds and 0.025 for the Spring Creek watershed. Lower target standard error values were initially tested for each watershed; however, the number of reference samples required was not feasible, so these values were lowered. The target standard error for Spring Creek was raised so the number of samples matched the small size of the watershed relative to the other two.

Stratified random samples of 645, 656, and 225 points were generated in Google Earth Engine for the Chattahoochee, Flint, and Spring Creek watersheds, respectively. For the Chattahoochee and Flint River watersheds, a minimum of 50 samples per class was used and, for the Spring Creek watershed, a minimum of 25 samples per class was used. After these per-class minima were met, the remaining number of samples were allocated proportionally based on the map area of each remaining stratum. These sample points were then imported into ArcGIS Pro and Google Earth Pro and each point was manually assigned a classification in ArcGIS Pro using the 1993 USGS Digital Orthophoto Quadrangles (DOQs) and 2023 Airbus imagery in Google Earth Pro as reference data. These three shapefiles were uploaded to Google Earth Engine and used to tabulate confusion matrices. These confusion matrices and the pixel counts per mapped class in each watershed were then used to create probability matrices and estimate per-class user's and producer's accuracies, the true proportion of each class, and corrected area estimates with 95% confidence intervals for each watershed. User's accuracies account for errors of commission and relay the probability that a pixel belonging to a certain category on a map actually represents that category on the ground whereas producer's accuracies account for errors of omission and relay the probability that a feature on the ground will be correctly classified on the map.

5.3 Results

The products generated in this study were: (i) a map of land-cover change in each watershed (Figure 28); (ii) a confusion matrix (Table 6, Table 7, and Table 8) and probability matrix (Table 9, Table 10, and Table 11) for each watershed including per-class user's and

producer's accuracies; and (iii) adjusted area estimates with 95% confidence intervals for the land-cover classes in each watershed (Table 12, Table 13, and Table 14).

Beginning with the stable change classes, high user's (> 93%) and producer's (> 80%) accuracies were observed for the *Water* and *Natural Vegetation* classes in all three watersheds. Excluding the *Water* class from the Chattahoochee watershed, which was incorrectly labeled as *Natural Vegetation* in a few instances, producer's accuracies were all > 92%. For the *Crops* class, user's accuracies were all > 79% and producer's accuracies were all > 89%. The user's accuracy for the *Crops* class in the Spring Creek watershed (95%) was notably higher than the Chattahoochee (79%) watershed, with the *Crops* class in the Chattahoochee watershed incorrectly incorporating several areas that were actually *Natural Vegetation*. User's and producer's accuracies for the *Developed* class were also relatively high (> 70%), with the highest user's accuracy in the Chattahoochee watershed (82%) and highest producer's accuracy in the Spring Creek watershed (93%). There were some issues with the *Developed* class in the Flint and Spring Creek watersheds mistakenly including areas that were *Crops*, which led to lower user's accuracies around 70%.

The *Nat Veg* → *Crops* change class was by far the most problematic class. In the Chattahoochee watershed, the user's and producer's accuracies for the *Nat Veg* → *Crops* class were 24% and 32%, respectively, suggesting significant errors of both commission and omission. This class most often erroneously incorporated areas that belonged to the *Natural Vegetation* or *Crops* classes, with only 12 of the 50 reference samples actually representing a change from natural vegetation to crops. In the Flint Watershed, the *Nat Veg* → *Crops* class had a user's accuracy of 48% and a producer's accuracy of 60%. While these percentages were still low overall, they did represent a large improvement over the performance of this class in the Chattahoochee watershed. As was the case in the Chattahoochee

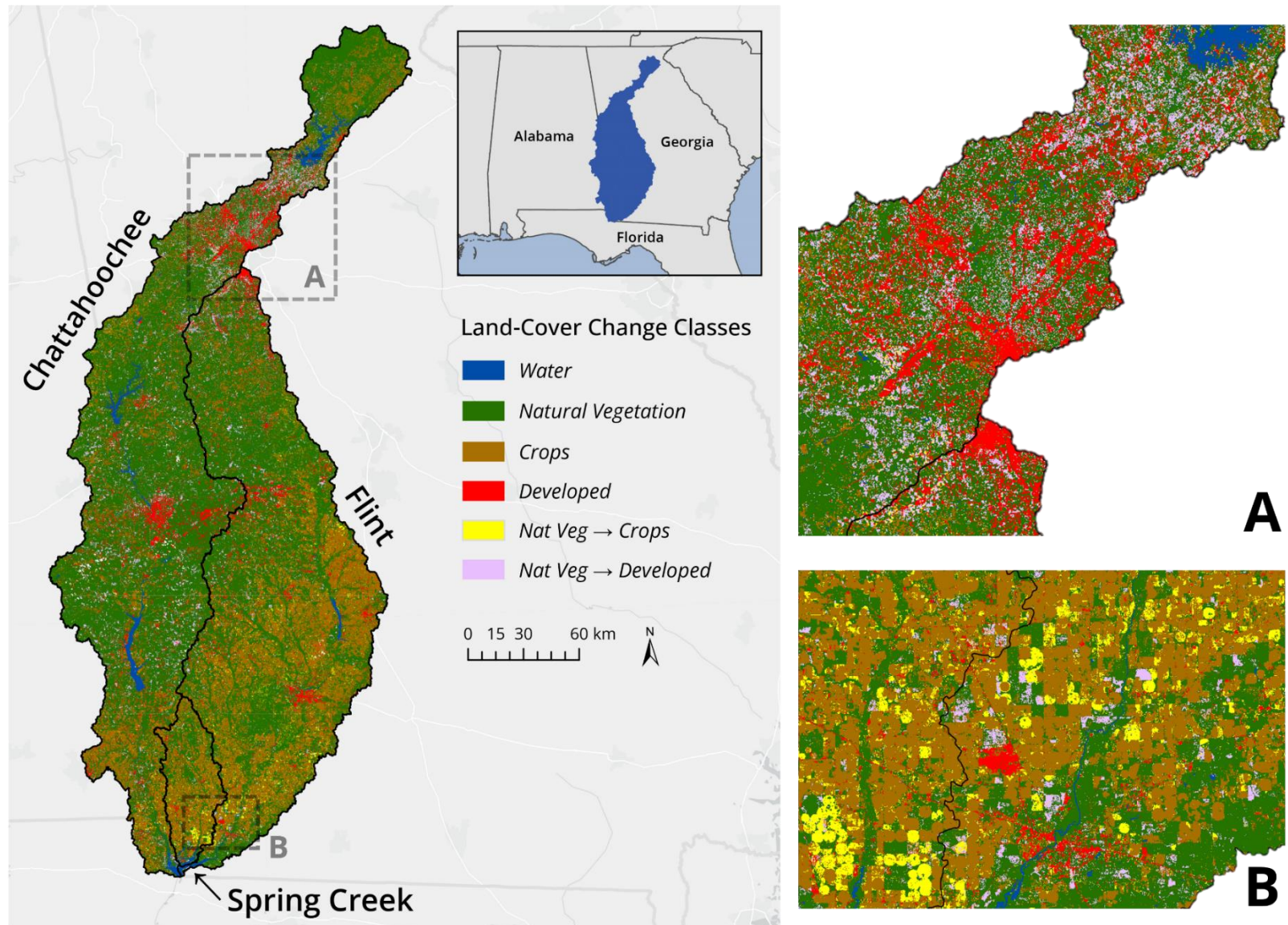


Figure 28. Land-cover change in the Chattahoochee, Flint, and Spring Creek watersheds from 1993–2023. Panels A and B show zoomed in maps of the region with the highest concentration of the Nat Veg → Developed class (A) and the Nat Veg → Crops class (B).

Table 6. Confusion matrix comparing reference data assessments with map categories for the Chattahoochee River watershed.

		Reference						Samples	User's accuracy (%)
		Water	Nat Veg	Crops	Developed	Nat → Crops	Nat → Dev		
Map	Water	49	0	0	1	0	0	50	98.00
	Nat Veg	3	352	2	3	1	3	364	96.70
	Crops	0	11	64	5	0	1	81	79.01
	Developed	0	5	3	41	0	1	50	82.00
	Nat → Crops	0	14	17	2	12	5	50	24.00
	Nat → Dev	0	2	0	1	2	45	50	90.00
	Total		52	384	86	53	15	55	645

Table 7. Confusion matrix comparing reference data assessments with map categories for the Flint River watershed.

		Reference						Samples	User's accuracy (%)
		Water	Nat Veg	Crops	Developed	Nat → Crops	Nat → Dev		
Map	Water	49	1	0	0	0	0	50	98.00
	Nat Veg	0	275	8	5	3	1	292	94.18
	Crops	0	14	146	2	1	1	164	89.02
	Developed	0	6	8	35	0	1	50	70.00
	Nat → Crops	0	11	14	0	24	1	50	48.00
	Nat → Dev	0	5	0	1	3	41	50	82.00
	Total		49	312	176	43	31	45	656

Table 8. Confusion matrix comparing reference data assessments with map categories for the Spring Creek watershed.

		Reference						Samples	User's accuracy (%)
		Water	Nat Veg	Crops	Developed	Nat → Crops	Nat → Dev		
Map	Water	25	0	0	0	0	0	25	100.00
	Nat Veg	0	54	1	0	1	0	56	96.43
	Crops	0	2	66	0	1	0	69	95.65
	Developed	0	1	6	18	0	0	25	72.00
	Nat → Crops	0	2	2	1	20	0	25	80.00
	Nat → Dev	1	0	1	0	2	21	25	84.00
	Total		26	59	76	19	24	21	225

Table 9. Probability matrix for the Chattahoochee River watershed.

		Reference					Samples	Map proportions	
		Water	Nat Veg	Crops	Developed	Nat → Crops			Nat → Dev
Map	Water	0.0249	0.0000	0.0000	0.0005	0.0000	0.0000	50	0.0254
	Nat Veg	0.0056	0.6611	0.0038	0.0056	0.0019	0.0056	364	0.6836
	Crops	0.0000	0.0204	0.1186	0.0093	0.0000	0.0019	81	0.1501
	Developed	0.0000	0.0067	0.0040	0.0551	0.0000	0.0013	50	0.0672
	Nat → Crops	0.0000	0.0024	0.0030	0.0003	0.0021	0.0009	50	0.0087
	Nat → Dev	0.0000	0.0026	0.0000	0.0013	0.0026	0.0585	50	0.0650
	True proportions	0.0305	0.6932	0.1293	0.0721	0.0066	0.0682		
	Producer's accuracy (%)	81.54	95.37	91.70	76.35	31.74	85.78	77.08 (avg)	

Table 10. Probability matrix for the Flint River watershed.

		Reference					Samples	Map proportions	
		Water	Nat Veg	Crops	Developed	Nat → Crops			Nat → Dev
Map	Water	0.0076	0.0002	0.0000	0.0000	0.0000	0.0000	50	0.0077
	Nat Veg	0.0000	0.5321	0.0155	0.0097	0.0058	0.0019	292	0.5650
	Crops	0.0000	0.0269	0.2807	0.0038	0.0019	0.0019	164	0.3153
	Developed	0.0000	0.0060	0.0080	0.0351	0.0000	0.0010	50	0.0502
	Nat → Crops	0.0000	0.0066	0.0084	0.0000	0.0144	0.0006	50	0.0300
	Nat → Dev	0.0000	0.0032	0.0000	0.0006	0.0019	0.0261	50	0.0319
	True proportions	0.0076	0.5749	0.3126	0.0493	0.0240	0.0316		
	Producer's accuracy (%)	100.00	92.54	89.79	71.28	59.88	82.71	82.70 (avg)	

Table 11. Probability matrix for the Spring Creek watershed.

		Reference					Samples	Map proportions	
		Water	Nat Veg	Crops	Developed	Nat → Crops			Nat → Dev
Map	Water	0.0151	0.0000	0.0000	0.0000	0.0000	0.0000	25	0.0151
	Nat Veg	0.0000	0.3812	0.0071	0.0000	0.0071	0.0000	56	0.3954
	Crops	0.0000	0.0139	0.4588	0.0000	0.0070	0.0000	69	0.4797
	Developed	0.0000	0.0015	0.0090	0.0270	0.0000	0.0000	25	0.0375
	Nat → Crops	0.0000	0.0041	0.0041	0.0020	0.0407	0.0000	25	0.0509
	Nat → Dev	0.0009	0.0000	0.0009	0.0000	0.0017	0.0180	25	0.0215
	True proportions	0.0160	0.4007	0.4798	0.0290	0.0564	0.0180		
	Producer's accuracy (%)	94.62	95.14	95.63	92.99	72.13	100.00	91.75 (avg)	

Table 12. Area estimates, adjusted area estimates of the final map classes, and 95% confidence intervals for the adjusted area estimates for the Chattahoochee River watershed.

Class	Map Estimate		Corrected Map Estimate		95% CI
	(% of total area)	(km ²)	(% of total area)	(km ²)	(km ²)
Water	2.54	682	3.05	820	173
Nat Veg	68.36	18,358	69.32	18,616	488
Crops	15.01	4,031	12.93	3,473	405
Developed	6.72	1,803	7.21	1,937	343
Nat → Crops	0.87	233	0.66	176	140
Nat → Dev	6.50	1,746	6.82	1,832	256

Table 13. Area estimates, adjusted area estimates of the final map classes, and 95% confidence intervals for the adjusted area estimates for the Flint River watershed.

Class	Map Estimate		Corrected Map Estimate		95% CI
	(% of total area)	(km ²)	(% of total area)	(km ²)	(km ²)
Water	0.77	182	0.76	178	7
Nat Veg	56.50	13,295	57.49	13,530	501
Crops	31.53	7,419	31.26	7,356	460
Developed	5.02	1,181	4.93	1,160	281
Nat → Crops	3.00	705	2.40	565	209
Nat → Dev	3.19	750	3.16	743	159

Table 14. Area estimates, adjusted area estimates of the final map classes, and 95% confidence intervals for the adjusted area estimates for the Spring Creek watershed.

Class	Map Estimate		Corrected Map Estimate		95% CI
	(% of total area)	(km ²)	(% of total area)	(km ²)	(km ²)
Water	1.51	36	1.60	38	4
Nat Veg	39.54	949	40.07	962	67
Crops	47.97	1,151	47.98	1,152	68
Developed	3.75	90	2.90	70	19
Nat → Crops	5.09	122	5.64	135	51
Nat → Dev	2.15	52	1.80	43	8

watershed, this class most often erroneously incorporated areas of *Natural Vegetation* or *Crops*. In contrast to the two larger watersheds, the *Nat Veg* → *Crops* class performed well in the largely-agricultural Spring Creek watershed, with user's and producer's accuracies of 84% and 72%, respectively. For the *Nat Veg* → *Developed* class, user's and producer's accuracies were > 82% in all three watersheds, with the highest user's accuracy in the Chattahoochee watershed (90%) and highest producer's accuracy in the Spring Creek watershed (100%), representing a much-improved performance compared to the *Nat Veg* → *Crops* class. For all classes in the land-cover change assessment, the Spring Creek watershed had both the highest average user's accuracy

(88%) and producer's accuracy (92%) and the Chattahoochee watershed had the lowest, with an average user's accuracy of 78% and an average producer's accuracy of 77%.

Looking at Figure 28, most of the *Nat Veg* → *Crops* changes are clustered within the Spring Creek and Flint watersheds and much of the *Nat Veg* → *Developed* changes are located around the outskirts of Atlanta and Columbus in the Chattahoochee watershed. In terms of adjusted area estimates, the area estimates with a 95% confidence interval for the *Nat Veg* → *Crops* class were $176 \pm 140 \text{ km}^2$ for the Chattahoochee watershed, $565 \pm 209 \text{ km}^2$ for the Flint, and $135 \pm 51 \text{ km}^2$ for Spring Creek. This class comprised less than 1% of the total area in the Chattahoochee watershed, 2.4% of the total area in the Flint, and 5.6% of the total area in Spring Creek. For the *Nat Veg* → *Developed* class, area estimates with a 95% confidence interval were $1,832 \pm 256 \text{ km}^2$ for the Chattahoochee watershed, $743 \pm 159 \text{ km}^2$ for the Flint, and $43 \pm 8 \text{ km}^2$ for Spring Creek, comprising 6.8%, 3.2%, and 1.8% of the total area, respectively. This means that, between 1993 and 2023, 7.5% of the Chattahoochee, 5.6% of the Flint, and 7.4% of the Spring Creek watersheds underwent land-cover changes, with *Nat Veg* → *Developed* being the most prevalent change class in the Chattahoochee, *Nat Veg* → *Developed* and *Nat Veg* → *Crops* comprising similar proportions in the Flint, and *Nat Veg* → *Crops* being the dominant change class in the Spring Creek watershed.

5.4 Discussion and Conclusions

Despite the ongoing processes of land-cover change in the three watersheds that drain to Lake Seminole, most of the land surface (93.4%) was comprised of stable land-cover classes between 1993 and 2023, with 6.6% of the total area undergoing land-cover change (Figure 28). Of the three watersheds, the Chattahoochee had the highest percentage of land-cover change (Table 12), followed by Spring Creek (Table 14), and then the Flint (Table 14); however, the difference of 7.5% land-cover change area in the Chattahoochee versus 5.6% land-cover change area in the Flint does not seem significantly different to explain the differences in sedimentation rates between the two arms of the reservoir. Additionally, the Chattahoochee and Spring Creek

watersheds had nearly identical percentages of land-cover change (7.5% and 7.4%, respectively), so, if land-cover change is a dominant factor in determining sediment supply for reservoir sedimentation and delta formation, then the Spring Creek arm of the reservoir should have a tributary delta or, at least, higher subaqueous sedimentation rates. Moreover, because Atlanta and Columbus are the loci of the *Nat Veg* → *Developed* class in the Chattahoochee watershed, much of the sediment generated by this type of land-cover disturbance was probably trapped by dams upstream of Lake Seminole (Figure 28). Land-cover change is likely one of many factors exerting an influence on sedimentation patterns in the different arms of Lake Seminole, and this project has provided a useful starting point for future land-cover assessments in focused areas of these three watersheds.

Furthermore, these conclusions need to be considered in the context of the low user's and producer's accuracies and large confidence intervals for the *Nat Veg* → *Crops* class (Tables 6–14). A previous land-cover change assessment conducted as a part of this research for a small region directly adjacent to Lake Seminole indicated that the *Developed* and *Nat Veg* → *Crops* classes could be challenging to get correct due to the low user's and producer's accuracies observed. One step taken to combat this was shifting the image compositing period to later in the growing season in the hopes that more fields would be planted and there would be less confusion between fallow fields, barren areas, and urban development. Unfortunately, June 1-October 1 was used as the compositing time period in this study due to a lack of cloud-free observations; being able to focus on July 1-September 1 would have been ideal.

In addition, it was interesting that the performance of the *Nat Veg* → *Crops* class improved as the percentage of total map area increased. That is to say, the more of that class was present in a watershed, the better the overall class accuracy was. Looking at Figure 28, most of the area of *Nat Veg* → *Crops* was concentrated in the Spring Creek watershed, where the user's and producer's accuracies were double and triple what they were for the Chattahoochee watershed, where this class comprised less than 1% of the total area. One way to possibly

improve this analysis could be conducting separate image classifications for each watershed rather than clipping a single classification to each watershed's boundaries. Though there should be no major differences in the spectral signature of each class between the watersheds, the strategy of selecting training data proportional to the occurrence of each class could have been more effective if separate training data was selected for each watershed. Additionally, this classification could have been improved with further post-classification correction (especially for the *Nat Veg* → *Crops* class) and the incorporation of additional ancillary data. For example, when implementing the Continuous Change Detection and Classification (CCDC) and LandTrendr algorithms to study land cover changes in a small portion of the Spring Creek watershed, the Normalized Burn Ratio (NBR) was more successful than NDVI or the Enhanced Vegetation Index (EVI) at detecting the transition from forest to crops, so an additional NBR band could be incorporated into the Landsat images.

In terms of future work, the most valuable research direction would be conducting a focused analysis of logging disturbances in the three watersheds. Because timber harvesting is often followed by reforestation, it can be missed by the endpoints change detection strategy implemented here. Even though the trees are replanted, the process of logging can generate large increases in sediment yield, which would be relevant to an analysis of sedimentation patterns in the different arms of Lake Seminole. To find change over shorter time intervals, a temporal segmentation approach like CCDC could be used (Zhu and Woodcock, 2014).

Chapter 6: Summary and Conclusions

Within Lake Seminole, there is evidence of both subaerial and subaqueous sediment deposition, with recent subaerial sedimentation rates slightly higher than subaqueous sedimentation rates. On the Chattahoochee River delta, subaerial sediment accumulated at a rate of 1.46 ± 0.48 cm/yr between 2007–2018 and subaqueous sediment accumulated at a rate of 1.28 cm/yr between 1957–2009 (Figure 20; Table 5). The most rapid areas of subaerial aggradation (> 4.5 cm/yr) on the Chattahoochee delta were located around the exterior edges of the islands whereas the interior wetlands were relatively stable (Figure 20).

In the Flint arm of the reservoir, where no subaerial deposits are present, subaqueous sediment eroded at a rate of -0.03 cm/yr between 1957–2009 (Table 5). However, based on updated bathymetric survey data, this erosional signal is focused in the upstream-most portion of the Flint arm and a depositional signal emerges further into the reservoir pool, where sediment accumulated at a rate of about 1.5 cm/yr between 2009–2023 (Figure 26).

Across the entire reservoir body, subaqueous sediment accumulated at a rate of 0.81 cm/yr between 1957–1976 and 0.12 cm/yr between 1976–2009, with the highest sedimentation rates occurring shortly after dam construction (Table 5). This is consistent with patterns observed in other reservoirs with deltaic deposits: because the upstream reach of the reservoir is narrow and shallow, a delta initially shows rapid advancement—leading to high subaerial and subaqueous sedimentation rates—before gradually slowing as the delta reaches wider and deeper areas of the reservoir (Morris et al., 2023). Even though the rate of delta advance decreased with time, between 1957–2009, Lake Seminole experienced a total of 3.03×10^7 m³ of sediment deposition, which is equivalent to a 7% loss in reservoir water storage capacity.

One of the primary purposes of Lake Seminole is hydropower generation; therefore, management strategies like sluicing or turbidity current venting may be necessary in the future to release fine sediments downstream and slow the arrival of abrasive delta sediments at the hydroelectric intake area (Morris et al., 2020). Additionally, Lake Seminole serves as a key

resource for tourism and recreation activities, so adopting watershed sediment management practices to control upstream erosion and reduce the sediment yield entering the reservoir could be a more holistic approach to curtail the advancement of the delta (Morris et al., 2023). Going forward, the most important step to support sustainable sediment management in Lake Seminole is to continue monitoring subaqueous and subaerial sedimentation rates, ideally through the acquisition of additional lidar and bathymetric surveys every 10 years. Another vital area of exploration for Lake Seminole is the response of the Chattahoochee River delta to short-term, extreme weather events like Hurricane Michael (2018) and Hurricane Helene (2024), especially considering the increased frequency and intensity of hurricanes expected in the future due to anthropogenic climate change (Seneviratne et al., 2021).

Though only 6.6% of Lake Seminole’s watershed underwent land-cover change between 1993–2023, land use impacts from population increases are expected to increase sediment yields and, thus, reservoir sedimentation rates in the future (Figure 28; Dethier et al., 2022). This means it is vital to begin addressing and understanding sedimentation problems now. Adopting a proactive approach is especially important because it is challenging or, in some cases, impossible to recover large volumes of reservoir storage capacity once they are lost due to the high cost of sediment removal and the lack of adequate disposal sites available (Morris et al., 2023). A key challenge for reservoir sediment management in the United States going forward will be collecting and analyzing sufficient monitoring data, like bathymetric surveys, to accurately predict future sedimentation rates and identify appropriate mitigation measures. Ultimately, it is crucial to continue researching new sediment management techniques and conducting site-specific assessments to both understand how sedimentation has impacted individual reservoirs and prevent future storage losses.

References

- Aneseyee, A. B., Elias, E., Soromessa, T., & Feyisa, G. L. (2020). Land use/land cover change effect on soil erosion and sediment delivery in the Winike watershed, Omo Gibe Basin, Ethiopia. *Science of The Total Environment*, 728, 138776.
<https://doi.org/10.1016/j.scitotenv.2020.138776>
- Baena-Escudero, R., Guerrero-Amador, I. C., Rinaldi, M., & González-Sayago, A. (2021). Hydrological and geomorphic effects upstream of the Cantillana Dam along the Guadalquivir River (southern Spain). *Geomorphology*, 388, 107786.
<https://doi.org/10.1016/j.geomorph.2021.107786>
- Bates, C. C. (1953). Rational Theory of Delta Formation. *AAPG Bulletin*, 37(9), 2119–2162.
<https://doi.org/10.1306/5CEADD76-16BB-11D7-8645000102C1865D>
- Brasington, J., Langham, J., & Rumsby, B. (2003). Methodological sensitivity of morphometric estimates of coarse fluvial sediment transport. *Geomorphology*, 53(3), 299–316.
[https://doi.org/10.1016/S0169-555X\(02\)00320-3](https://doi.org/10.1016/S0169-555X(02)00320-3)
- Breiman, L. (2001). Random Forests. *Machine Learning*, 45(1), 5–32.
- Bricker, S. B., Longstaff, B., Dennison, W., Jones, A., Boicourt, K., Wicks, C., & Woerner, J. (2008). Effects of nutrient enrichment in the nation's estuaries: A decade of change. *Harmful Algae*, 8(1), 21–32. <https://doi.org/10.1016/j.hal.2008.08.028>
- Csiki, S., & Rhoads, B. L. (2010). Hydraulic and geomorphological effects of run-of-river dams. *Progress in Physical Geography: Earth and Environment*, 34(6), 755–780.
<https://doi.org/10.1177/0309133310369435>
- Darst, M.R. & Light, H.M. (2008) Drier Forest Composition Associated with Hydrologic Change in the Apalachicola River, Florida, Scientific Investigations Report 2008-5062. Reston, VA: U.S. Geological Survey.
- Dethier, E. N., Renshaw, C. E., & Magilligan, F. J. (2022). Rapid changes to global river suspended sediment flux by humans. *Science*, 376(6600), 1447–1452.
<https://doi.org/10.1126/science.abn7980>
- Dewberry (2019). FL Panhandle Lidar Project Report Produced for U.S. Geological Survey, 149 p. https://noaa-nos-coastal-lidar-pds.s3.amazonaws.com/laz/geoid18/8945/supplemental/FL_Panhandle_Lidar_Project_Report_20190601.pdf
- Eidmann, J. S., Rathburn, S. L., White, D., & Huson, K. (2022). Channel Response and Reservoir Delta Evolution From Source to Sink Following an Extreme Flood. *Journal of Geophysical Research: Earth Surface*, 127(2), e2020JF006013.
<https://doi.org/10.1029/2020JF006013>
- Eubanks, M. J., & Donald, M. M. (2001). Lake Seminole Hydrilla Action Plan: Development and Implementation. Proceedings of the 2001 Georgia Water Resources Conference, held March 26-27, 2001, at the University of Georgia. Kathryn J. Hatcher, editor, Institute of Ecology, the University of Georgia, Athens, Georgia.
<https://repository.gatech.edu/server/api/core/bitstreams/65c3c139-9b31-4acf-80ff-671e57b433e4/content>
- Evans, J. E., Huxley, J. M., & Vincent, R. K. (2007). Upstream Channel Changes Following Dam Construction and Removal Using a GIS/Remote Sensing Approach1. *JAWRA Journal of the American Water Resources Association*, 43(3), 683–697.
<https://doi.org/10.1111/j.1752-1688.2007.00055.x>
- Foga, S., Scaramuzza, P.L., Guo, S., Zhu, Z., Dilley, R.D., Beckmann, T., Schmidt, G.L., Dwyer,

- J.L., Hughes, M.J., Laue, B. (2017). Cloud detection algorithm comparison and validation for operational Landsat data products. *Remote Sensing of Environment*, 194, 379-390.
- Gashaw, T., Tulu, T., Argaw, M., & Worqlul, A. W. (2019). Modeling the impacts of land use–land cover changes on soil erosion and sediment yield in the Andassa watershed, upper Blue Nile basin, Ethiopia. *Environmental Earth Sciences*, 78(24), 679.
<https://doi.org/10.1007/s12665-019-8726-x>
- Gilbert, G. K. (1885). The topographic features of lake shores, *Annu. Rep. USGS*, 5, 69–123.
- Hopkinson, C., Chasmer, L. E., Sass, G., Creed, I. F., Sitar, M., Kalbfleisch, W., & Treitz, P. (2005). Vegetation class dependent errors in lidar ground elevation and canopy height estimates in a boreal wetland environment. *Canadian Journal of Remote Sensing*, 31(2), 191–206. <https://doi.org/10.5589/m05-007>
- Jackson, C. R., & Pringle, C. M. (2010). Ecological Benefits of Reduced Hydrologic Connectivity in Intensively Developed Landscapes. *BioScience*, 60(1), 37–46.
<https://doi.org/10.1525/bio.2010.60.1.8>
- Johnson, K. M., Snyder, N. P., Castle, S., Hopkins, A. J., Waltner, M., Merritts, D. J., & Walter, R. C. (2019). Legacy sediment storage in New England river valleys: Anthropogenic processes in a postglacial landscape. *Geomorphology*, 327, 417–437.
<https://doi.org/10.1016/j.geomorph.2018.11.017>
- Jones, D. J. (1965). The Gilbert-Type Delta. *AAPG Bulletin*, 49(3), 345.
<https://doi.org/10.1306/A663359A-16C0-11D7-8645000102C1865D>
- Juracek, K.E. (2015). The aging of America's reservoirs: in-reservoir and downstream physical changes and habitat implications. *JAWRA Journal of the American Water Resources Association*, 51(1), pp.168-184, <https://doi.org/10.1111/jawr.12238>
- Keith, M.K., Wallick, J.R., Taylor, G., Mangano, J., White, J., and Schenk, L. (2016). Geomorphic responses of gravel bed rivers to fine sediment releases during annual reservoir drawdowns: Spatial patterns and magnitude of aggradation along Fall Creek and Middle Fork Willamette River, Oregon: San Francisco, California, American Geophysical Union, 2016 Fall Meeting supplement, abstract EP53C-0984.
- Kostic, S., Parker, G., & Marr, J. G. (2002). Role of Turbidity Currents in Setting the Foreset Slope of Clinofolds Prograding into Standing Fresh Water. *Journal of Sedimentary Research*, 72(3), 353–362. <https://doi.org/10.1306/081501720353>
- Kucharczyk, M., Hugenholtz, C. H., & Zou, X. (2018). UAV–LiDAR accuracy in vegetated terrain. *Journal of Unmanned Vehicle Systems*, 6(4), 212–234.
<https://doi.org/10.1139/juvs-2017-0030>
- Lague, D., Brodu, N., & Leroux, J. (2013). Accurate 3D comparison of complex topography with terrestrial laser scanner: Application to the Rangitikei canyon (N-Z). *ISPRS Journal of Photogrammetry and Remote Sensing*, 82, 10–26.
<https://doi.org/10.1016/j.isprsjprs.2013.04.009>
- Lai, S. Y. J., & Capart, H. (2009). Reservoir infill by hyperpycnal deltas over bedrock. *Geophysical Research Letters*, 36(8). <https://doi.org/10.1029/2008GL037139>
- Langbein, W. B.; Iseri, Kathleen T. (1960). General Introduction and Hydrologic Definitions, Manual of Hydrology: Part 1. General Surface-Water Techniques: Geological Survey Water Supply Paper 1542-F. U.S. Geological Survey, 29 p.
- Light, H. M., Vincent, K. R., Darst, M. R., & Price, F. D. (2006). Water-level decline in the Apalachicola River, Florida, from 1954 to 2004, and effects on floodplain habitats. In *Water-level decline in the Apalachicola River, Florida, from 1954 to 2004, and effects on*

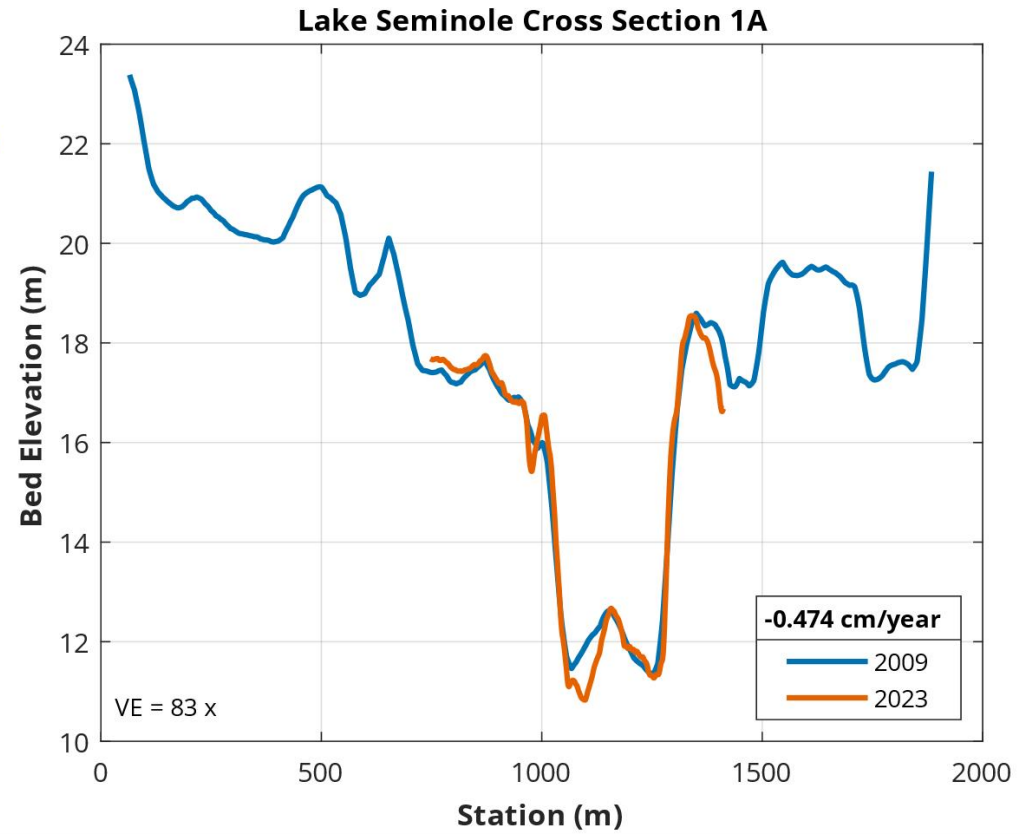
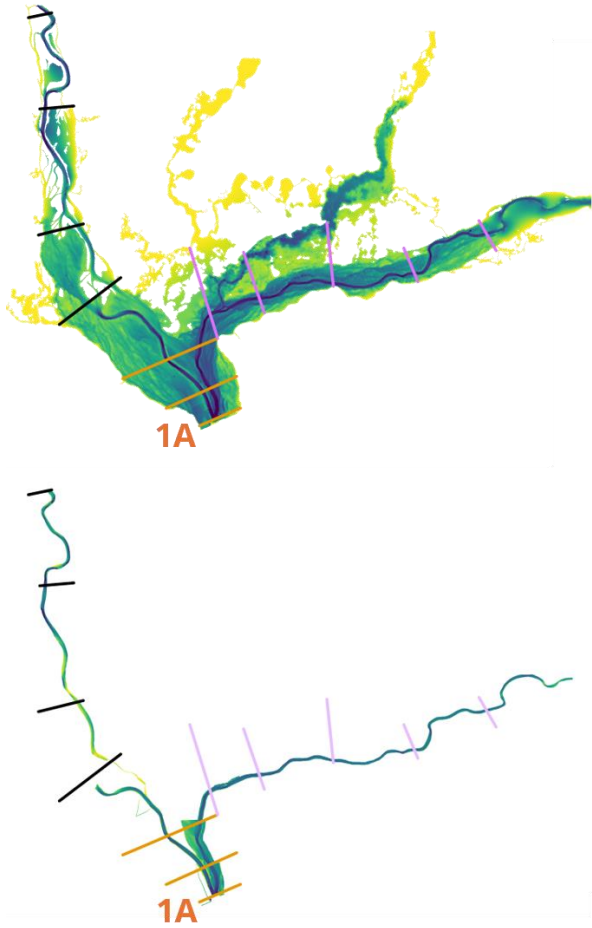
- floodplain habitats* (USGS Numbered Series No. 2006–5173; Scientific Investigations Report, Vols. 2006–5173, p. 61). <https://doi.org/10.3133/sir20065173>
- Liro, M. (2017). Dam-induced base-level rise effects on the gravel-bed channel planform. *CATENA*, 153, 143–156. <https://doi.org/10.1016/j.catena.2017.02.005>
- Liro, M. (2019). Dam reservoir backwater as a field-scale laboratory of human-induced changes in river biogeomorphology: A review focused on gravel-bed rivers. *Science of The Total Environment*, 651, 2899–2912. <https://doi.org/10.1016/j.scitotenv.2018.10.138>
- LoCascio, S. (2015). The Apalachicola-Chattahoochee-Fltin River Dispute: Atlanta vs. Apalachicola, Water Apportionments’ Real Version of David vs. Goliath. *Journal of Land Use & Environmental Law*, 30(2), 331–362.
- Luscombe, D. J., Anderson, K., Gatis, N., Wetherelt, A., Grand-Clement, E., & Brazier, R. E. (2015). What does airborne LiDAR really measure in upland ecosystems? *Ecohydrology*, 8(4), 584–594. <https://doi.org/10.1002/eco.1527>
- Meng, X., Currit, N., & Zhao, K. (2010). Ground Filtering Algorithms for Airborne LiDAR Data: A Review of Critical Issues. *Remote Sensing*, 2(3), Article 3. <https://doi.org/10.3390/rs2030833>
- Merrick & Company (Merrick) (2008). Northwest Florida Water Management District (NFWMD) Calhoun, Holmes, Washington, Jackson, and Liberty Counties (hereafter known as “5-Counties”) LiDAR Mapping Report, 49 p. https://noaa-nos-coastal-lidar-pds.s3.amazonaws.com/laz/geoid18/579/supplemental/NFWMD_5_Counties_Lidar_Mapping_Report.pdf
- Morris, G. L. (2020). Classification of Management Alternatives to Combat Reservoir Sedimentation. *Water*, 12(3), Article 3. <https://doi.org/10.3390/w12030861>
- Morris, G. L., Dahl, T. A., Ramos-Villanueva, M., Leech, J. R., Jonas, M. M. (2023). Sustainable Sediment Management at US Army Corps of Engineers Reservoirs. <https://doi.org/10.21079/11681/46470>
- Mossa, J., & Chen, Y.H. (2022). Geomorphic response to historic and ongoing human impacts in a large lowland river. *Earth Surface Processes and Landforms*, 47. <https://doi.org/10.1002/esp.5334>
- Murphy, J. C. (2020). Changing suspended sediment in United States rivers and streams: Linking sediment trends to changes in land use/cover, hydrology and climate. *Hydrology and Earth System Sciences*, 24(2), 991–1010. <https://doi.org/10.5194/hess-24-991-2020>
- National Oceanic and Atmospheric Administration (NOAA). Local Climatological Data (LCD). Bainbridge Decatur Co Industrial Air Park Airport, GA, US (WBAN:53882)
- Obata, S., Bettinger, P., Cieszewski, C. J., & Lowe III, R. C. (2020). Mapping Forest Disturbances between 1987–2016 Using All Available Time Series Landsat TM/ETM+ Imagery: Developing a Reliable Methodology for Georgia, United States. *Forests*, 11(3), Article 3. <https://doi.org/10.3390/f11030335>
- Olofsson, P., Foody, G. M., Herold, M., Stehman, S. V., Woodcock, C. E. and Wulder, M. A. (2014). Good Practices for Assessing Accuracy and Estimating Area of Land Change. *Remote Sensing of Environment*. 148, 42–57.
- Passalacqua, P., Belmont, P., Staley, D. M., Simley, J. D., Arrowsmith, J. R., Bode, C. A., Crosby, C., DeLong, S. B., Glenn, N. F., Kelly, S. A., Lague, D., Sangireddy, H., Schaffrath, K., Tarboton, D. G., Wasklewicz, T., & Wheaton, J. M. (2015). Analyzing high resolution topography for advancing the understanding of mass and energy transfer through landscapes: A review. *Earth-Science Reviews*, 148, 174–193. <https://doi.org/10.1016/j.earscirev.2015.05.012>

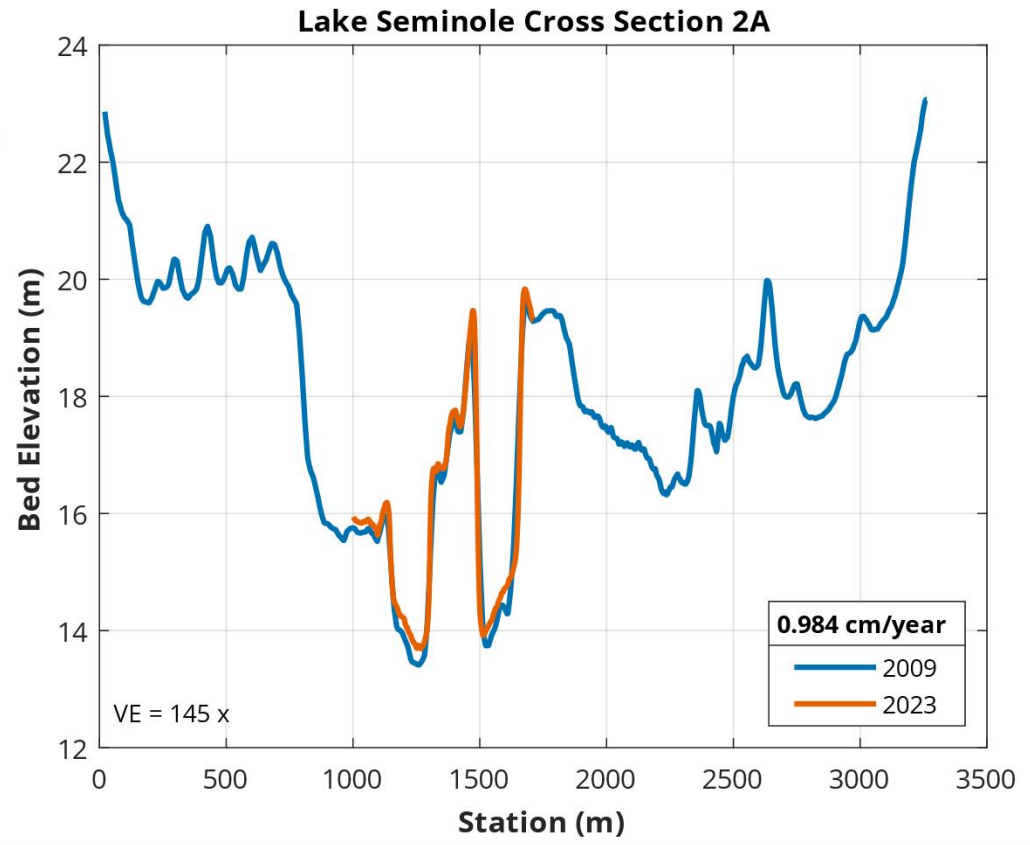
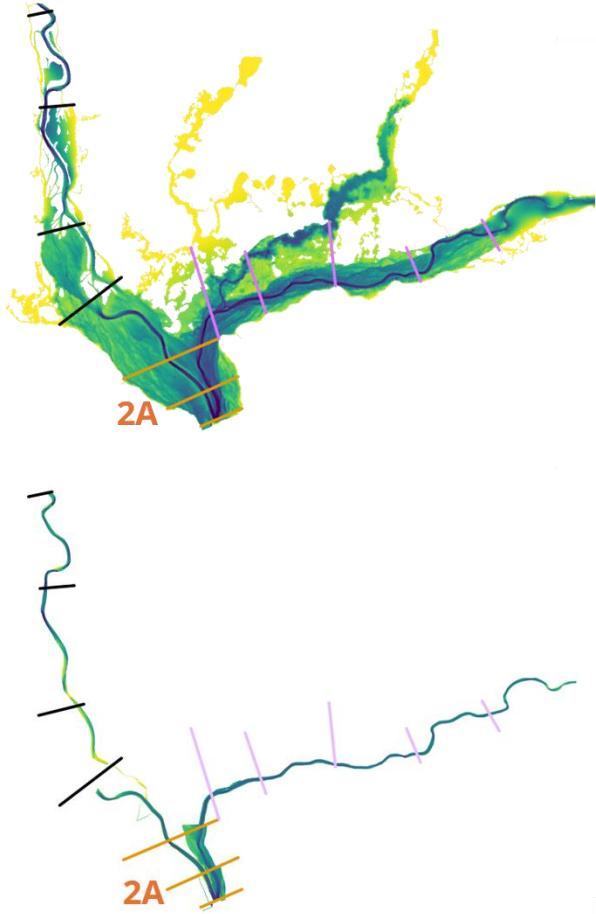
- Randle, T. J., Bountry, J. A., Ritchie, A., & Wille, K. (2015). Large-scale dam removal on the Elwha River, Washington, USA: Erosion of reservoir sediment. *Geomorphology*, 246, 709–728. <https://doi.org/10.1016/j.geomorph.2014.12.045>
- Rathburn, S. L., Bennett, G. L., Wohl, E. E., Briles, C., McElroy, B., & Sutfin, N. (2017). The fate of sediment, wood, and organic carbon eroded during an extreme flood, Colorado Front Range, USA. *Geology*, 45(6), 499–502. <https://doi.org/10.1130/G38935.1>
- Rouse, J.W., Haas, R.H., Schell, J.A., Deering, D.W. and Harlan, J.C. (1974). Monitoring the Vernal Advancement and Retrogradation (Green Wave Effect) of Natural Vegetation. NASA/GSFC Type III Final Report, 371 p.
- Rubi, R., Rohais, S., Bourquin, S., Moretti, I., & Desaubliaux, G. (2018). Processes and typology in Gilbert-type delta bottomset deposits based on outcrop examples in the Corinth Rift. *Marine and Petroleum Geology*, 92, 193–212. <https://doi.org/10.1016/j.marpetgeo.2018.02.014>
- Sadler, P. M., & Jerolmack, D. J. (2015). Scaling laws for aggradation, denudation and progradation rates: The case for time-scale invariance at sediment sources and sinks. *Geological Society, London, Special Publications*, 404(1), 69–88. <https://doi.org/10.1144/SP404.7>
- Sankey, T., Donager, J., McVay, J., & Sankey, J. B. (2017). UAV lidar and hyperspectral fusion for forest monitoring in the southwestern USA. *Remote Sensing of Environment*, 195, 30–43. <https://doi.org/10.1016/j.rse.2017.04.007>
- Scott, C., Phan, M., Nandigam, V., Crosby, C., & Arrowsmith, J. R. (2021). Measuring change at Earth’s surface: On-demand vertical and three-dimensional topographic differencing implemented in OpenTopography. *Geosphere*, 17(4), 1318–1332. <https://doi.org/10.1130/GES02259.1>
- Seneviratne, S.I., X. Zhang, M. Adnan, W. Badi, C. Dereczynski, A. Di Luca, S. Ghosh, I. Iskandar, J. Kossin, S. Lewis, F. Otto, I. Pinto, M. Satoh, S.M. Vicente-Serrano, M. Wehner, and B. Zhou (2021). Weather and Climate Extreme Events in a Changing Climate. In *Climate Change 2021: The Physical Science Basis. Contribution of Working Group I to the Sixth Assessment Report of the Intergovernmental Panel on Climate Change* [Masson-Delmotte, V., P. Zhai, A. Pirani, S.L. Connors, C. Péan, S. Berger, N. Caud, Y. Chen, L. Goldfarb, M.I. Gomis, M. Huang, K. Leitzell, E. Lonnoy, J.B.R. Matthews, T.K. Maycock, T. Waterfield, O. Yelekçi, R. Yu, and B. Zhou (eds.)]. Cambridge University Press, Cambridge, United Kingdom and New York, NY, USA, pp. 1513–1766, doi:10.1017/9781009157896.013
- Singh, A. (1989). Digital change detection techniques using remotely-sensed data. *International Journal of Remote Sensing*, 10, 989-1003.
- Snyder, N. P., Rubin, D. M., Alpers, C. N., Childs, J. R., Curtis, J. A., Flint, L. E., & Wright, S. A. (2004). Estimating accumulation rates and physical properties of sediment behind a dam: Englebright Lake, Yuba River, northern California. *Water Resources Research*, 40(11). <https://doi.org/10.1029/2004WR003279>
- Snyder, N. P., Wright, S. A., Alpers, C. N., Flint, L. E., Holmes, C. W., & Rubin, D. M. (2006). Reconstructing depositional processes and history from reservoir stratigraphy: Englebright Lake, Yuba River, northern California. *Journal of Geophysical Research: Earth Surface*, 111(F4). <https://doi.org/10.1029/2005JF000451>
- Stratton, L. E., & Grant, G. E. (2019). Autopsy of a reservoir: Facies architecture in a multdam system, Elwha River, Washington, USA. *GSA Bulletin*, 131(11–12), 1794–1822. <https://doi.org/10.1130/B31959.1>

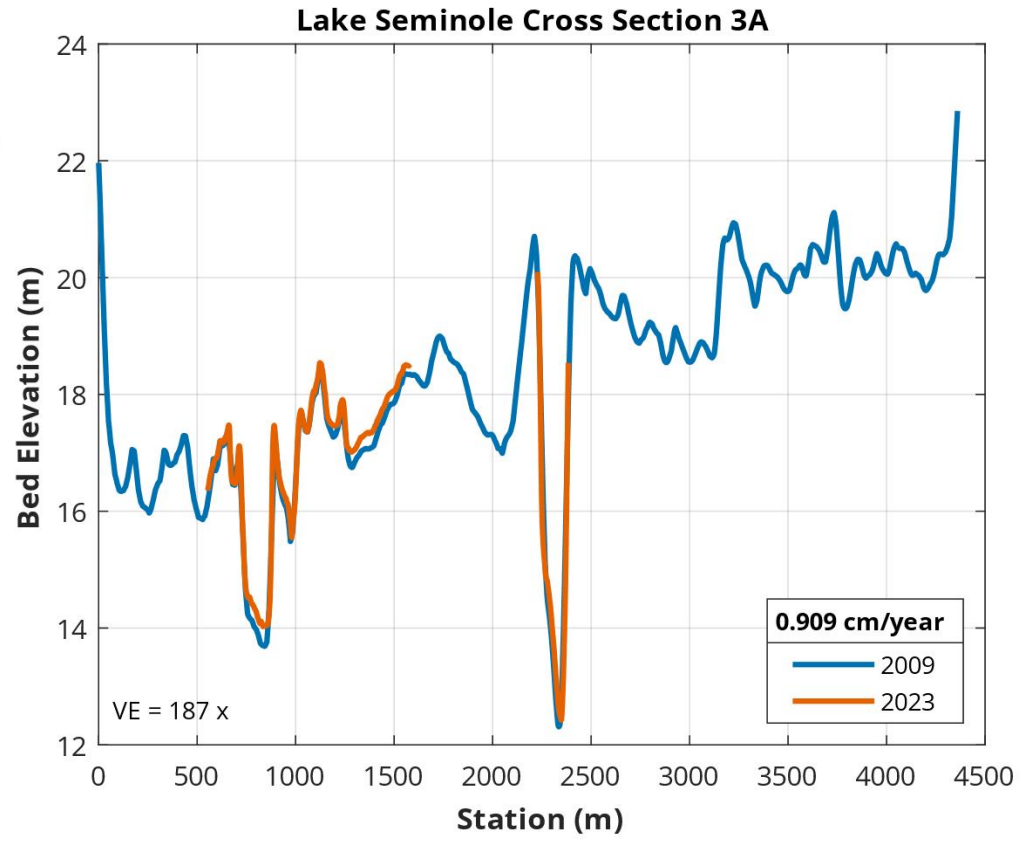
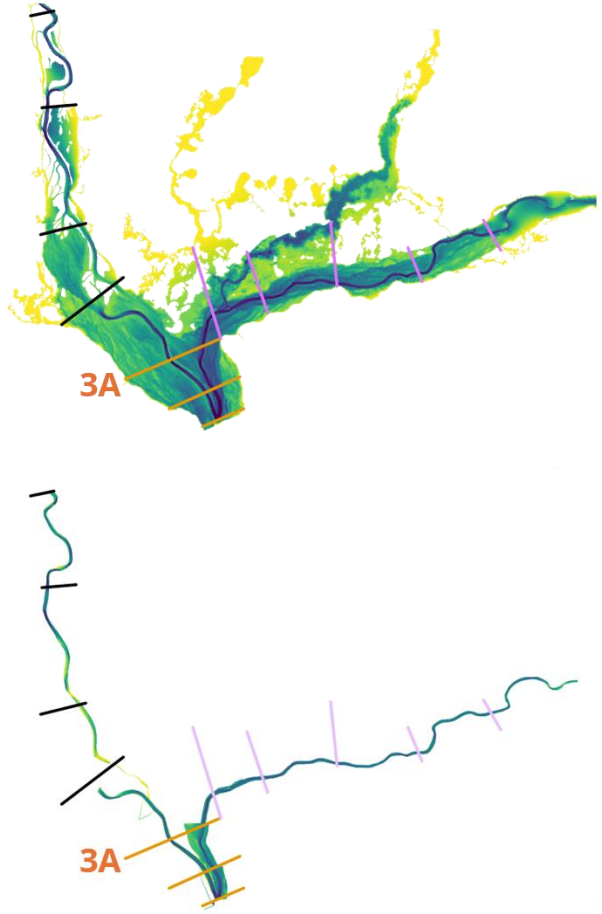
- Sullivan, G. M., & Feinn, R. (2012). Using Effect Size—Or Why the P Value Is Not Enough. *Journal of Graduate Medical Education*, 4(3), 279–282. <https://doi.org/10.4300/JGME-D-12-00156.1>
- Tetra Tech (2011). Sedimentation and Erosion Analysis for Lake Seminole: Jim Woodruff Lock and Dam, FL and GA, 228 p.
- Tetra Tech (2016). Appendix A: Jim Woodruff Lock and Dam and Lake Seminole Apalachicola River, Florida and Georgia. In Draft Environmental Impact Statement: Update of the Water Control Manual for the Apalachicola-Chattahoochee-Flint River Basin in Alabama, Florida, and Georgia and a Water Supply Storage Assessment, 184 p. https://www.sam.usace.army.mil/Portals/46/docs/planning_environmental/acf/docs/ACF%20DEIS%20Vol2_App%20A%20Jim%20Woodruff.pdf
- Torak, L.J., Crilley, D.M., and Painter, J.A. (2005). Physical and hydrochemical evidence of lake leakage near Jim Woodruff Lock and Dam and of ground-water inflow to Lake Seminole, and an assessment of karst features in and near the lake, southwestern Georgia and northwestern Florida: U.S. Geological Survey Scientific Investigations Report 2005-5084, 90 p.
- Töyrä, J., Pietroniro, A., Hopkinson, C., & Kalbfleisch, W. (2003). Assessment of airborne scanning laser altimetry (lidar) in a deltaic wetland environment. *Canadian Journal of Remote Sensing*, 29(6), 718–728. <https://doi.org/10.5589/m03-040>
- USACE Waterways Experiment Station (1952). Spillway and Lock Approach: Jim Woodruff Dam: Apalachicola River, Florida (Technical Memorandum No. 2-340). <https://usace.contentdm.oclc.org/digital/api/collection/p266001coll1/id/1643/download>
- Volke, M. A., Scott, M. L., Johnson, W. C., & Dixon, M. D. (2015). The Ecological Significance of Emerging Deltas in Regulated Rivers. *BioScience*, 65(6), 598–611. <https://doi.org/10.1093/biosci/biv040>
- Volke, M. A., Johnson, W. C., Dixon, M. D., & Scott, M. L. (2019). Emerging reservoir delta-backwaters: Biophysical dynamics and riparian biodiversity. *Ecological Monographs*, 89(3), e01363. <https://doi.org/10.1002/ecm.1363>
- Wagner, W., Lague, D., Mohrig, D., Passalacqua, P., Shaw, J., & Moffett, K. (2017). Elevation change and stability on a prograding delta. *Geophysical Research Letters*, 44(4), 1786–1794. <https://doi.org/10.1002/2016GL072070>
- Waters, M. N., Golladay, S. W., Patrick, C. H., Smoak, J. M., & Shivers, S. D. (2015). The potential effects of river regulation and watershed land use on sediment characteristics and lake primary producers in a large reservoir. *Hydrobiologia*, 749(1), 15–30. <https://doi.org/10.1007/s10750-014-2142-8>
- Wheaton, J. M., Brasington, J., Darby, S. E., & Sear, D. A. (2010). Accounting for uncertainty in DEMs from repeat topographic surveys: Improved sediment budgets. *Earth Surface Processes and Landforms*, 35(2), 136–156. <https://doi.org/10.1002/esp.1886>
- White, J. (2019). Get to Know Lake Seminole: How the bass fishing sets up for stop No. 3 of the 2019 FLW Tour. Major League Fishing. <https://majorleaguefishing.com/pro-circuit/2019-03-05-get-to-know-lake-seminole/>
- Wildman, R. A., Pratson, L. F., DeLeon, M., & Hering, J. G. (2011). Physical, Chemical, and Mineralogical Characteristics of a Reservoir Sediment Delta (Lake Powell, USA) and Implications for Water Quality during Low Water Level. *Journal of Environmental Quality*, 40(2), 575–586. <https://doi.org/10.2134/jeq2010.0323>
- Xu, J. (1990). Complex response in adjustment of the Weihe River channel to the construction of the Sanmenxia Reservoir. *Zeitschrift Für Geomorphologie*, 233–245.

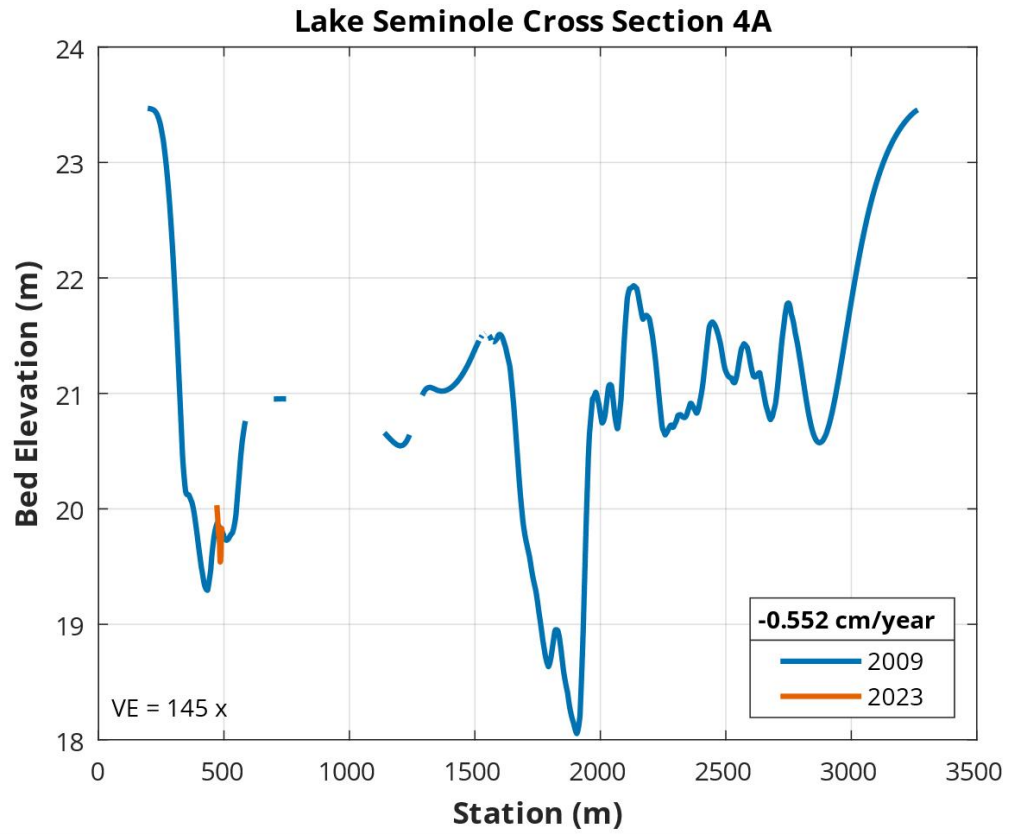
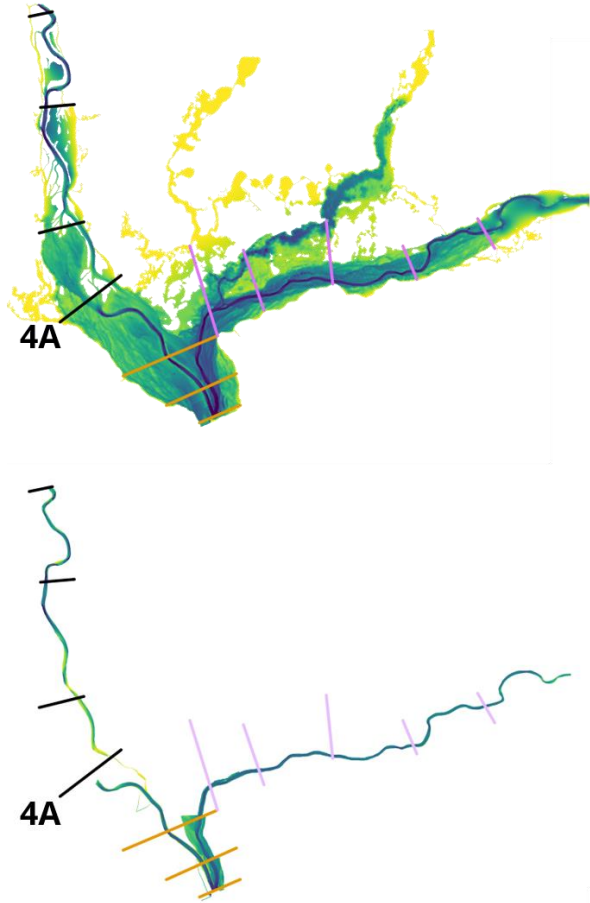
- <https://doi.org/10.1127/zfg/34/1990/233>
- Xu, J., & Shi, C. (1997). The river channel pattern change as influenced by the floodplain geoecosystem: An example from the Hongshan Reservoir. *Zeitschrift Für Geomorphologie*, 97–113. <https://doi.org/10.1127/zfg/41/1997/97>
- Zhao, G., Rasmussen, M. R., Larsen, K. G., Srba, J., Nielsen, T. D., Goorden, M. A., Qian, W., & Nielsen, J. E. (2023). Determine stormwater pond geometrics and hydraulics using remote sensing technologies: A comparison between airborne-LiDAR and UAV-photogrammetry field validation against RTK-GNSS. *Journal of Hydroinformatics*, 25(4), 1256–1275. <https://doi.org/10.2166/hydro.2023.178>
- Zhu, Z., & Woodcock, C. E. (2014). Continuous change detection and classification of land cover using all available Landsat data. *Remote Sensing of Environment*, 144, 152–171. <https://doi.org/10.1016/j.rse.2014.01.011>
- Zhu, Z., Gallant, A.L., Woodcock, C.E., Pengra, B., Olofsson, P., Loveland, T.R., Jin, S., Dahal, D., Yang, L., and R.F. Auch (2016). Optimizing selection of training and auxiliary data for operational land cover classification for the LCMAP initiative. *ISPRS Journal of Photogrammetry and Remote Sensing*, 122, 206–221.

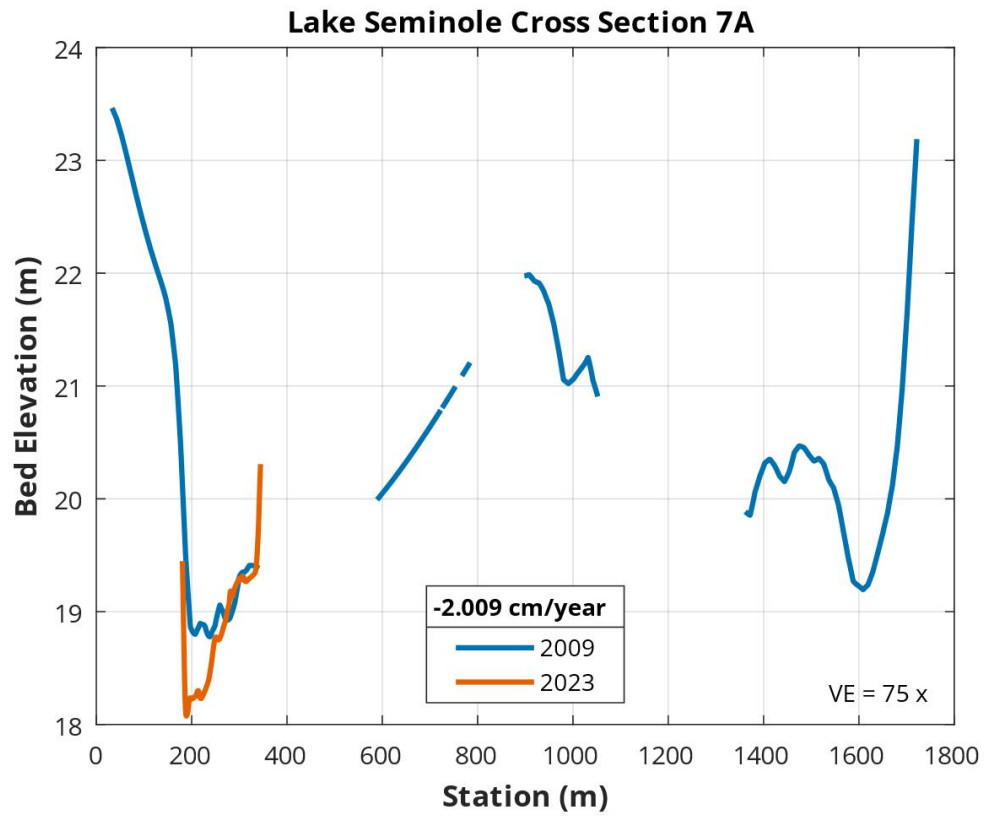
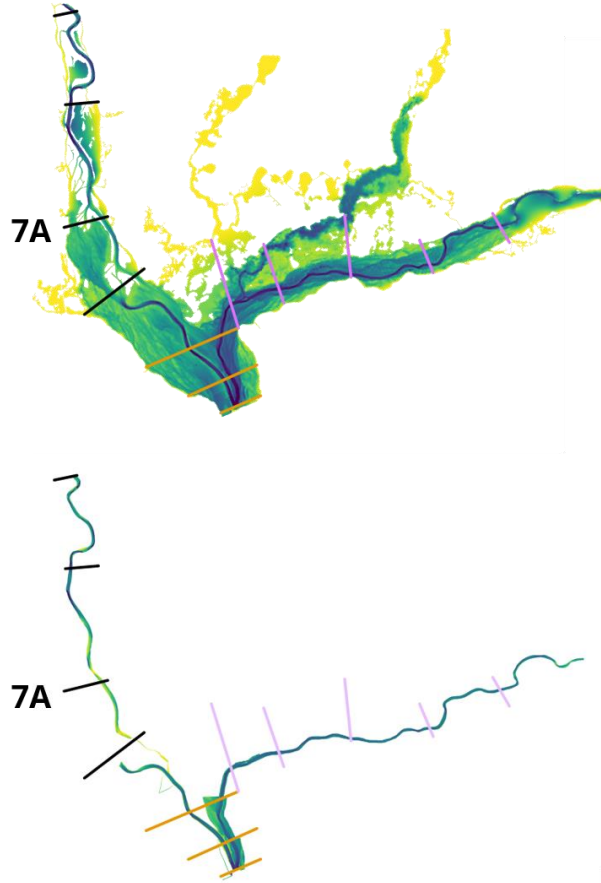
Appendix A: All Bathymetric Survey Cross Section Plots

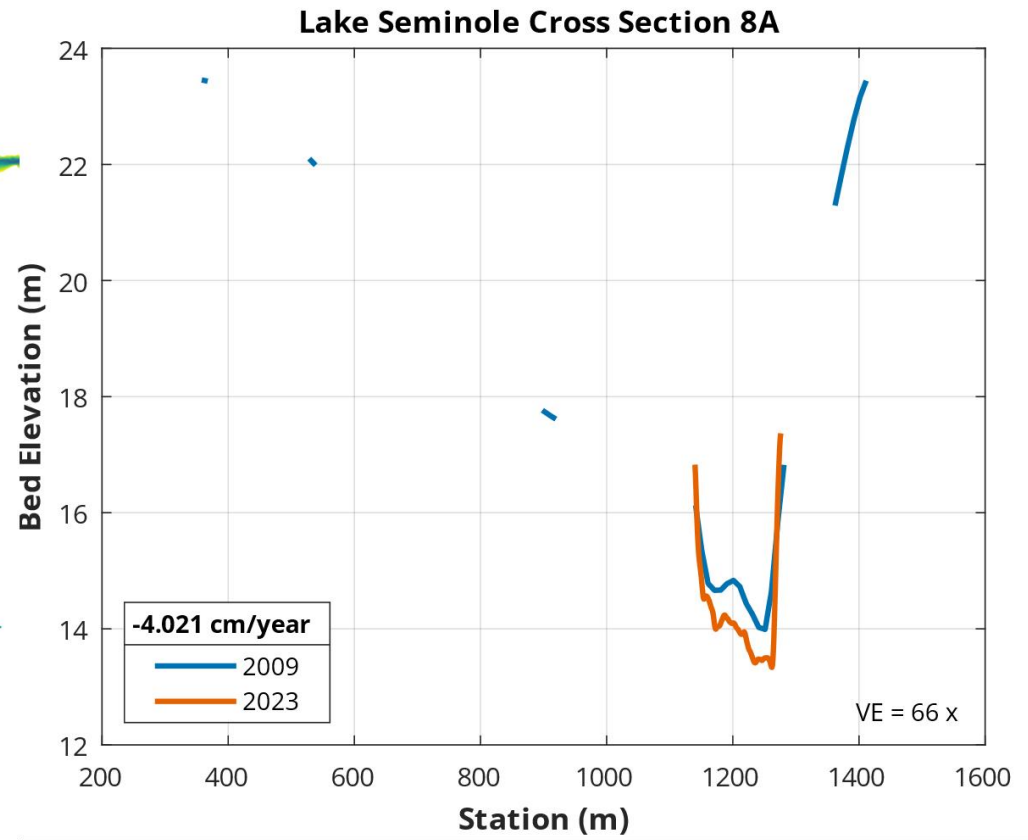
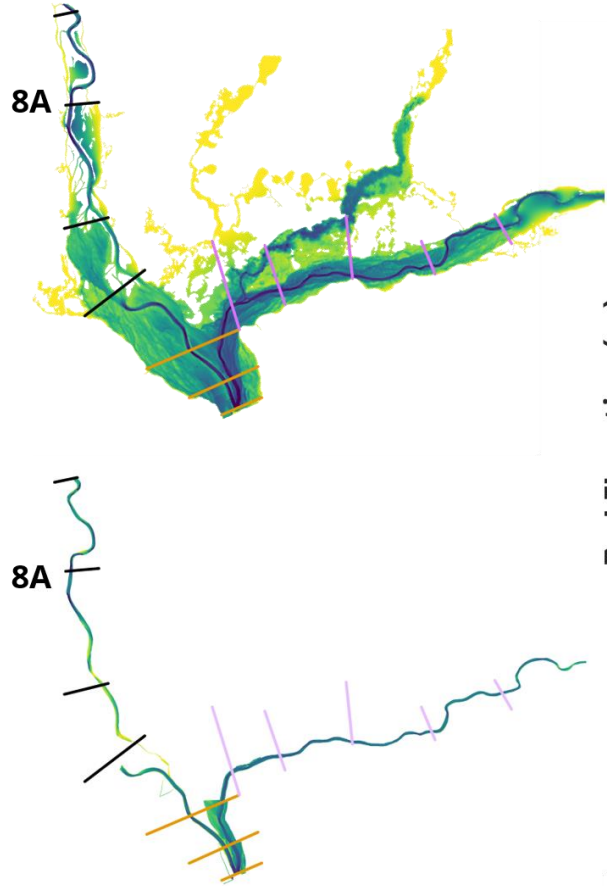


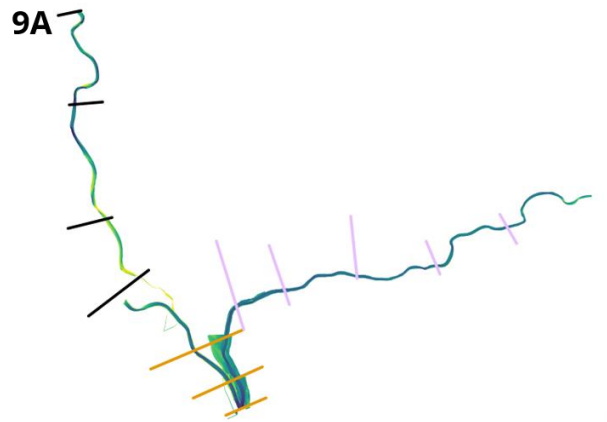
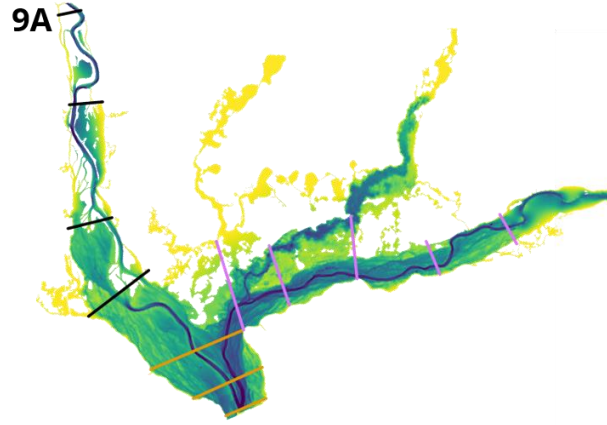




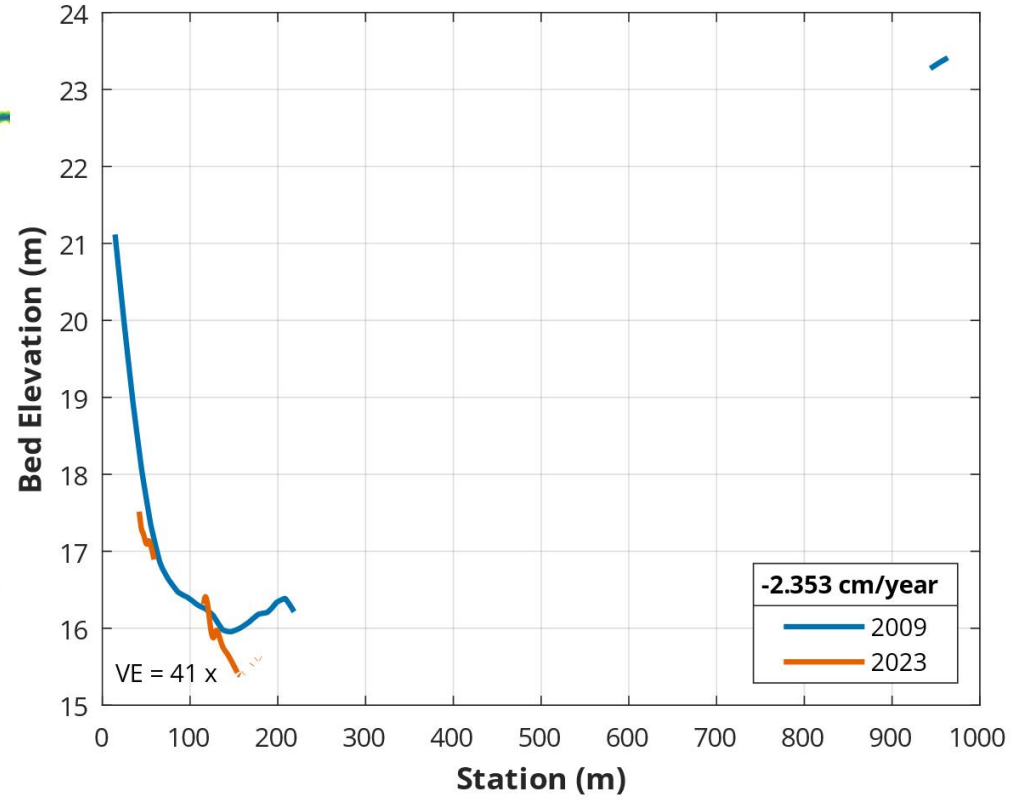


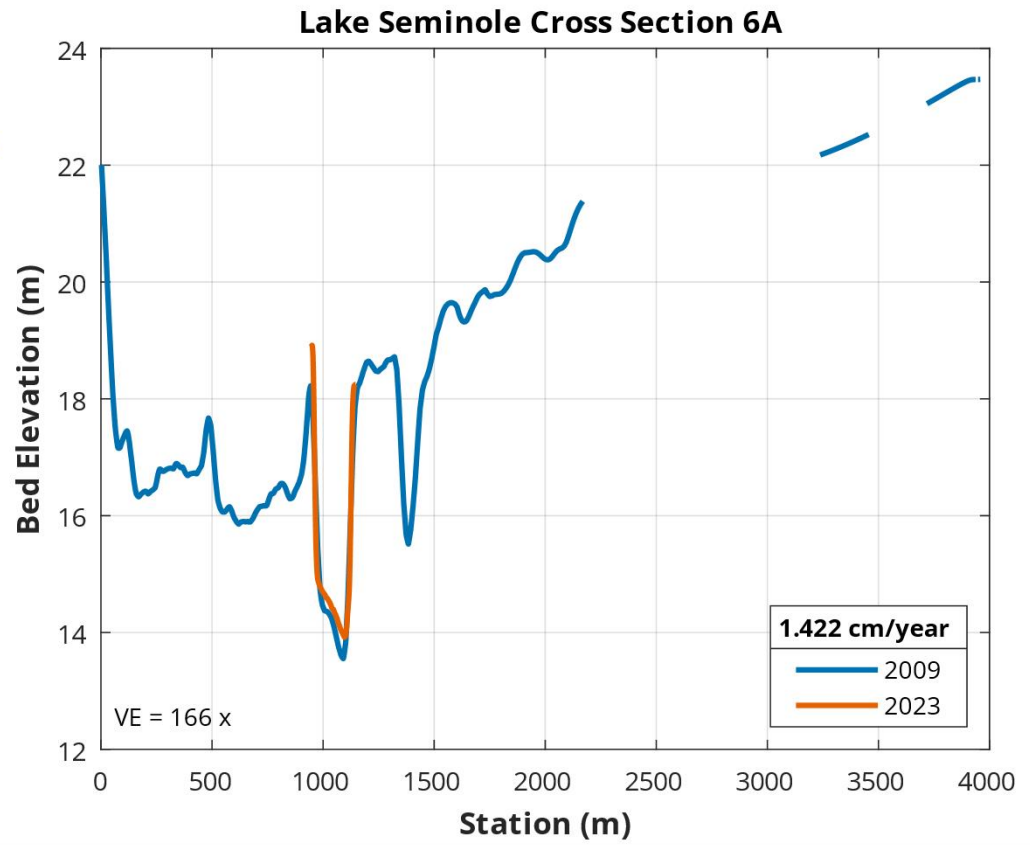
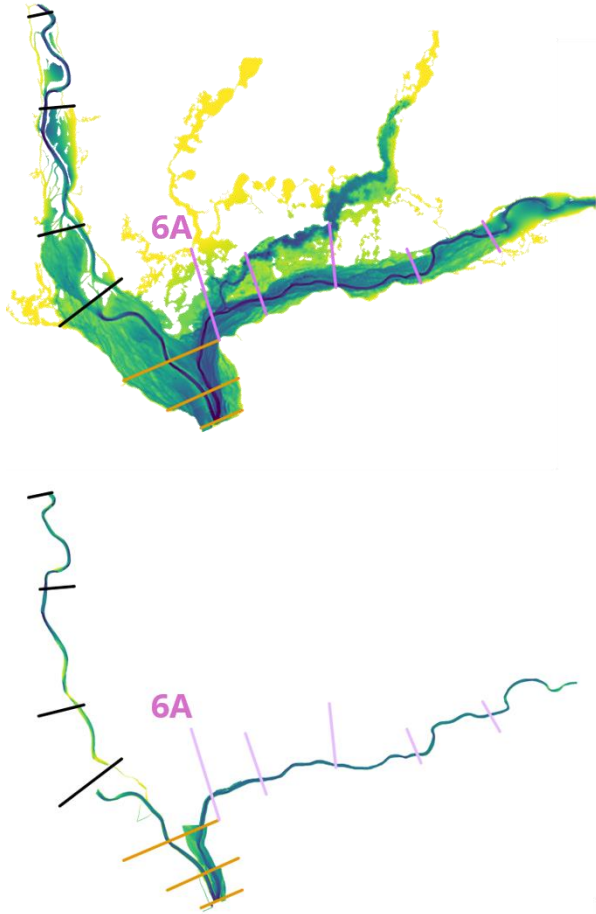


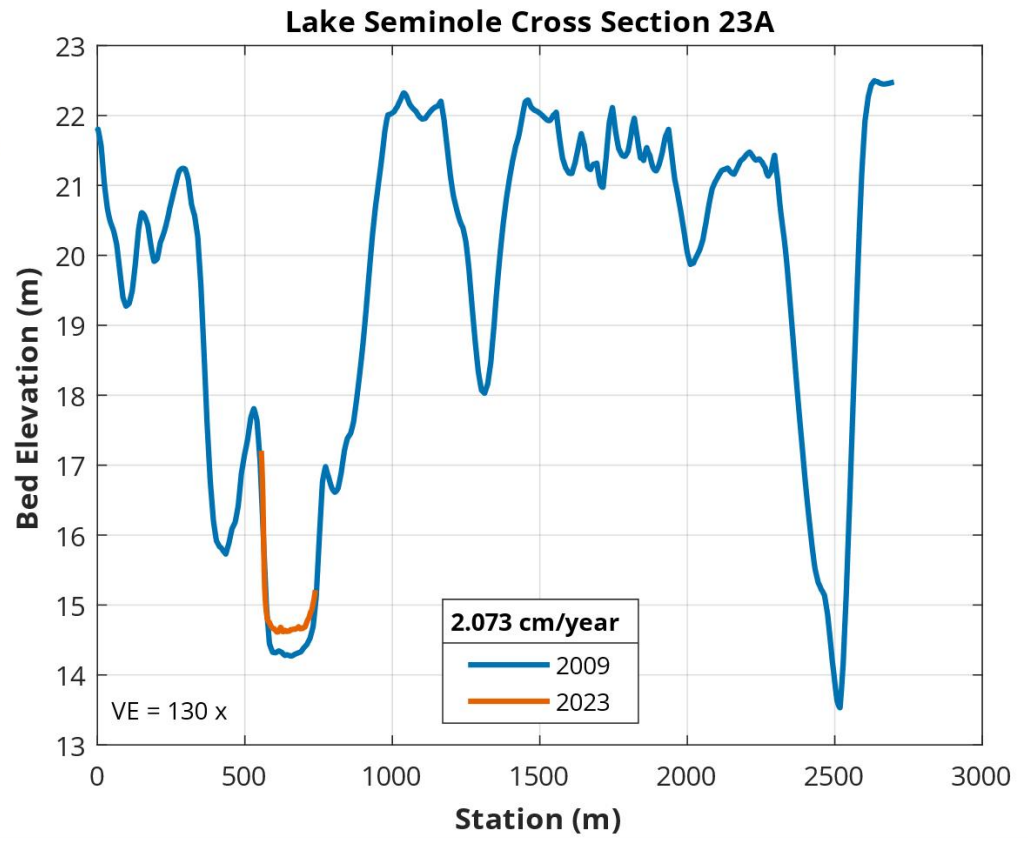
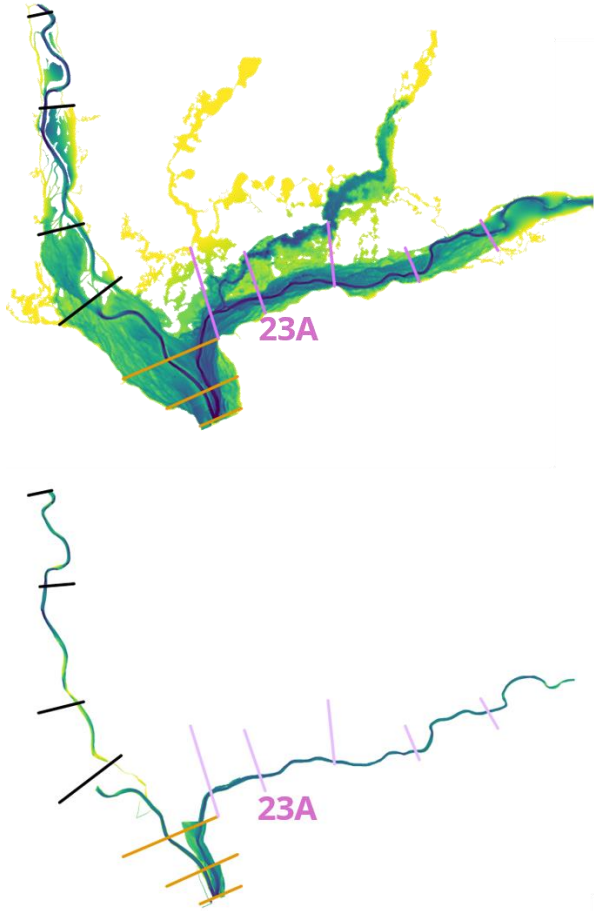


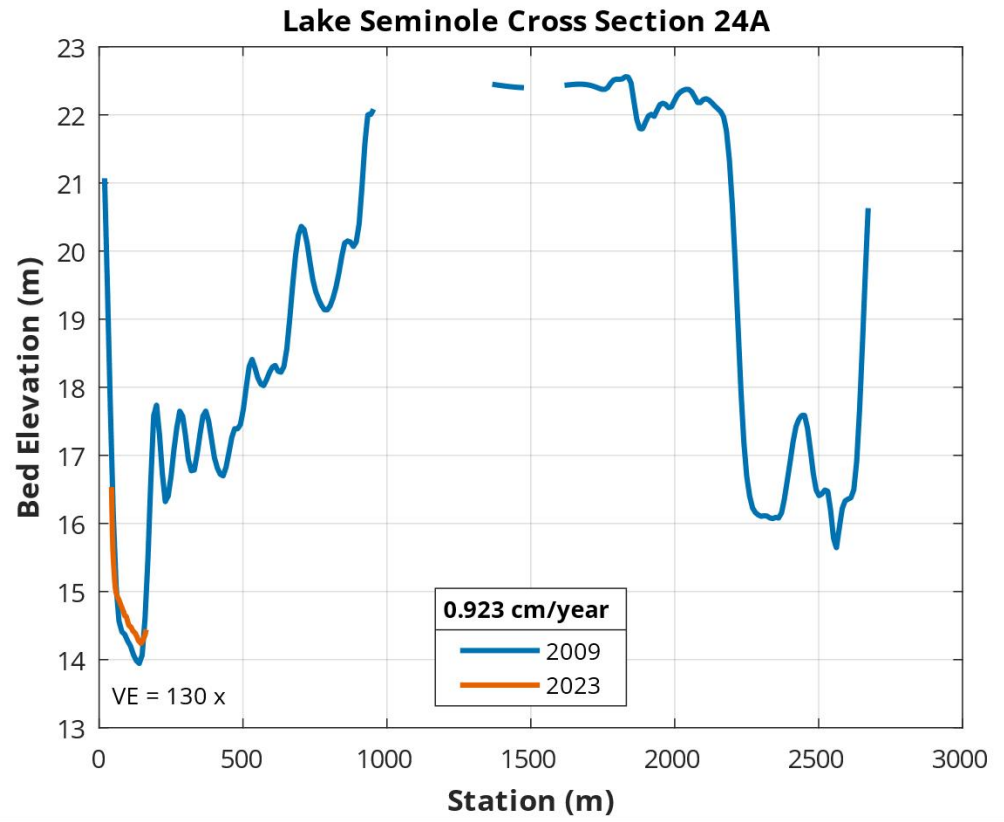
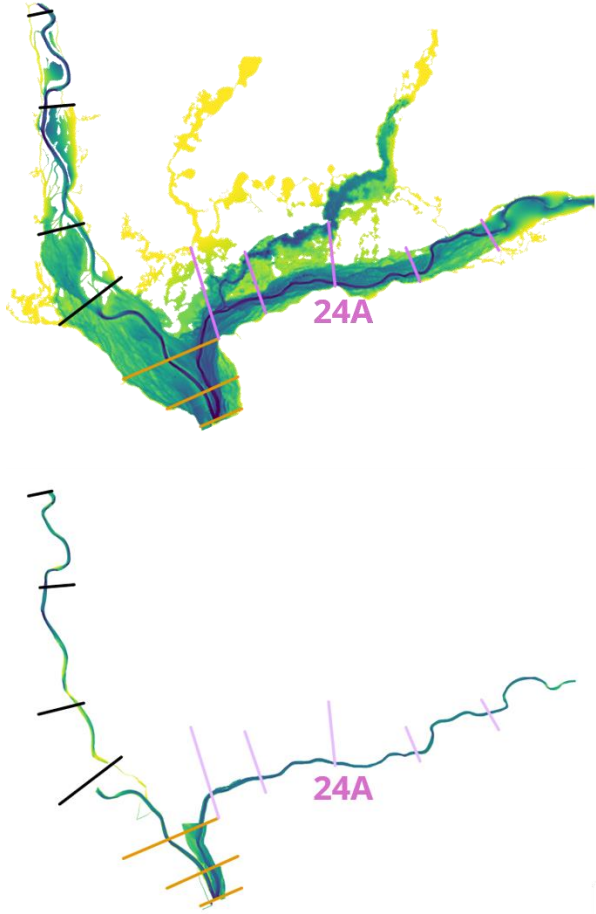


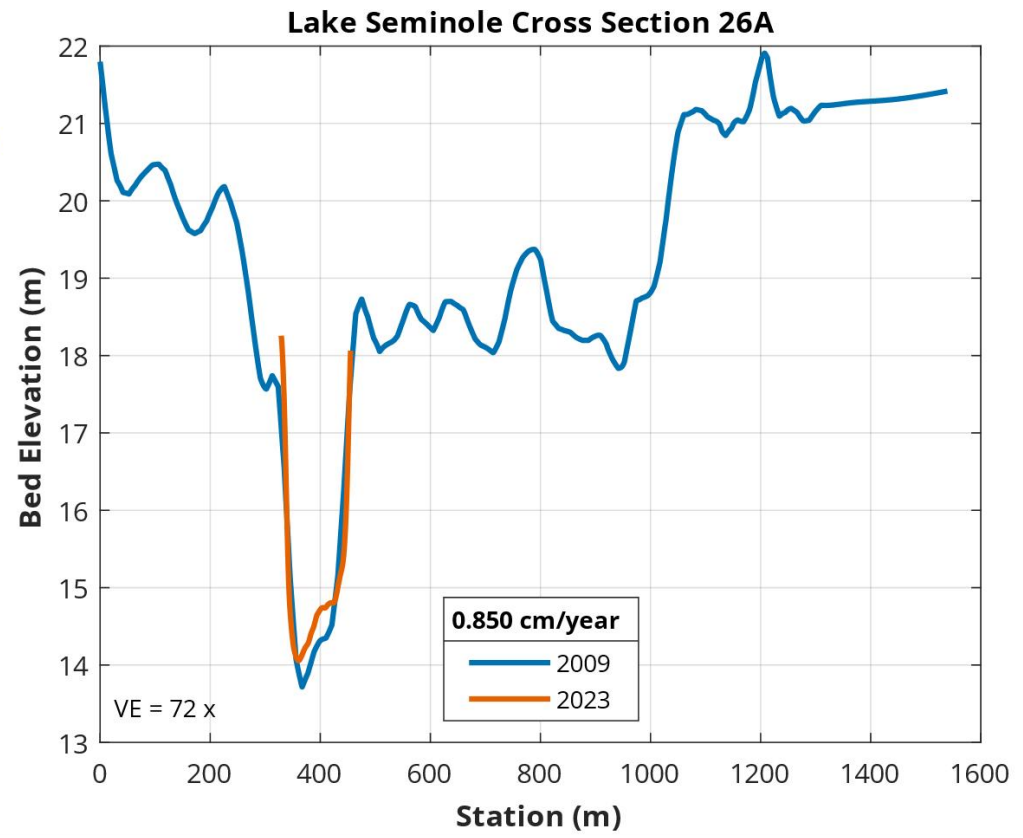
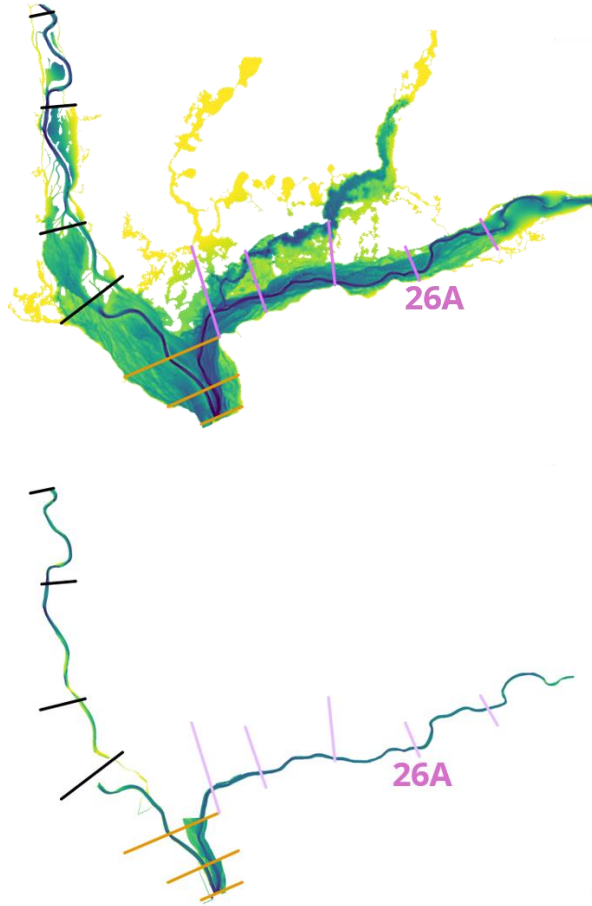
Lake Seminole Cross Section 9A

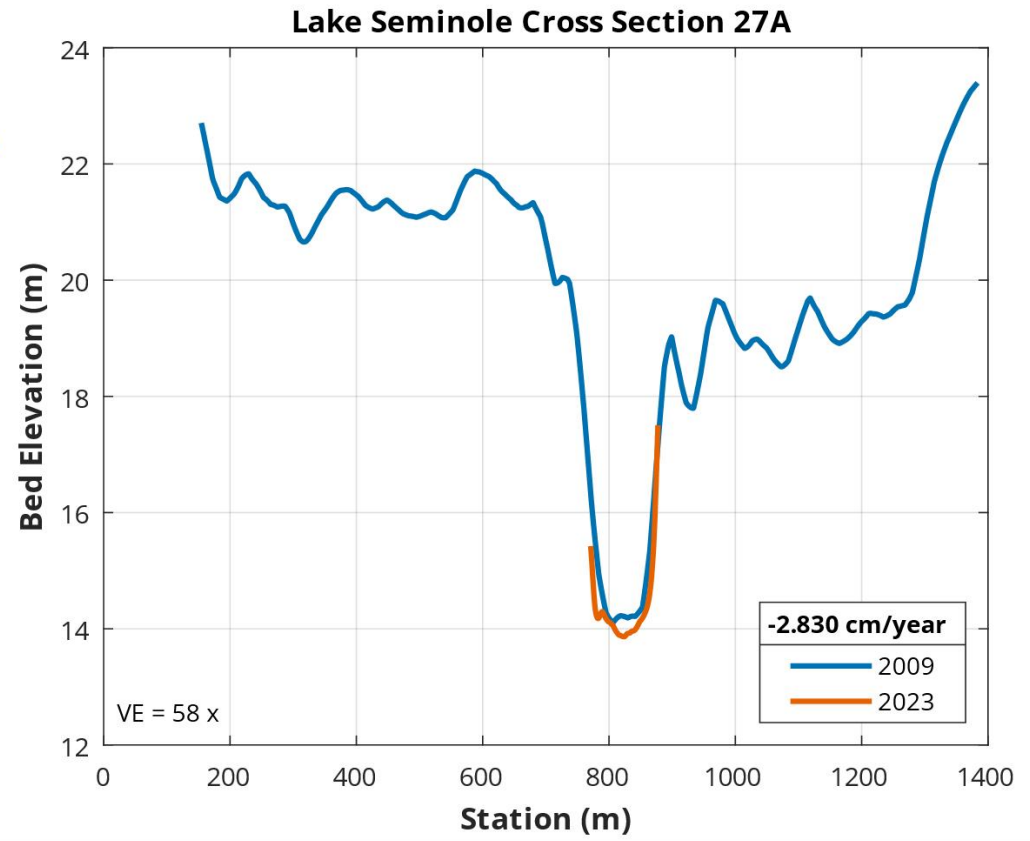
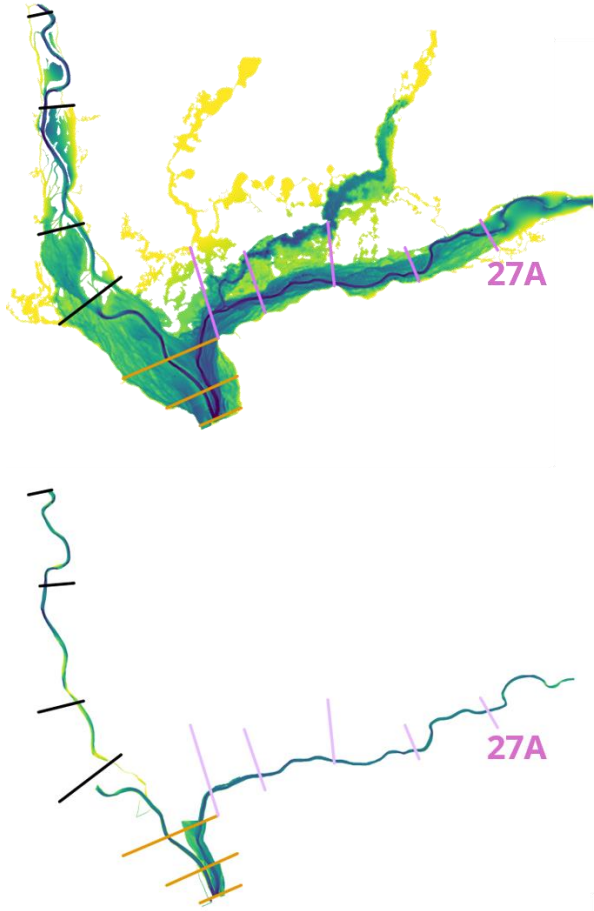




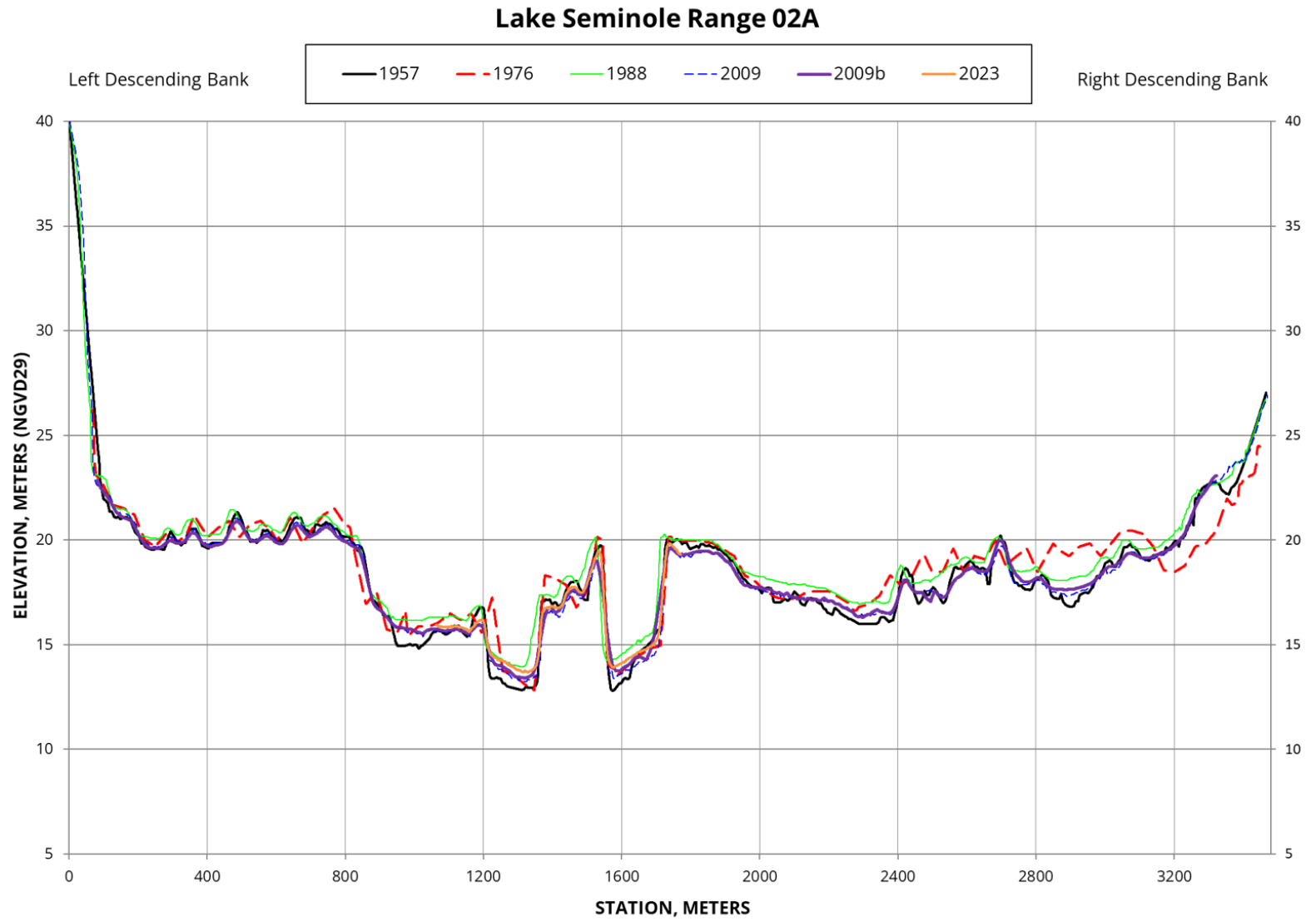








Appendix B: Combined USACE and Bathymetric Survey Cross Section Plots



Lake Seminole Range 03A

